

Coupled metal hydride reactions for preheating vehicle components at low temperatures

A thesis accepted by the Faculty of Energy-, Process- and Bio-Engineering
of the University of Stuttgart to fulfill the requirements
for the degree of Doctor of Engineering Sciences (Dr.-Ing.)

by

Mila Kölbig née Dieterich

born in Ulm

Main referee:	Prof. Dr. André Thess
Co-referee:	Prof. Dr. Thomas Klassen
Date of oral exam:	17.09.2018

Institute for Building Energetics, Thermotechnology and Energy Storage
of the University of Stuttgart

2018

Eigenständigkeitserklärung

Hiermit versichere ich, dass ich die vorgelegte Dissertation selbstständig und nur mit den angegebenen Hilfsmitteln verfasst habe. Alle Passagen, die ich wörtlich oder sinngemäß aus der Literatur oder anderen Quellen wie z. B. Internetseiten übernommen habe, habe ich deutlich als Zitat mit Angabe der Quelle kenntlich gemacht.

Parts of this study have been presented in scientific journals and at international conferences specified at the end of the reference section.

In this work, in order to provide easier reading, the common term “waste heat” or “heat” is sometimes used for (surplus) thermal energy, although it is thermodynamically not strictly correct to speak of heat if the transfer of the thermal energy is not actually mentioned or obvious.

Zusammenfassung

Verbrennungsmotoren produzieren heute die meisten Emissionen während der Kaltstartphase, bis das System auf Betriebstemperatur ist. Ein Vorheizers auf Basis gekoppelter Metallhydrid-Reaktionen könnte durch die potentiell schnelle Wärmebereitstellung zur Lösung dieses Problems beitragen. Jedoch stellen sowohl die niedrige Temperatur als auch die gegenseitig abhängigen Reaktionen starke Einschränkungen der Reaktionsrate dar. Bis heute ist wenig über Metallhydrid-Eigenschaften bei Temperaturen unter dem Gefrierpunkt bekannt und es fehlen systematische Untersuchungen gekoppelter Metallhydride. Dies verhinderte bisher die Entwicklung eines solchen Vorheizers. Diese Dissertation liefert detaillierte Untersuchungen gekoppelter Metallhydrid-Reaktionen bei niedrigen Temperaturen, um das Potential der thermischen Leistung und ihre Haupteinflussfaktoren zu identifizieren.

Darum wurden in dieser Arbeit das Materialpaar $\text{LaNi}_{4.85}\text{Al}_{0.15}$ und Hydralloy C5 ($\text{Ti}_{0.95}\text{Zr}_{0.05}\text{Mn}_{1.46}\text{V}_{0.45}\text{Fe}_{0.09}$), regenerierbar mit Abwärme zwischen 90 und 130 °C, charakterisiert, Einflussfaktoren auf die spezifische thermische Leistung im Labormaßstab systematisch untersucht und Haupteinflussfaktoren abgeleitet.

Die durchgeführte thermodynamische und kinetische Charakterisierung bis zu -30 °C liefert die ersten Daten für diese Materialien bei diesen niedrigen Temperaturen. Es wurde gezeigt, dass der Abstand zum Gleichgewicht als thermodynamisch treibende Kraft einen viel größeren Einfluss auf die spezifische thermische Leistung hat als die Starttemperatur der Einzelreaktion. Bei -20 °C und 10 bar lieferte $\text{LaNi}_{4.85}\text{Al}_{0.15}$ eine Leistung von über 5 kW/kg.

Die gekoppelten Reaktionen erreichten eine spezifische thermische Leistung von 600 W/kg bei -20 °C. Dies stellt den ersten veröffentlichten Wert für die Wärmeerzeugung bei dieser Temperatur dar. Er ist besonders hoch verglichen mit Literaturwerten, die sich bei +20 °C, also 40 K höher, im gleichen Bereich bewegen. Noch höhere spezifische Leistungen wurden bei höheren Temperaturen erzielt, wie zum Beispiel 1.1 kW/kg bei 0 °C und 1.6 kW/kg bei 20 °C. Somit ist die Umgebungstemperatur der Haupteinflussfaktor auf die gekoppelten Reaktionen. Es wurde gezeigt, dass das wasserstoffbereitstellende Material C5 die Limitierung der Leistung bei sinkenden Temperaturen durch seine sinkende Reaktionsrate während der Desorption verursacht.

Aus dieser ersten systematischen Untersuchung kann abgeleitet werden, dass die spezifische Leistung von Materialeigenschaften abhängt und nicht durch optimierten Wärmeübergang verbessert werden kann. Darum wird ein System vorgeschlagen, dass durch die potentielle Energie des fahrzeugeigenen Wasserstoffs eines Brennstoffzellen-Fahrzeugs betrieben wird – ohne den Wasserstoff zu verbrauchen – um so hohe Leistungen zu erreichen und den Weg für eine nachhaltige, kohlenstofffreie Mobilität zu ebnet.

Abstract

Today, internal combustion engines produce most emissions during the cold start phase until the system is at operation temperature. A preheater based on coupled metal hydride reactions could help solve this problem due to the potential to supply heat fast even at low temperatures. However, both the low temperature and the interdependent reactions might pose severe limitations on the reaction rate. Until now, little knowledge about metal hydride properties at subzero conditions and the lack of systematic investigation of the coupled metal hydrides have prevented the development of such a preheater. This thesis provides detailed investigations of coupled metal hydride reactions at low temperatures to identify the potential of thermal power and its main influence factors.

Therefore, in this work, the material pair $\text{LaNi}_{4.85}\text{Al}_{0.15}$ and Hydralloy C5 ($\text{Ti}_{0.95}\text{Zr}_{0.05}\text{Mn}_{1.46}\text{V}_{0.45}\text{Fe}_{0.09}$), rechargeable with onboard waste heat of 90 to 130 °C, was characterized, influencing factors on the specific thermal power were investigated systematically in laboratory scale and main factors of influence were derived.

The performed thermodynamic and kinetic characterization down to -30 °C provides the first data for these materials at such low temperatures. The distance to equilibrium as thermodynamic driving force is found to influence the specific thermal power much more than the actual starting temperature of the single reaction. At -20 °C and 10 bar, $\text{LaNi}_{4.85}\text{Al}_{0.15}$ provided a thermal power of more than 5 kW/kg.

For the coupled reactions at -20 °C, a specific thermal power of 600 W/kg was achieved, representing the first published value for heat generation at this temperature. It is exceptionally high, considering literature values are in the same range at +20 °C or 40 K higher. Even higher specific power levels were obtained at higher temperatures, such as 1.1 kW/kg at 0 °C and 1.6 kW/kg at 20 °C. Therefore, the main influencing factor on the coupled reactions is the ambient temperature. The hydrogen-providing material C5 is identified as cause for this limitation due to its decreasing reaction rate during desorption.

From this first systematic investigation, it is concluded that the specific power output depends on material properties and cannot be improved by optimizing heat transfer. Consequently, a system using the potential energy of onboard hydrogen in a fuel cell vehicle – without consuming it – is proposed in order to reach a high thermal power and help pave the way to a sustainable, carbon-free mobility.

Table of content

Zusammenfassung.....	v
Abstract	vii
Table of content	ix
List of Figures.....	xi
List of Tables.....	xiii
Nomenclature, abbreviations and indices	xv
1. Introduction	1
1.1. Motivation	1
1.2. Fundamentals of metal hydrides.....	3
1.2.1. Thermodynamics.....	5
1.2.2. Reaction kinetics	7
1.3. Literature review	9
1.3.1. Material properties at low temperatures	9
1.3.2. Thermal applications of metal hydrides.....	17
1.4. Challenge of coupled reactions	24
1.5. Aim of thesis	25
2. Material characterization.....	27
2.1. Material selection.....	27
2.2. Methodology and test bench for material characterization	30
2.2.1. Methodology.....	30
2.2.2. Test bench	31
2.3. Thermodynamics (Pressure-Concentration Isotherm).....	34
2.3.1. Measurement procedure	34
2.3.2. Reactor design.....	35
2.3.3. Analysis.....	36
2.3.4. Experimental design	37
2.3.5. Results	39
2.4. Reaction kinetics.....	48
2.4.1. Measurement procedure	49

2.4.2.	Reactor design	50
2.4.3.	Analysis.....	51
2.4.4.	Experimental design	52
2.4.5.	Results	53
3.	Experiments in laboratory scale	58
3.1.	Methodology	58
3.1.1.	Reactor design.....	59
3.1.2.	Test bench and analysis.....	61
3.1.3.	Experimental design	66
3.1.4.	Repeatability	67
3.2.	Single reaction	69
3.2.1.	Absorption of $\text{LaNi}_{4.85}\text{Al}_{0.15}$	70
3.2.2.	Desorption of $\text{Ti}_{0.95}\text{Zr}_{0.05}\text{Mn}_{1.46}\text{V}_{0.45}\text{Fe}_{0.09}$ (C5).....	74
3.3.	Coupled reactions.....	79
3.3.1.	Variation of mass flow of heat transfer fluid	80
3.3.2.	Variation of regeneration temperature	82
3.3.3.	Variation of ambient temperature.....	84
3.3.4.	Conclusions from coupled reactions	85
3.4.	Characteristics of $\text{Ti}_{0.95}\text{Zr}_{0.05}\text{Mn}_{1.46}\text{V}_{0.45}\text{Fe}_{0.09}$ (C5)	86
3.5.	Summary of all laboratory scale experiments.....	88
4.	Discussion and conclusion	91
4.1.	Factors influencing the specific thermal power	91
4.2.	Conclusion	95
5.	Summary and outlook.....	98
	References.....	101
	Appendix.....	111

List of Figures

Figure 1. Reversible metal hydride reaction	3
Figure 2. Scheme of pressure-concentration isotherm (PCI) and van't Hoff-plot of a metal hydride.....	6
Figure 3. Available thermodynamic data for $\text{LaNi}_{4.85}\text{Al}_{0.15}$ and C5 [54]–[58], [60], [61]	11
Figure 4. Available kinetic data for $\text{LaNi}_{4.85}\text{Al}_{0.15}$, C5 and LaNi_5 [21], [56], [60]	15
Figure 5. Overview of usable (black) and missing (orange) data on properties for $\text{LaNi}_{4.85}\text{Al}_{0.15}$ and C5.....	16
Figure 6. Schema of discharge and regeneration of a closed metal hydride system	18
Figure 7. Dependencies of the interlinked coupled reactions	25
Figure 8. Extrapolated equilibrium data for $\text{LaNi}_{4.85}\text{Al}_{0.15}$ [54] and C5 [61]	29
Figure 9. Schematic of thermodynamic and reaction rate measurements	31
Figure 10. Layout of characterization test bench	31
Figure 11. Picture of the characterization test bench.....	33
Figure 12. Exemplary measurement results for absorption and desorption (exp. #6)	35
Figure 13. Reactor for dynamic pressure-concentration isotherm measurements	36
Figure 14. PCI for $\text{LaNi}_{4.85}\text{Al}_{0.15}$ at (a) -20°C , (b) 20°C and (c) 40°C at different hydrogen flow rates and repeated experiments	40
Figure 15. Comparison of results of $\text{LaNi}_{4.85}\text{Al}_{0.15}$ to literature [54]–[56]	42
Figure 16. PCI measurements for $\text{LaNi}_{4.85}\text{Al}_{0.15}$ for all temperatures (-20°C : #6, 0°C : #7, 20°C : #1, 40°C : #4, 110°C : #9, 130°C : #10).....	42
Figure 17. Van't Hoff plot from PCI measurements for $\text{LaNi}_{4.85}\text{Al}_{0.15}$ for absorption (solid) and desorption (dashed)	43
Figure 18. PCI for C5 at -30°C at different hydrogen volume flow rates and repeated experiments (exp. #1, 2).....	45
Figure 19. Comparison of results of C5 to literature [58], [60], [61]	45
Figure 20. PCI measurements for C5 for all temperatures (-30°C : #1, -20°C : #3, 20°C : #5, 35°C : #4)	46
Figure 21. Van't Hoff plot from PCI measurements for C5 for absorption and desorption	47
Figure 22. Van't Hoff plot for both $\text{LaNi}_{4.85}\text{Al}_{0.15}$ (red) and C5 (blue); absorption (solid), desorption (dashed)	48
Figure 23. Pressure signal over time (exp. #II-7).....	50
Figure 24. Reactor for reaction rate measurements.....	51
Figure 25. Temperature change in reactor for all experiments of the reaction rate measurements for charge I (left) and II (right).....	53
Figure 26. Repeatability of experiments (exp. #II-1 and II-5); pressure drop and transformed fraction (left) and obtained coefficient of mechanism and pressure function (right)..	54
Figure 27. Coefficient of mechanism and pressure function, including fit function and transformed fraction (exp. #II-7).....	54
Figure 28. Rate coefficients for $\text{LaNi}_{4.85}\text{Al}_{0.15}$ for all performed experiments and for C5 [60]	55
Figure 29. Rate coefficient for $\text{LaNi}_{4.85}\text{Al}_{0.15}$ compared to LaNi_5 [21], [56], [60]	56

Figure 30. Modular reactor design for laboratory scale	59
Figure 31. Laboratory scale reactor in detail	60
Figure 32. Specifications of laboratory scale reactor	61
Figure 33. Test bench design with photo (left) and scheme (right).....	61
Figure 34. (a) Measurement data of reactor 1 and (b) calculated thermal power of reactor 1 and 2 (exp. #1)	65
Figure 35. Repeatability of laboratory experiments	69
Figure 36. Single reaction of $\text{LaNi}_{4.85}\text{Al}_{0.15}$ – Variation of HTF mass flow, including measurement uncertainties of hydrogen conversion (exp. #I, II).....	70
Figure 37. Single reaction of $\text{LaNi}_{4.85}\text{Al}_{0.15}$ – Variation of ambient temperature, including measurement uncertainties of hydrogen conversion (exp. #I, IV, V, VI, VII)	72
Figure 38. Single reaction of $\text{LaNi}_{4.85}\text{Al}_{0.15}$ - Variation of supply pressure (exp. #I, IV, X at $-20\text{ }^{\circ}\text{C}$ and #V, VI at $0\text{ }^{\circ}\text{C}$)	73
Figure 39. Single reaction of C5 – Response close to equilibrium (exp. #XVI, XVII)	76
Figure 40. Single reaction of C5 – Pressure and temperature at varied ambient temperatures (exp. #XII, XV).....	77
Figure 41. Single reaction of C5 – Specific thermal power and hydrogen conversion at varied ambient temperatures (exp. #XII, XV)	78
Figure 42. Coupled reactions - Variation of mass flow of heat transfer fluid, including measurement uncertainties of hydrogen conversion (exp. #12, 10 at $-20\text{ }^{\circ}\text{C}$ and #5, 1, 9 at $20\text{ }^{\circ}\text{C}$).....	81
Figure 43. Coupled reactions – Temperature of C5 and hydrogen conversion for HTF mass flow variation at $20\text{ }^{\circ}\text{C}$ (exp. #5, 1, 9)	82
Figure 44. Coupled reactions - Variation of regeneration temperature, including measurement uncertainties of hydrogen conversion (exp. #7, 10 at $-20\text{ }^{\circ}\text{C}$ and #3, 4, 6 at $0\text{ }^{\circ}\text{C}$).....	83
Figure 45. Coupled reactions - Variation of ambient temperature, including measurement uncertainties of hydrogen conversion (exp. #10, 6, 1)	85
Figure 46. Temperature course of C5 at experiments with high reaction rates (single reaction at $20\text{ }^{\circ}\text{C}$, exp. #XIV; coupled reactions at $20\text{ }^{\circ}\text{C}$ and HTF mass flow of 425 kg/h , exp. #9).....	87
Figure 47. Kinetic fits of laboratory scale experiments.....	93
Figure 48. Apparent rate coefficients of the coupled reactions at 0 and $-20\text{ }^{\circ}\text{C}$ and the rate coefficients for $\text{LaNi}_{4.85}\text{Al}_{0.15}$ (this work) and C5 [60]	94

List of Tables

Table 1. Investigated compositions of Hydralloy C5	11
Table 2. Overview of metal hydride thermal power applications in literature, focusing on low temperatures.....	21
Table 3. Measurement equipment of the characterization test bench.....	33
Table 4. Experimental design for PCI measurements of $\text{LaNi}_{4.85}\text{Al}_{0.15}$	38
Table 5. Experimental design for PCI measurements of C5	38
Table 6. Reaction enthalpy, entropy and plateau slope for $\text{LaNi}_{4.85}\text{Al}_{0.15}$	43
Table 7. Reaction enthalpy, entropy and plateau slope for C5.....	47
Table 8. Experimental design of reaction rate measurements of $\text{LaNi}_{4.85}\text{Al}_{0.15}$	52
Table 9. Results of all reaction rate experiments.....	56
Table 10. Measurement equipment of laboratory scale test bench	62
Table 11. Experimental design of the coupled reactions in laboratory scale	66
Table 12. Experimental design of the single reactions in laboratory scale	67
Table 13. Specific thermal power, thermal energy and hydrogen conversion for all experiments in laboratory scale	89
Table 14. Composition information of Hydralloy C5 from supplier	112
Table 15. Tubes, Sieverts' and reactors free volumes, partly from [112].....	113
Table 16. Overall hydrogen conversion for the large scale experiments at -20 and 20 °C....	121
Table 17. Plateau slopes for all temperature for $\text{LaNi}_{4.85}\text{Al}_{0.15}$	122
Table 18. Plateau slopes for all temperature for C5	122

Nomenclature, abbreviations and indices

Symbol	Description	Units
Latin letters		
A	Pre-exponential factor	1/s
c_p	Heat capacity	J/(gK)
$\Delta_R H$	Reaction enthalpy	kJ/(mol K)
$\Delta_R S$	Reaction entropy	J/(mol K)
E_a	Activation energy	kJ/mol
f	Factor between end and equilibrium pressure	-
F	Antiderivative	
H ₂	Hydrogen	
k	Rate coefficient	1/s
m	Mass	g
M	Molar mass of hydrogen (2)	g/mol _{H2}
\dot{m}	Mass flow	kg/h
m_{pl}	Plateau slope of PCI	wt.-% ⁻¹
p	Pressure	bar
P	Specific thermal power	kW/kg
p_0	Standard pressure (1)	bar
p_N	Normal pressure (1.013)	bar
Q	Thermal energy	kJ
q	Specific thermal energy	kJ/kg _{MH}
R	Universal gas constant (8.314)	J/(mol K)
r	Ratio of reactor to metal hydride mass	-
T	Temperature	°C
t	Time	s
T_N	Normal temperature (273.15)	K
\dot{V}	Hydrogen volume flow	ml _N /min
x	Transformed fraction	%

Greek letters

Δ	Difference	
α	Solid solution phase	
α_{reactor}	Heat transfer coefficient of reactor	W/(m ² K)
β	Metal hydride phase	
ω	Hydrogen conversion	wt.-%

Indices

1	Referring to MH1 (LaNi _{4.85} Al _{0.15})
2	Referring to MH2 (C5)
600s	Value after 600 s
amb	Ambient
corr	Corrected value
d	Differential
end	At the end of measurement
eq	Equilibrium
free	Free volume
H ₂	Hydrogen
in	At the inlet
init	Initial
max	Maximal value
mean	Mean value
MH	Metal hydride
mid	Middle
out	At the outlet
R	Reactor
reg	Regeneration
S/Siev	Sieverts'
th	Thermal
tl	Tube left (characterization test bench)
tr	Tube right (characterization test bench)

Abbreviations

A	Stable hydride forming metals
abs	Absorption
B	Non-hydride forming metals
C5	Hydrogen-supplying material in this work ($\text{Ti}_{0.95}\text{Zr}_{0.05}\text{Mn}_{1.46}\text{V}_{0.45}\text{Fe}_{0.09}$)
CH_4	Methane
des	Desorption
FS	Full scale
HC	Hydrocarbons
HTF	Heat transfer fluid
HV	Hand valve
ICE	Internal combustion engine
$\text{LaNi}_{4.85}\text{Al}_{0.15}$	Heat-generating metal hydride in this work
MFM	Mass flow meter for HTF
MH	Metal hydride
MH1	Heat-generating material $\text{LaNi}_{4.85}\text{Al}_{0.15}$
MH2	Hydrogen-supplying material C5
NO_x	Nitrogen oxides
NPDM	Normalized pressure dependence method
PCI	Pressure-concentration isotherm
PEMFC	Proton exchange membrane fuel cell
Rd	Reading
TD	Thermodynamics
V	Pneumatic valve
VFC	Volume flow controller for hydrogen
VFM	Volume flow meter for hydrogen
VOC	Volatile organic compounds
VP	Vacuum pump

1. Introduction

1.1. Motivation

What will mobility look like tomorrow?

Of course, this question cannot be answered precisely. Today, however, almost 40 % of all nitrogen oxides emissions come from the mobility sector [1]. Following the trend of increasing mobility [2] and including autonomous driving, the travelled kilometers will increase substantially in the future. If we cannot find a sustainable solution, local pollution and global climate change will pick up the pace and pose huge challenges to human kind.

In the long run, electric drives powered by either batteries or fuel cells have the potential to solve this problem, if the electricity or hydrogen can be provided free of emissions. However, the transition phase already provides huge potentials for quick emission reduction.

Power engines working at elevated temperature generate propulsion inefficiently during the cold start phase as long as below operation temperature. This is true for all types of engines such as internal combustion engines or fuel cells.

For internal combustion engines in particular, the operation below the designated temperature of around 100 °C has severe impacts on the environment. During the cold start phase neither the combustion process nor the exhaust gas treatment work sufficiently. Due to wall quenching in the cylinder and low combustion temperatures, the amount of pollutants is increased. Therefore, in these first couple of minutes, 60 - 80 % of all pollutants of the whole ride are produced. This includes mainly nitrogen oxides (NO_x), hydrocarbons (CH₄ and other HC) and volatile organic compounds (VOC). As ICEs nowadays become more and more efficient, waste heat is reduced and this leads to a prolonged cold start phase and even more pollutants. Additionally, the low temperature has also negative effect on the lubricant and the engine itself. The high viscosity of the engine oil at low temperatures [3] leads to its degradation and the reduced lubrication effect increases engine wear. If the components would be preheated quickly, a large amount of the pollutants could be prevented and operation life could be prolonged. [4]–[11]

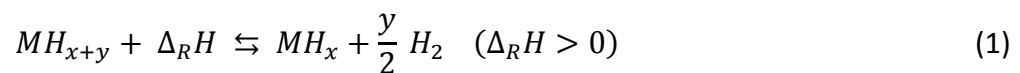
Once the system is at operation temperature, after approx. 5 - 10 min, very little pollutants are released. From this point on, waste heat is generated, which has to be dissipated to prevent overheating. At nominal operation, the combustion engine releases around 2/3 of the energy as heat [12]. Waste heat occurs in the exhaust gas, due to radiation, in the cooling circuit or the engine lubricant. The latter two are best accessible for heat recovery.

This time shift in demand and occurrence of thermal energy can be overcome with a thermal energy system driven by waste heat. This way, the start-up phase can be shortened and its negative impacts can be reduced drastically without consuming additional energy. Furthermore, the harvested energy could also be used for other heat demands in the vehicle.

Such a preheater based on a thermochemical reaction of metal hydrides is investigated in this thesis. The main focus is the high thermal power required within the short cold start period.

Ambient temperatures for cold start between -20 and 20 °C were considered in this work. These values are around 15 K below the lowest and above the highest mean winter temperature in Germany¹, ensuring functionality of the system for Central Europe in almost all cases. For regeneration, waste heat of the ICE between 90 and 130 °C is considered, as it might occur e.g. in the engine lubricant. This represents very low regeneration temperatures compared to literature (see subsection 1.3.2).

Metal hydrides are metal alloys reacting exo-/endothermally with hydrogen according to equation (1) [13]. They receive increasing attention for thermal applications due to their very fast reaction, even at low temperatures.



Besides the intrinsic advantages of the gas/solid reaction, such as discharge on demand by recombining the separated reaction partners and recharge by waste heat without the requirement of thermal insulation, metal hydrides provide high thermal energy density and fast reaction rates. These advantages could lead to an easy (pre-) heating system without

¹ The lowest mean winter temperature in Germany between 1882 and 2017 was -5.5°C, the highest was 4.4 °C, according to the Deutscher Wetterdienst (German weather service) [113].

additional energy consumption other than a small increase of the vehicle mass and, hence, reduce emissions drastically.

However, all thermochemical reactions slow down with decreasing temperature. This might pose limitations on the achievable specific thermal power, in particular if hydrogen has to be provided within the thermal storage system. This can be realized by using two metal hydrides with different thermodynamics, which exchange hydrogen in a coupled reaction. This represents a considerably complex process, which is described in section 1.4.

Details on the working principle of metal hydrides and an extensive literature review of material properties as well as their thermal applications are given in the following. Subsequently, the challenge of coupled reactions is discussed and the aim of thesis is derived thereof.

1.2. Fundamentals of metal hydrides

Metal hydrides are metal alloys that form hydrides by absorbing hydrogen. Only metallic hydrides are considered here, which mostly keep the properties of metals but are usually more brittle [14]. In this section, their thermodynamic and kinetic properties are described in detail.

The reversible gas-solid reaction is depicted in Figure 1. The solid metal hydride can absorb gaseous hydrogen in its lattice, which releases thermal energy in an exothermic reaction (left to right). By providing thermal energy, the endothermic back reaction is triggered and hydrogen is desorbed (right to left). The ab- and desorption is an equilibrium process, depending on hydrogen pressure and solid temperature. Hence, desorption can also be initiated by lowering the gas pressure below equilibrium pressure at a constant temperature.

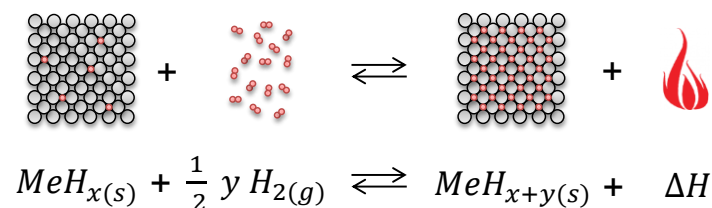


Figure 1. Reversible metal hydride reaction

These thermochemical reactions have several advantages. They can provide high energy densities due to high reaction enthalpies and can be recharged by onboard waste heat without the need of additional energy. The reaction partners can be separated easily due to their different physical state. Thus, the energy can be stored as chemical potential at room temperature without the necessity of insulation and the generation of heat can be triggered on demand by recombining both components.

The statements above are true for all types of thermochemical reactions. However, at present, only metal hydrides seem to have the potential to react at room temperature with an adequate reaction rate to satisfy the high thermal power demand of vehicle applications.

Most hydrides formed by one element don't show reversible properties at moderate temperatures and pressures. Only a few, such as Mg, show promising characteristics for hydrogen storage applications at elevated temperature [15], [16]. However, the combination of these stable hydride forming metals (so called A-metals or hydride formers) and non-hydride forming metals (so called B-metals or hydride modifiers) yields alloys with phase formation at technically relevant temperature and pressure levels, as first suggested by van Vucht et. al [17]. According to their stoichiometry, these intermetallic compounds can be grouped as: A_2B (e.g. Mg_2Ni), AB (e.g. $ZrNi$), AB_2 (e.g. $TiMn_2$), AB_3 (e.g. $LaCo_3$) and AB_5 (e.g. $LaNi_5$). [13], [18], [19]

The equilibrium pressure for a given temperature can be varied by substitution of elements, e.g. investigated for $LaNi_5$ [20]–[22] or $ZrNi$ [23]. Therefore, a wide variety of metal hydride alloys are known, from which appropriate materials can be selected for the according application. In this work, the alloy $LaNi_{4.85}Al_{0.15}$ (AB_5 , based on $LaNi_5$) and $Ti_{0.95}Zr_{0.05}Mn_{1.46}V_{0.45}Fe_{0.09}$ (AB_2 , based on $TiMn_2$, so called Hydralloy C5) are used.

The expansion during absorption and the shrinkage during desorption exerts stress on the metal lattice and leads to crumbling of the alloy until equilibrium between lattice bonding and expansion stress is reached. Usually, this leads to particle sizes of an activated metal hydride powder in the low micrometer range (1-20 μm) [24], [25]. On the one hand, this leads to a large surface benefitting hydrogen penetration and reducing the share of passivated surface; on the other hand, the thermal conductivity of the powder is decreased drastically compared to pure metal.

1.2.1. Thermodynamics

Each metal hydride has its specific equilibrium correlation, which defines the temperature and pressure range at which the hydride is stable. This information on metal hydride thermodynamics is pivotal to identify an appropriate metal hydride for a certain application. For a given metal hydride, the temperature level of the thermal energy released or required depends on the hydrogen pressure. A higher pressure level corresponds to a higher temperature level. In order to determine the thermodynamic equilibrium, a pressure-concentration isotherm (PCI) has to be measured, as given in Figure 2, left. The concentration is usually given as the ratio of either the number of H-atoms to the number of metal atoms (H/M-ratio) or of the hydrogen mass to the metal mass (wt.-%). The mass based hydrogen conversion is used in this work and is defined by equation (2). Referred to the whole reversible hydrogen content, the transformed fraction in % is defined by equation (3).

$$\omega = \frac{m_{H2}}{m_{MH}} \cdot 100 \quad (2)$$

$$x = \frac{\omega}{\omega_{max}} \cdot 100 \quad (3)$$

As can be seen in the left part of Figure 2, the PCI curve for a given temperature forms three distinct parts. During the initial steep increase, hydrogen is physically absorbed forming the solid solution or α -phase. The reaction follows the Sieverts' law where the hydrogen conversion is proportional to the root of the hydrogen pressure ($\omega \sim \sqrt{p_{eq}}$). After reaching the saturation limit of solution, the formation of a distinct second solid phase, the hydride or β -phase, begins. Now, the α -phase converts into the β -phase. At this plateau or $\alpha+\beta$ region, the pressure remains almost constant while hydrogen conversion increases following the Gibb's Phase Rule. At the end of the plateau, everything converted into the β -phase, the actual metal hydride. If more hydrogen is dissolved in the β -phase, the pressure rises again steeply according to the Sieverts' law. [13], [26]

The plateau region is the most important part used in the applications of metal hydrides, because here, a large amount of hydrogen is absorbed. The corresponding pressure and temperature are generally referred to as the equilibrium values of the material. With increasing temperature, the equilibrium pressure increases and the plateau width decreases.

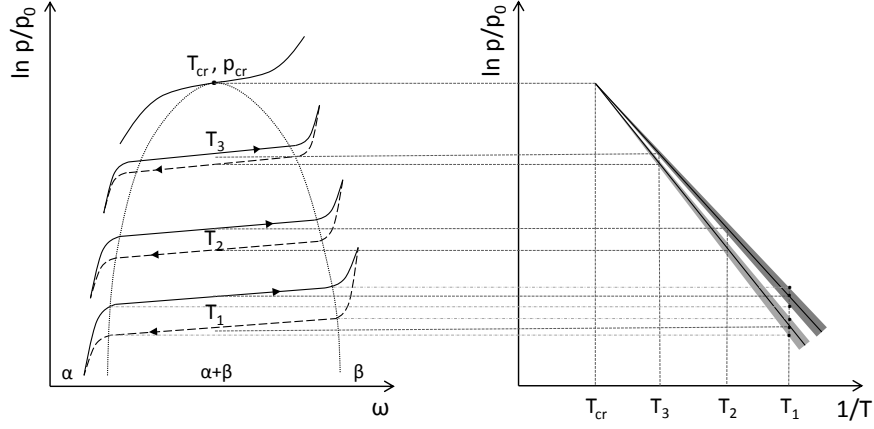


Figure 2. Scheme of pressure concentration-isotherm (PCI) and van't Hoff-plot of a metal hydride

Plateau slope

For most real materials, the plateau shows a slope leading to a certain pressure range in the $\alpha+\beta$ region. This indicates an overlap of different equilibrium pressures of different parts of the material due to inhomogeneities of the surface, impurities and stress [26]. Although the plateau slope might not be linear for the whole plateau region, usually it is sufficient to derive a constant slope value m_{pl} in $\text{wt.}\%^{-1}$ at the middle of the plateau (ω_{mid}) according to equation (4).

$$m_{pl} = \left. \frac{d \left(\ln \frac{p_{eq}}{p_0} \right)}{d\omega} \right|_{\omega_{mid}} \quad (4)$$

Hysteresis

Additionally, a hysteresis occurs between absorption and desorption, leading to a lower desorption plateau pressure, indicated by solid (absorption) and dashed (desorption) lines in Figure 2. In literature, this effect is correlated to lattice expansion during hydration requiring a larger hydrogen pressure for the absorption [26]. Although other theories exist, such as a decrease of the hysteresis with decreasing particle size as suggested by Rabkin and Skripnyuk [27], for the considered particle size in this work, as for most investigations published, hysteresis is observed.

Hence, the hysteresis, just like the plateau slope, has to be taken into account for further considerations.

Several PCI-measurements at different temperatures lead to the correlation between equilibrium pressure and temperature as given in equation (5), which is shown in a van't Hoff-plot in Figure 2, right. Thereby, the reaction enthalpy $\Delta_R H$ and entropy $\Delta_R S$ can be derived. [13], [18]

$$\ln\left(\frac{p_{eq}}{p_0}\right) = \frac{-\Delta_R H}{R T} + \frac{\Delta_R S}{R} \quad (5)$$

Although, both reaction enthalpy and entropy are not strictly independent of temperature, in most cases and in particular at small temperature ranges, a constant value is a fair assumption [28]. To account for the slope, the equilibrium pressure at different hydrogen conversion rates (e.g. 10, 50, and 90 % of total hydrogen conversion of the plateau) is considered for the pressure-temperature correlation. Due to hysteresis, the lower desorption pressure values lead to higher values for the reaction enthalpy and entropy.

1.2.2. Reaction kinetics

The overall reaction rate $\frac{\partial x}{\partial t}$ can be determined from experiments. It is affected by both, external factors, such as temperature and applied pressure, and internal ones, like particle size and hydrogen conversion. It is commonly described as given in equation (6) [29].

$$\frac{\partial x}{\partial t} = k(T) \cdot f(p) \cdot f(x) \quad (6)$$

Besides the temperature dependent rate coefficient $k(T)$, it additionally depends on the pressure dependence function $f(p)$ as well as the reaction mechanism $f(x)$. In order to determine the rate coefficient, the pressure dependence function and the mechanism have to be described.

The pressure dependence function describes the effect of the thermodynamic equilibrium. This pressure dependence, however, was interpreted differently in literature, leading to a large discrepancy between the results, as was pointed out by Ron in [24]. As a consequence, he also proposes a normalization method (normalized pressure dependence method, NPDM), allowing good comparison of different experimental set-ups if the instructions are followed (see p.15). Therefore, this work will follow this method with the pressure dependence function as given in equation (7). Due to the modulus, the equation applies for both absorption and desorption.

$$f(p) = \frac{|p_{eq} - p|}{p_{eq}} \quad (7)$$

For the description of the reaction mechanism, the hydrogenation of a metal hydride alloy has to be considered. The process consists of several consecutive steps. The rate controlling step has to be identified by comparing mathematical models of each step with experimental results. However, there is no consensus in literature on the precise hydration process.

E.g. in [30], Gérard and Ono mention a sequence of 5 steps: (1) gas transport, (2) surface adsorption and dissociation, (3) transition from surface to bulk, (4) diffusion and (5) nucleation and growth. Also, Martin et al. [31] state 5 steps, including physisorption and surface penetration. Most reduce the process to 3 steps; however, it is not agreed on which ones. Rudman [32] calls them (1) surface process, (2) diffusion and (3) phase transformation. Nahm et. al [33] and Oh et. al [34] state (1) dissociative chemisorption of hydrogen molecules, (2) diffusion of hydrogen atoms through the β -phase and (3) chemical reaction of the hydrogen atoms with the α -phase at its interface between the β -hydride and unreacted core. Whereas Wang et. al [35] argues that the boundary transition step should be included, because it can be rate determining, leading to dissolution as first step. Furthermore, in his opinion, the phase transformation kinetics rather than the chemical reaction kinetics has to be considered. And finally, Ron [24] calls the steps (1) physisorption of an hydrogen molecule, (2) dissociative chemisorption leading to subsurface hydrogen and (3) hydrogen penetration into the bulk.

From these inconclusive statements, different rate determining steps and their models are derived. Fortunately, for fast reactions, the measurement analysis of the reaction rate allows an approximation of the correctly reflected characteristics of the pressure dependence and mechanism functions. For the ratio of their antiderivative (cf. equation (9)), all results have to fall on one line. Then, the pressure dependence and mechanism are reflected correctly and the rate coefficient can be derived (cf. section 2.4).

In this work, different expressions have been calculated for the experiments and the reaction of first order as given in equation (8) [24], [36] was found to fit all results.

$$f(x) = 1 - x \quad (8)$$

The integration of equation (6) with the correctly determined expressions yields a straight line. Its slope corresponds to the rate coefficient, as given in equation (9):

$$\frac{F(x)}{f(p)} = \frac{-\ln(1-x) \cdot p_{eq}}{|p_{eq} - p|} = k(T) \cdot t \quad (9)$$

With experimental results at varied temperatures, the explicit equation for the temperature dependent Arrhenius term for the rate coefficient can be derived, given in equation (10), leading to the pre-exponential factor A in s^{-1} and the activation energy E_a in kJ/mol.

$$k(T) = A \exp\left(-\frac{E_a}{RT}\right) \quad (10)$$

1.3. Literature review

This chapter provides a detailed overview of the literature with regard to metal hydride properties at low temperatures as well as metal hydride applications with focus on thermal power.

1.3.1. Material properties at low temperatures

Originally metal hydrides were investigated as hydrogen storage materials [37]–[40]. But since they release and absorb heat during reaction, more and more investigations deal with thermal applications such as e.g. thermally driven heat pumps at temperatures around 10 °C [41]–[50]. The considered preheating application in vehicles requires even lower reaction temperatures down to -20 °C.

In general, very little characterization data is published at -20 °C for any metal hydride. For AB_2 and AB_5 materials, some of which show fast reaction at low pressure and temperature, the available values are very scarce.

Pressure-concentration isotherms (PCI)

Existing thermodynamic property values are provided here, in particular for the selected materials. This is followed by a discussion of PCI measurement techniques and conclusions for this work.

Thermodynamic properties

The substitution of nickel by aluminum in LaNi_5 was found to lower the equilibrium pressure, to reduce the hydrogen conversion and to increase the reaction enthalpy [51], [52]. This leads to a wide range of derivatives with differing equilibrium properties.

For this study, $\text{LaNi}_{4.85}\text{Al}_{0.15}$ was found to fit the boundary conditions for the heat-generating material perfectly, as described in section 2.1. For this material, only five publications could be found on PCI investigations. Mechi et. al [53] published measurements at 25, 30 and 40 °C. However, this very small temperature range hardly allows conclusion for the relevant temperature range of this work. Higher temperatures were investigated by Selvam et. al [54] and Willers [55], reporting PCIs at 50, 80 and 110 °C. The latter also published values of the reaction enthalpy and entropy of this material. PCI measurements from Dhaou et. al [56] show curves for 30 and 40 °C, which again is a very small range. Wanner [57] investigated the cyclic stability of metal hydrides, including $\text{LaNi}_{4.85}\text{Al}_{0.15}$. He found degradation after over 25,000 cycles, however, could recover the material almost completely by thermal treatment. There, he also published PCIs at 80 °C.

As hydrogen-supplying material, **Hydralloy C5** was identified as promising candidate, although, for this material as well, only few publications of PCIs could be found. Additionally, the exact composition for the commercial name 'Hydralloy C5' differs in literature. An overview of the investigated compositions and their thermodynamics is given in Table 1, including the composition investigated in this work (cf. Appendix A). As shown by Capurso et. al [58], results of an element analysis and thermodynamic measurements might deviate from the supplier specifications. However, all compositions show similar thermodynamics, except for the second material investigated by Skripnyuk and Ron [59] (C5_2), which exhibits significantly higher equilibrium pressures. In particular, a close match can be found between the material of this thesis and the composition of the first material investigated by Skripnyuk and Ron [60] (C5_1) as well as the one published by Herbrig et. al [61]. Therefore, their results can be applied to the material of this work. Skripnyuk mentioned measurements of PCI for this material at -20 °C, however, only published the curve for 20 °C. Herbrig published PCIs for temperatures of 0, 25, 50, 75 and 100 °C. He suggested an exponential polynomial with 15 coefficients for both absorption and desorption. It agreed well with the experiments.

Table 1. Investigated compositions of Hydralloy C5

Author	Ref.	Composition	P _{abs} in bar	T _{abs} in °C	P _{des} in bar	T _{des} in °C
Skripnyuk and Ron	[59], [60]	C5 ₁ : Ti _{0.95} Zr _{0.05} Mn _{1.48} V _{0.43} Fe _{0.08} Al _{0.01}	4.5 ^a	4	3.1 ^a	4
Skripnyuk and Ron	[59]	C5 ₂ : Ti _{0.955} Zr _{0.045} Mn _{1.52} V _{0.43} Fe _{0.12} Al _{0.03}	11.8 ^a	4	5.2 ^a	4
Herbrig et. al	[61]	Ti _{0.95} Zr _{0.05} Mn _{1.55} V _{0.45} Fe _{0.09}	6.0 ^b	4	3.1 ^b	4
Capurso et. al	[58]	supplier specifications Ti _{0.95} Zr _{0.05} Mn _{1.48} V _{0.43} Fe _{0.08} Al _{0.02}	20 ^a	44	12.6 ^a	44
		own measurement Ti _{0.95} Zr _{0.05} Mn _{1.36} V _{0.49} Fe _{0.10} Al _{0.03} Ce _{0.01}	23.3 ^b	44	15.6 ^b	44
			6.8 ^b	4	3.3 ^b	4
This work		Ti _{0.95} Zr _{0.05} Mn _{1.46} V _{0.45} Fe _{0.09}	6.3 ^c	4	3.1 ^c	4

^a Given; ^b Calculated from given enthalpy and entropy; ^c Calculated from PCI-measurement results of this work

In Figure 3, all available thermodynamic data at the center of the PCI plateau is given for the considered materials, including the temperature and pressure range considered in this work (grey area).

As can be seen in this figure, no thermodynamic characteristic is known at temperature below 25 and 0 °C for LaNi_{4.85}Al_{0.15} and C5, respectively. The temperature range in this work considers temperatures 20 to 45 K below these values. Extrapolation of the known data yields only approximated values with no experimental foundation, with increasing uncertainty for increasing distances. Therefore, thermodynamic measurements have been performed in this work for LaNi_{4.85}Al_{0.15} and C5 at very low temperatures.

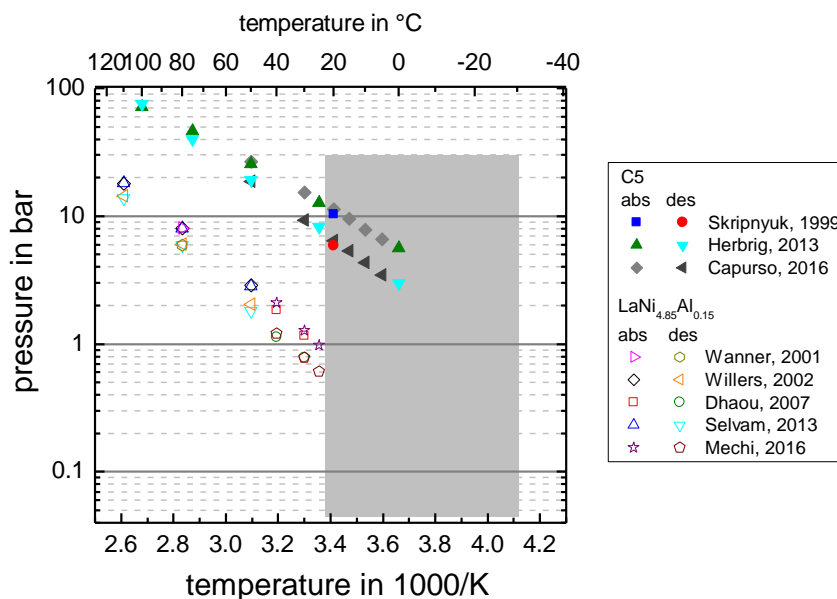


Figure 3. Available thermodynamic data for LaNi_{4.85}Al_{0.15} and C5 [54]–[58], [60], [61]

Measurement of PCIs

The equilibrium for different hydrogen conversion states can be measured either statically or dynamically. The static measurement provides hydrogen to the material and allows sufficient time to reach equilibrium at the set temperature. These measurement steps are repeated several times, each step leading to one point of the PCI, until full conversion is reached. This type of measurement was performed extensively in literature, see e.g. [53], [61]–[64]. Usually, little information is given about the testing procedure, such as the amount and pressure of hydrogen added or the resulting temperature peak inside the material. This, however, might influence the results, as mentioned by Friedlmeier et. al [65].

During a dynamic measurement, hydrogen is supplied continuously resulting in continuous measurement values for the PCI. However, for such a measurement, the equilibrium state is disturbed at any time so the experimental variables have to be chosen with care [65]. This requires a considerable effort for the reactor design and experiment parameters. The heat management of the reactor has to be sufficient in order to ensure almost isothermal conditions and, thus, relate the results to the intended set temperature. The experiment has to be performed at such low hydrogen flow rates, that the material remains very close to equilibrium during reaction. If the flow rate is too high, the measurement is controlled by heat transfer rather than by the equilibrium of the reaction. This leads to pressure values presumably too high or low for absorption and desorption, respectively.

This might be the reason for the reported different results for both measurement types by Goodell et. al [66]. The PCI results on LaNi₅ and FeTi at 25 °C show a considerably larger hysteresis for the dynamic measurements. Although slow hydrogen flow rates were chosen (equivalent to a test duration of 5 days), the comparatively large diameter of the reactor of 15 mm and its tempering (no details provided) might still have limited the heat transfer. Therefore, the mass flow and temperature change have to be examined intensively to ensure appropriate measurements. Even though the measurement principle compares better to the later application, the dynamic method is rarely used in literature. E.g. Muthukumar et. al [67] investigated PCIs dynamically for several metal alloys.

Instead of pure PCI determination, dynamic measurements were also used to determine the behavior of the combination of thermodynamic and kinetics for a particular application by a research group in India [47], [51], [68]. Here, the hydrogen flow rate was adjusted to the

considered application. In the mentioned references, these conditions did not allow the system to reach equilibrium. It has to be emphasized here, that these responses cannot be referred to as thermodynamic properties. Moreover, the results are difficult to generalize for the usage in applications, because the behavior depends strongly on the heat transfer and hence on the geometry of the reactor. Therefore, the determination of thermodynamic and kinetic properties separately leads to deeper insight into the material's behavior.

For precise thermodynamic measurements with either method, the experiments have to be executed with great care. In this work, PCIs for the investigated materials are measured dynamically in order to derive the plateau slope as well as the enthalpy and entropy values at low, to date uninvestigated temperatures. To ensure appropriate results, the equilibrium state and isothermal conditions are considered carefully and the results are compared to literature values at available temperatures.

Reaction kinetics

As for the thermodynamics, in this section, the kinetic properties from literature are reviewed, followed by reported measurement techniques.

Kinetic properties

The investigation of reaction kinetics for fast reacting metal hydrides is difficult, because careful considerations for heat removal and gas supply are required in order to ensure isothermal conditions. Additionally, different equations for the pressure dependence term $f(p)$, required for the calculation of the rate coefficient, lead to different results, as described by Ron [24]. Therefore, kinetic values in literature have to be examined carefully. Even though it is generally assumed that the reaction of metal hydrides possess very fast reaction rates [59], [69] until now, little data exists of metal hydride characteristics at very low temperatures.

The kinetic properties of LaNi_5 have been investigated by many researchers [21], [22], [56], [60], [63], [69]–[71] and cover a temperature range between -6 and 80 °C. However, the results don't particularly agree. Unsurprisingly, no consensus in literature exists on the effect of nickel substitution by aluminum on the reaction rate, either. Whereas some authors state a decreasing effect on the kinetic behavior, such as [20], [63], [72], others suggest an increasing effect, e.g. [21], [22], [44], [56].

For the particular $\text{LaNi}_{4.85}\text{Al}_{0.15}$ used in this work, very little data exists. Only Dhaou et. al [56] and An et. al [21] published kinetic investigations. Dhaou showed the hydrogen conversion over time for 30 and 40 °C at 6 and 10 bar. This temperature is 50 K or more above the lowest temperature considered in the present work. Extrapolation of rate coefficient values results in vague approximation, just as for thermodynamic properties. Additionally, no statement about the isothermal conditions of the material during reaction is provided. The published rate coefficients for desorption are quite close to measurements of LaNi_5 in the same work and also showed a similar slope. However, results for absorption showed a much weaker dependency of the temperature than desorption, which was neither mentioned nor discussed in the publication. If compared to other metal hydrides, such a considerable difference in slope between absorption and desorption wasn't reported yet. Therefore, an extrapolation of these values is even more disputable. Furthermore, the used pressure dependence function for the kinetic fit ($f(p) = \left(\frac{p_{init}}{p_{mid}} - 1\right) \frac{\ln(p/p_{eq})}{(p/p_{eq})}$) differs from the ones used in other studies and in this work (cf. equation (7)), which also might cause a deviating trend.

In the work of An et. al [21], only hydrogen conversion measurements over time were shown without comparable values for rate coefficients. Again, no statement about isothermal conditions was given. Compared to Dhaou, the results for both LaNi_5 and $\text{LaNi}_{4.85}\text{Al}_{0.15}$ were much lower.

From this discussion, it is concluded that the data from literature for $\text{LaNi}_{4.85}\text{Al}_{0.15}$ is contradictory and hence will be determined at temperature down to -20 °C in this work.

For the other material considered in this work, C5, only one single publication was found on kinetic investigations. The already mentioned work of Skripnyuk and Ron [60] presented results down to a temperature of -20 °C. As discussed in the literature review for PCIs, this material matches well the composition of the one investigated in this work. The slopes of the rate coefficients for absorption and desorption were in the same range. Desorption of LaNi_5 was found to be fairly slower than of C5. In [24], Ron suggested a normalized pressure dependence method (NPDM), which the work in [60] follows. Here, the pressure dependence function is discussed thoroughly and a procedure is described to obtain

comparable results. These kinetic properties are therefore considered reliable and are used for this work.

For a better overview, the discussed rate coefficients for both materials are given in Figure 4. From the given curve by An, a rate coefficient was calculated for $\text{LaNi}_{4.85}\text{Al}_{0.15}$ and LaNi_5 as part of this thesis using the pressure dependence function given by equation (7). Unfortunately, the temperature at which the measurement of $\text{LaNi}_{4.85}\text{Al}_{0.15}$ took place is mentioned contradictory in the publication and was stated to be either at 30 or 40 °C, hence, the result is shown for both temperatures. Since all references did also measurements on LaNi_5 , these values are also included for comparison of the different studies.

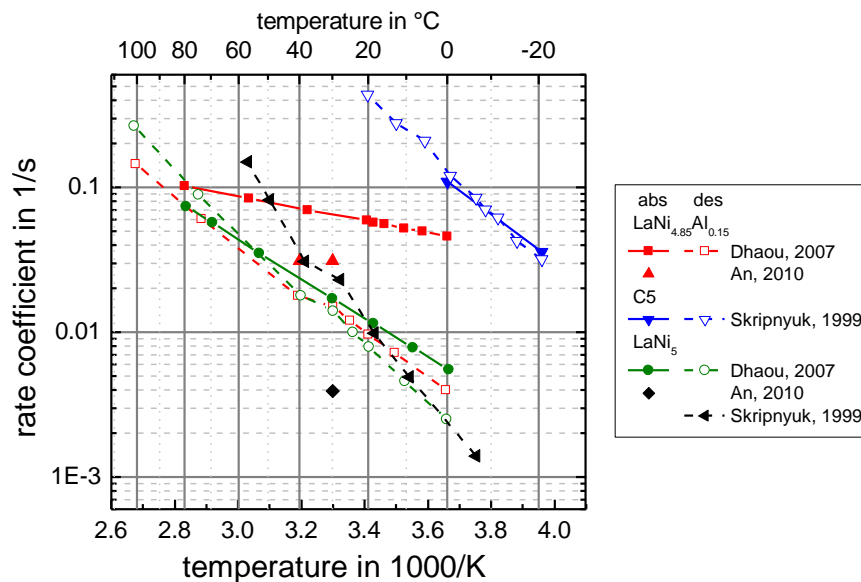


Figure 4. Available kinetic data for $\text{LaNi}_{4.85}\text{Al}_{0.15}$, C5 and LaNi_5 [21], [56], [60]

From this figure, both the scarce and contradictory rate coefficient results can be seen. For C5, the published data from Ron is used. Since no reliable data on the reaction rates of $\text{LaNi}_{4.85}\text{Al}_{0.15}$ exists, it has to be obtained as part of this work.

Determination of kinetics

The measurement procedure has to exclude limitations of the reaction other than the kinetics in order to yield correct results. In particular for the fast reaction rates of the materials considered in this work, careful considerations have to ensure correct measurements. If in particular heat flow limitations are underestimated, reported results can divergent greatly, as discussed e.g. by Goodell and Rudman [73]. The normalized

pressure dependence method (NPDM) suggested by Ron [24] is used to determine the kinetic values. The following conditions are suggested there:

- Temperature change of the material should be limited to ± 1 K, e.g. by the thermal ballast method
- Mass transfer of hydrogen through the reaction bed should be high so the gas transport does not limit the reaction
- A reaction order or mechanism must be defined
- Within the considered temperature range, the reaction process has to obey the Arrhenius temperature dependence
- The hydrogen should be converted within the plateau region ($\alpha+\beta$ region)

The restriction on the maximal temperature change is strict compared to other work. Rudman [32], for example, discusses a temperature change of ± 10 K. In order to be able to refer the derived rate coefficient to one temperature, the maximal temperature change allowed in this work is ± 3 K.

The careful consideration of possible limitations of the reaction is further discussed in section 2.4 and the results are discussed accordingly.

Conclusion

From this literature overview, the temperature range of all available data for both materials used in this work is depicted in black in Figure 5. However, in orange, the range is indicated, at which data is necessary for this study but missing from literature.

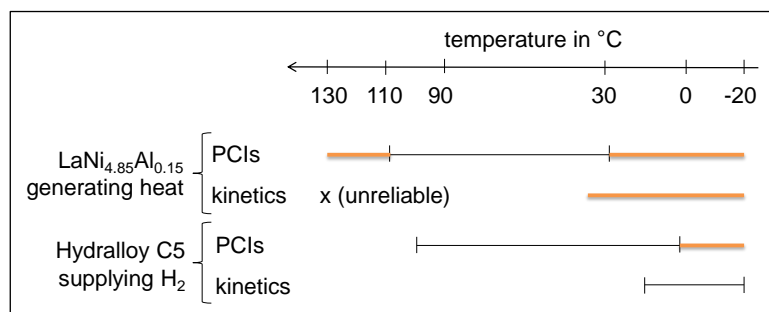


Figure 5. Overview of usable (black) and missing (orange) data on properties for LaNi_{4.85}Al_{0.15} and C5

The thermodynamic properties of both materials could only be estimated by extrapolation but have to be specified by measurements in this work. The rate coefficient of C5 can be

taken from literature and shows fast reaction rates. This is crucial to know in advance since this material cools down even further when supplying hydrogen via desorption. For $\text{LaNi}_{4.85}\text{Al}_{0.15}$, however, no reliable data is available and the rate coefficients have to be determined for the low temperatures considered.

1.3.2. Thermal applications of metal hydrides

Thermal power investigations

In literature, there are two basic operation modes used to run thermal metal hydride systems. If a hydrogen source is available, one metal hydride can react in an open system, where hydrogen is supplied and released from/to the infrastructure. In case no hydrogen infrastructure is available (e.g. ICE vehicles), it has to be provided by another metal hydride. The hydrogen does not cross the systems border; hence this system is referred to as closed. Such a closed system is also considered in the present thesis.

The scheme of operation of a closed system is depicted in Figure 6. The upper part shows the discharge. Both materials start at ambient temperature. As can be seen in the van't Hoff plot on the right hand side, at the same temperature, the hydrogen-supplying material (MH2) has a higher equilibrium pressure than the heat-generating material (MH1). After connecting both materials, e.g. by opening a valve, hydrogen is desorbed from MH2 and absorbed by MH1 until full conversion is reached. The desorption heat is taken from the ambient and the absorption heat can be used for preheating purposes.

For regeneration, waste heat is supplied to MH1. The pressure rises according to its equilibrium. The temperature level of the waste heat has to lead to a higher pressure in MH1 than in MH2 at ambient temperature. Thus, the hydrogen can be reabsorbed in MH2 and the absorption heat is released to ambient. After complete conversion, the valve is closed and both materials cool down to ambient. The thermal energy is stored as chemical potential free of loss for as long as required.

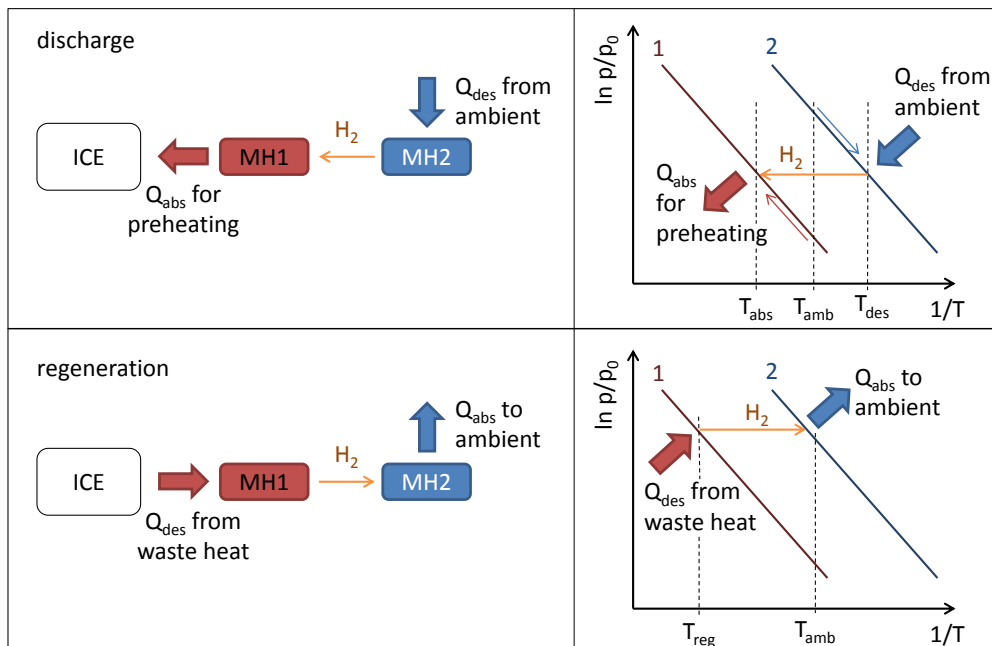


Figure 6. Schema of discharge and regeneration of a closed metal hydride system

Since desorption of hydrogen requires heat, cold for air conditioning or refrigeration can also be provided. For continuous air conditioning, two sets of reactor(s) are used in parallel; one generates cold while the other regenerates. Therefore, both heating and cooling effects are investigated in literature. In both cases, the reaction and the reactor design pose similar requirements; however, for air conditioning, most reactions take place at temperatures above 0 °C. For that reason, some suitable work on cold generation is included here.

Several reviews of metal hydride applications have been published. E.g. Sandrock and Bowman [74] provided a detailed overview of many different metal hydride applications, including closed thermodynamic systems. Muthukumar and Groll [41] published a review of heating and cooling systems based on metal hydride, however, focused on cooling applications. The review of Bhuiya et. al [42] focused on non-storage applications of metal hydrides. A detailed overview of cooling applications was given. The mentioned thermal storages, though, only focused on high temperature applications based on Mg-hydride.

No published thermal power values on **heat generation at low temperatures** in relevant scale could be found, except for the authors own work [75]. The patent of Docter et. al [76] claimed preheating a fuel cell with TiFe from subzero temperature, however, no values or experiments were provided.

At **higher temperatures**, though, some work on coupled metal hydride reactions is published. Interesting work on preheating a vehicle component was published by Golben et. al [77] and DaCosta et. al [78]. In a coupled reaction of a Nb-stabilized β -Ti alloy and $\text{MmNi}_{4.5}\text{Al}_{0.5}$, high specific thermal power of 92 kW/kg was achieved to preheat an internal combustion engine catalyst. However, heat was generated at up to 400 °C with a regeneration temperature of 600 °C, and hence at much higher temperatures than considered here.

Investigations at 30 °C by Park et. al [44], although not focused on thermal power, yielded a value of 280 W for the single reaction of $\text{LaNi}_{4.75}\text{Al}_{0.25}$. The investigated amount of metal hydride was 80 g, mixed with copper and tin powder and compressed to pellets. The reactor was designed as a simple tube and extrapolation would decrease the specific thermal power. Nonetheless, linear extrapolation would lead to 3.5 kW/kg, but the reaction at 20 bar is hardly comparable to coupled reactions. When the reaction was coupled with $\text{Ca}_{0.6}\text{Mm}_{0.4}\text{Ni}_5$, this value decreased by almost 90 % to 32 W. The theoretical up-scale of the 80 g-experiment yields a specific thermal power of 400 W/kg for the coupled reactions, despite of the comparably high temperature of 30 °C.

A so called thermal battery was developed by Fang et. al [79]. The work considered both heat and cold generation for cabins of electric vehicles. The coupled reactions of TiMn_2 catalyzed MgH with Hydralloy C ($\text{TiMn}_{1.5}\text{V}_{0.62}$) generated a peak thermal power of 320 W_{heat} (125 W_{cold}). Although, mathematically, a high specific thermal power of 6.4 kW/kg would have been achieved, the reactor design of a tube with 19 mm inner diameter might not allow easy scale-up from the 50 and 190 g of metal hydride, respectively. Additionally, a high regeneration temperature of 390 °C was required.

A fairly comparable work is the investigation of two LaNi-based materials with regeneration temperature level of around 180 °C by Qin et. al [80]. They also looked at both heat and cold generation. The results for the cycle performance test starting from 20 °C yielded thermal peak power for heat generation of 0.48 kW/kg (cold generation: 0.25 kW/kg; 7.7 W/kg for the whole cycle).

More work can be obtained in literature for **cold generation from room temperature**.

Coupled reactions providing cold at subzero temperature were investigated by e.g. Imoto et. al [45], and the already mentioned work of Fang et. al [79]. Imoto investigated two LaNi-based materials which reached temperatures below $-20\text{ }^{\circ}\text{C}$ using a regeneration temperature of $150\text{ }^{\circ}\text{C}$. However, 90 kg of alloy were necessary to reach a thermal power of 1.8 kW.

Both Linder and Kulenovic [81] and Weckerle et. al [82] reported high cooling power values. Linder reported $2.1\text{ kW/kg}_{\text{peak}}$ and $1.1\text{ kW/kg}_{\text{mean}}$ power for an 800 g-scale experiment. Cold at $13\text{ }^{\circ}\text{C}$ was generated at $30\text{ }^{\circ}\text{C}$ ambient temperature. Weckerle achieved a mean power of 1.3 kW/kg at $10\text{ }^{\circ}\text{C}$ for 360 g of Hydralloy C5, the same material as used in this work. However, both references investigated open systems with regeneration pressure of 50-30 bar, which is difficult to compare to coupled reactions.

The approach by Linder et al. [43] investigating the thermal power achievable of coupled reactions at $130\text{ }^{\circ}\text{C}$ regeneration temperature is best comparable to the preheater of this work. The experiments of around 900 g of material yielded 780 W/kg at $20\text{ }^{\circ}\text{C}$ at an ambient temperature of $28\text{ }^{\circ}\text{C}$.

Many other publications exist. They are summarized in Table 2, without claiming to be exhaustive. Where not provided, the specific thermal power values have been calculated from the given data in all conscience. Nonetheless, in some cases, the specific thermal power values are not comparable due to the lack of information about reactor or experiment design.

From this discussion, the following can be concluded. No work on heat generation at temperatures below $20\text{ }^{\circ}\text{C}$ has been published. The only comparable investigations to the preheater of this work yielded specific thermal power values of $480\text{ W}_{\text{heat}}/\text{kg}$ by Qin and $780\text{ W}_{\text{cold}}/\text{kg}$ by Linder, however, both at $20\text{ }^{\circ}\text{C}$. Additionally, the identified regeneration temperature level for ICEs of 90 to $130\text{ }^{\circ}\text{C}$ in this work present the lowest regeneration energy used in all investigations. Therefore, the intended investigation of coupled reactions at temperatures as low as $-20\text{ }^{\circ}\text{C}$ will greatly enlarge the available data.

Table 2. Overview of metal hydride thermal power applications in literature, focusing on low temperatures

	Author	Year	Ref.	T _{use} in °C	T _{amb} in °C	Regen- eration	P _{th} in W/kg	System	Used metal hydrides	Mass	Comment
Heat storage	Golben, DaCosta, Sandrock	1997	[77]	400	25	600°C	92,000 (5s)	closed	Nb-stabilized β-Ti alloy/ MmNi _{4.5} Al _{0.5} (HY-STORE 208)	1 kg β-Ti	
	Gerstmann, Golben	1999	[83]	400	RT	diesel flame	316 W	closed		77 g 1743 g	diesel cook stove
	Qin, Chen, [...] Yang	2007	[80]	150	20	180°C	480 (peak) 260 (mean)	closed	LaNi _{4.61} Mn _{0.26} Al _{0.13} / La _{0.6} Y _{0.4} Ni _{4.8} Mn _{0.2}	2.75 kg 2.75 kg	both heat + cold
	Docter, Frank, [...] Mueller	2008	[76]	-30 ... 50				open	TiFeH		patent
	Park, Kim, [...] Gawlik	2009	[44]	30	30	70/ 80°C	400	closed	LaNi _{4.75} Al _{0.25} / Ca _{0.6} Mm _{0.4} Ni ₅ , both coated + compressed	80 g 80 g	
	Park, Kim, [...] Gawlik	2009	[44]	30	30	20 bar	3500	open	LaNi _{4.75} Al _{0.25} coated + compressed	80 g	
	Fang, Zhou, [...] Kekelia	2015	[79]	228	25	390°C	6,400 (peak)	closed	MgH+TiMn ₂ , partially + ENG/ TiV _{0.62} Mn _{1.5} = C	50 g 190 g	both heat + cold
	Liu, Li, [...] Wang	2016	[84]	20 ... 60		30 bar		open	LaNi ₅	220 g	focus on storage
Cold converter	Ron	1984	[85]	-2	20	380-400°C	250	closed	LaNi _{4.7} Al _{0.3} + 18% Al/ MmNi _{4.15} Fe _{0.85} + 18% Al		not cycling-stable
	Golben, Lee Huston	1989	[86]				0.16	closed	LaNi _{4.5} Al _{0.5} / (CFM)Ni ₅	16.2 kg 16.2 kg	report
	Lee, Kim, Lee	1995	[87]			>220°C	270	closed	Zr _{0.9} Ti _{0.1} Cr _{0.9} Fe _{1.1} / Zr _{0.9} Ti _{0.1} Cr _{0.6} Fe _{1.4}		
	Imoto, Yonesaki, [...] Saito	1996	[45]	< -20		150°C	45	closed	LaNi _{4.6} Al _{0.3} Mn _{0.1} / La _{0.6} Y _{0.4} Ni _{4.8} Mn _{0.2}	90 kg total	
	Izhvanov, Solovey [...] Shanin	1996	[88]				234	closed	LaNi _{4.6} Al _{0.4} / MmNi _{4.85} Fe _{0.15}	1.5 kg 1.5 kg	
	Kanhg, Park, Lee	1996	[89]	20	30	150°C	175	closed	MmNi _{4.15} Fe _{0.85} / LaNi _{4.7} Al _{0.3}	5.7 kg 4.5 kg	

Table 2. Overview of metal hydride thermal power applications in literature, focusing on low temperatures (continued)

	Author	Year	Ref.	T _{use} in °C	T _{amb} in °C	Regeneration	P _{th} in W/kg	System	Used metal hydrides	Mass	Comment
Cold converter	Gopal, Murthy	1999	[90]	5 ... 15		110-130°C	30-45	closed	ZrMnFe/ MmNi _{4.5} Al _{0.5}	700 g 800 g	
	Willers, Wanner, Groll	1999	[91]	0 ... 10		152-240°C	360 W (mean)	closed	8 different LaNi-based materials, Ti _{0.98}		multi-hydride thermal wave
	Chernikov, Izhvanov, [...] Shanin	2002	[92]	< 4			100	closed	LaNi _{4.6} Al _{0.4} / MmNi _{4.15} Fe _{0.85}	1.5 kg 1.5 kg	
	DaCosta, Golben, Tragna	2002	[78]	7	38	200°C	380 (peak) 190 (mean)	closed		14 kg AB5, 30 kg sys	
	Klein, Groll	2002	[93]	2	125	310°C	116	closed	MmNi _{4.91} Sn _{0.15} / LaNi _{4.1} Al _{0.52} Mn _{0.38} / Ti _{0.99} Zr _{0.01} V _{0.43} Fe _{0.09} Cr _{0.05} Mn _{1.5}	max. 1.9 kg	double stage concept
	Ni, Liu	2007	[49]	2 ... 7		150°C	89	closed	LaNi _{4.61} Mn _{0.26} Al _{0.13} / La _{0.6} Y _{0.4} Ni _{4.8} Mn _{0.2}	2.75 kg	
	Qin, Chen, [...] Yang	2007	[80]	0.4	20	180°C	250 (peak) 90 (mean)	closed	LaNi _{4.61} Mn _{0.26} Al _{0.13} / La _{0.6} Y _{0.4} Ni _{4.8} Mn _{0.2}	2.75 kg 2.75 kg	both heat + cold
	Linder, Mertz, Laurien	2010	[43]	10, 15, 20	28	130°C	780 (20°C, mean)	closed	LmNi _{4.91} Sn _{0.15} Ti _{0.99} Zr _{0.01} V _{0.43} Fe _{0.09} Cr _{0.05} Mn _{1.5}	948 g 800 g	
	Linder, Kulenovic	2011	[81]	13	30	50 bar	2,125 (peak) 1,125 (mean)	open	Ti _{0.99} Zr _{0.01} V _{0.43} Fe _{0.09} Cr _{0.05} Mn _{1.5}	800 g	
	Fang, Zhou, [...] Kekelia	2015	[79]	-12	25	390°C	700	closed	MgH+TiMn ₂ partially + ENG/ TiV _{0.62} Mn _{1.5}	50 g 190 g	both heat + cold
Weckerle, Buerger, Linder	2017	[82]	10, 20		30 bar	1,310 (10°C, mean)	open	Hydralloy C5	360 g		

High thermal power reactors

For the considered preheating application, the energy density should be high to realize a small system. However, since the required amount of thermal energy during cold start is comparatively small but has to be provided within a very short period, the most important property of the system is the specific thermal power.

For high thermal power, the reacting materials have to possess very fast reaction kinetics, which might be a challenge at the considered temperatures. Besides, the reactor design has to allow for fast transfer of both reaction gas and heat (of reaction). However, metal hydride powders have low thermal conductivity in the order of 1 W/(mK) [94]. There are several ways to improve the thermal conductivity of the reaction bed. E. g. a mixture with expanded natural graphite and compression to composites improves the effective thermal conductivity of the bed by more than factor ten even after long-term cycling [95], [96]. Another possibility to decrease thermal resistance is to reduce the distance from the origin of reaction to the heat transfer fluid by reducing the bed width. This method was followed in this work. Additionally, for high thermal power, the overall heat transfer of the whole reactor has to be considered. Here, the main goal is to increase the heat transfer surface area between the metal hydride powder and the heat transfer fluid. However, more passive mass of the reactor leads to a smaller temperature increase by the heat release and, additionally, increases the overall system mass. Hence, the ratio of reactor to metal hydride mass, as given in equation (11), should be kept small.

$$r = \frac{m_{reactor}}{m_{MH}} \quad (11)$$

Additionally, for sufficient gas transport, the design should realize short gas penetration distances.

Basically, two types of heat exchangers exist, namely plate or tube bundle heat exchanger. Both types are used for thermal sorption systems, with special attention to gas penetration. The resulting thermal power values, however, are very difficult to compare, because the reaction rate of the system depends additionally on the used materials and their boundary conditions. Therefore, the following review only describes different designs used in literature without comparison.

A **plate heat exchanger** with increased heat transfer area by fins was investigated by Oi et. al [97]. In their comparison with a heat transfer model, they emphasized the importance of detailed knowledge of the material properties for appropriate reactor design. In the assessment of Sharafian and Bahrami [98], albeit for adsorption cooling systems, plate heat exchangers reached reactor to reacting material ratios between 2.45 and 9. An optimized design with small gap widths of 1.5 mm was presented by Weckerle et. al [82], reaching a thermal mean power of 1.31 kW/kg for air conditioning at 10 °C.

The plate design allows easy scale-up by adding more plates and is therefore fully modular. However, the design is limited in pressure and plate size due to sufficient gas transport.

In **tube bundles**, the reaction bed is usually on the shell side for better room use. Gas can be supplied either from the center or from the outside of the bundle. The former was investigated in several studies [90], [93], [99] and involves a porous tube allowing hydrogen to penetrate the bed from the inside out. Alternatively, gas can be supplied from the outer diameter, either through a filter, allowing penetration over the complete perimeter, as investigated e.g. in [43], [50], or by a gap at the top of a horizontal tube bundle for penetration over the whole diameter, as used in the present work. The heat transfer area can be increased either by using fins or a compact tube arrangement. As found by Afzal et. al [100], most researchers use fins to improve the thermal conductivity.

The modularity of tube bundle heat exchanger is limited, because a change in outer diameter leads to different proportions e.g. for gas penetration. However, the tube design allows better stability at high pressures or stress from expanding metal hydride during absorption. Therefore, this robust design is preferable in mobile applications and is used for experiments in laboratory scale in this thesis.

1.4. Challenge of coupled reactions

As shown in Figure 6, in a closed system that is only thermally connected to the surrounding, the reaction gas has to be supplied by a second metal hydride (cf. section 1.3.2). These coupled reactions are extremely complex, because they depend on many influencing factors and additionally presuppose each other. Starting from the initial (ambient) temperature, the heat-generating material strives to increase its temperature at the given supply pressure

according to its equilibrium. This, however, is influenced by the actual material temperature, hydrogen pressure and transformed fraction. The material temperature is influenced by the heat exchange in the reactor. Furthermore, the reaction rate also depends on the temperature and additionally on the intrinsic rate coefficients of the material. And, moreover, the hydrogen pressure depends on the reaction of the hydrogen-providing material, which, again, depends on all the other factors mentioned. This linkage of the two parallel, interdependent reactions is illustrated with the help of a van't Hoff-plot in Figure 7.

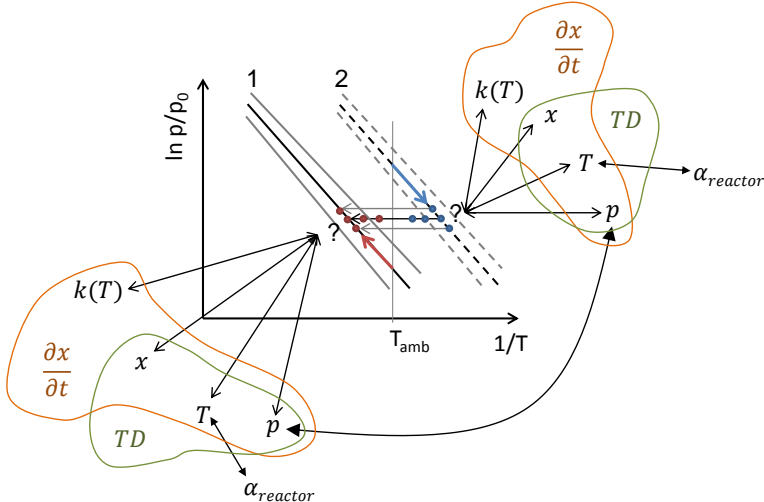


Figure 7. Dependencies of the interlinked coupled reactions

This complex correlation has to be understood for the development of a preheater and is therefore subject matter of the systematic investigations in this work. Hereof, the aim of thesis is derived.

1.5. Aim of thesis

Running internal combustion engines below their operation temperature during cold start causes 60 - 80 % of all pollutants of the whole ride. These emissions could be reduced drastically by preheating the vehicle components.

A thermal energy storage based on metal hydrides can provide high thermal energy density and reaction rates and be discharged on demand and recharged by waste heat without the requirement of thermal insulation. These advantages could lead to an easy (pre-) heating system without additional energy consumption other than a small increase of the vehicle mass.

However, the system of two coupled reactions is extremely complex. Additionally, the automotive boundary conditions during cold start pose severe restrictions on the thermochemical system. Since reaction rates decrease with decreasing temperature, the achievable specific thermal power might face limitations. Little is known about metal hydrides at subzero conditions. This includes both material properties and laboratory scale thermal power investigations.

In particular for coupled metal hydride reactions down to $-20\text{ }^{\circ}\text{C}$ for heat applications, data is hardly available. At comparable conditions, the highest specific thermal power value for coupled reactions was $480\text{ W}_{\text{heat}}/\text{kg}$ by Qin [80] and $780\text{ W}_{\text{cold}}/\text{kg}$ by Linder [43], however, both at $20\text{ }^{\circ}\text{C}$. Moreover, no systematic investigation of possible influencing factors has been performed yet. This knowledge, however, is pivotal for appropriate preheater design for vehicle cold start phases.

Therefore, this thesis investigates the influencing factors on coupled metal hydride reactions at temperatures as low as $-20\text{ }^{\circ}\text{C}$ for preheating vehicle components regarding the thermal power. In particular, the following questions are examined:

- Which specific thermal power can be achieved with metal hydrides at automotive boundary conditions, in particular at low temperatures?
- What are the influencing factors on the specific thermal power?
- What conclusions can be drawn for future applications of metal hydrides in vehicles?

In order to answer these questions, first, the potential materials have to be characterized in the temperature range of question. This allows detailed interpretation of the subsequent investigation in laboratory scale of almost 1 kg of metal hydride. From experiments of the single reactions, conclusions at constant boundary conditions can be drawn. Then, the achievable specific thermal power of the two coupled reactions at low temperatures is investigated and the factors of influence are identified. From this, a future application of metal hydride in vehicles can be outlined in order to pave the way for emission reduction in the short and carbon-free mobility in the long run.

2. Material characterization

In order to investigate the achievable specific thermal power of metal hydrides at automotive boundary conditions, first, appropriate materials have to be selected. Due to the lack of published properties in the given temperature range, the chosen materials then have to be characterized. For this purpose a test bench was designed which is able to provide the respective temperature and pressure range of question for both pressure-concentration isotherms (PCI) and reaction rate measurements. PCIs were measured for both materials down to $-30\text{ }^{\circ}\text{C}$ and kinetic properties of the heat-generating material were investigated down to $-20\text{ }^{\circ}\text{C}$. Details on the material selection, the experiments and the results are given in this chapter.

2.1. Material selection

Since the suitability of the materials form the basis for the thermal storage, great care has to be taken when defining the boundary conditions and requirements and scanning the literature. For the selection, all material properties are taken from literature. However, as discussed in the literature review section, data on metal hydride properties below $0\text{ }^{\circ}\text{C}$ are hardly available. Therefore, an extrapolation of available data to lower temperatures was necessary. The correctness of the extrapolated data has to be verified for the selected materials by own measurements. Due to the demand for very high specific thermal power, only materials with very fast reaction kinetics are considered.

As can be seen from Figure 6 in section 1.3.2, the maximal distance of the equilibria of the coupled materials is given by the distance of ambient and regeneration temperature. However, hysteresis and non-ideal plateau slope decrease the usable temperature difference. The exact value depends on the considered materials and the quality of the available data in the considered temperature range. This theoretical consideration does not take pressure losses etc. into account.

As described in the introduction, the considered boundary conditions are heat generation at temperature levels of -20 to $20\text{ }^{\circ}\text{C}$ and regeneration at 90 to $130\text{ }^{\circ}\text{C}$. The pressure level of the coupled reactions can be chosen freely. However, the reactors have to withstand this pressure. Therefore, a maximal pressure level of 30 bar was chosen to limit the necessary amount of reactor material.

The equilibrium values of the materials have to satisfy the following conditions (cf. Figure 8): The absorption pressure of the heat-generating material (MH1) at ambient temperature has to be below the desorption pressure of the hydrogen-supplying material (MH2) at the same temperature, so the hydrogen tends to MH1 ($p_{\text{MH1,abs}}(T_{\text{amb}}) < p_{\text{MH2,des}}(T_{\text{amb}})$). Additionally, in order to ensure a preheating effect, the temperature of MH1 at the pressure level of MH2 has to be well above ambient temperature ($T_{\text{MH1,abs}}(p_{\text{MH2,des}}(T_{\text{amb}})) \gg T_{\text{amb}}$). For regeneration, the pressure level of MH1 at the waste heat level of the internal combustion engine has to be above the pressure level of MH2 at ambient temperature, so the hydrogen flows back into MH2 ($p_{\text{MH1,des}}(T_{\text{reg}}) > p_{\text{MH2,abs}}(T_{\text{amb}})$). Also, the absorption heat level of MH2 at the regeneration pressure level of MH1 has to be above ambient temperature in order to release it to ambient ($T_{\text{MH2,abs}}(p_{\text{MH1,des}}(T_{\text{reg}})) > T_{\text{amb}}$).

After an intensive literature review, mainly two types of metal hydride alloys were found to both laying in the considered range and showing fast rate coefficients. For the heat-generating material, some derivatives of LaNi_5 with aluminum show high reaction rates and appropriate thermodynamics. The hydrogen-providing material requires even higher rate coefficients, because it will cool below ambient temperature when desorbing. Some AB_2 -alloys with large titanium content, so called Hydralloy C-materials, could satisfy the requirements. A detailed look at the thermodynamic properties led to the following chosen pair of materials (see section 1.3.1 for properties):

- $\text{LaNi}_{4.85}\text{Al}_{0.15}$ from WholeWin (China) as heat-generating material
- Hydralloy C5² ($\text{Ti}_{0.95}\text{Zr}_{0.05}\text{Mn}_{1.46}\text{V}_{0.45}\text{Fe}_{0.09}$) from GfE Metalle und Materialien GmbH (Germany) as hydrogen-providing material

Their thermodynamic properties are given in the van't Hoff-plot in Figure 8 (extrapolated from literature data).

² Hydralloy C-materials are numbered according to their percentage of other components than titanium. Therefore, $\text{Ti}_{0.95}\text{Zr}_{0.05}\text{Mn}_{1.46}\text{V}_{0.45}\text{Fe}_{0.09}$ – the material used in this study – is called Hydralloy C5[®] and is referred to as 'C5' in this work

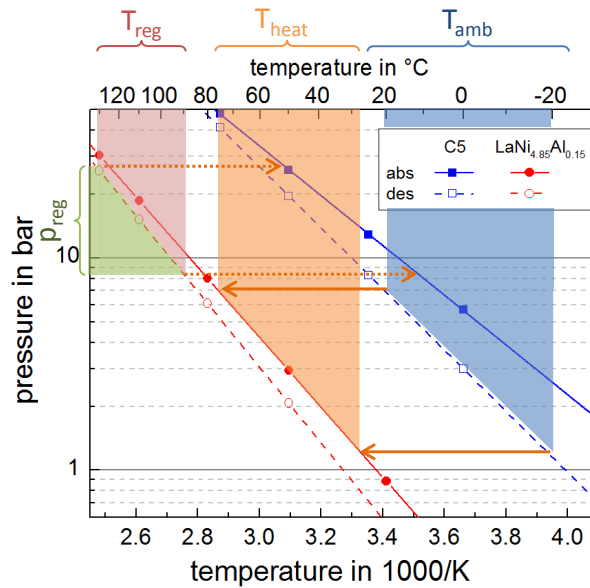


Figure 8. Extrapolated equilibrium data for $\text{LaNi}_{4.85}\text{Al}_{0.15}$ [54] and C5 [61]

For coupled reactions, the ambient temperature determines the hydrogen pressure for heat generation. If C5 desorbs hydrogen at $-20\text{ }^{\circ}\text{C}$, the resulting pressure leads to heat production of around $25\text{ }^{\circ}\text{C}$ if absorbed by $\text{LaNi}_{4.85}\text{Al}_{0.15}$ (indicated by the lower solid orange arrow). The desorption pressure of C5 at $20\text{ }^{\circ}\text{C}$ leads to an absorption temperature of $75\text{ }^{\circ}\text{C}$ of $\text{LaNi}_{4.85}\text{Al}_{0.15}$ (upper solid orange arrow). Hence, heat can be generated theoretically between 25 and $75\text{ }^{\circ}\text{C}$. At a regeneration temperature of $130\text{ }^{\circ}\text{C}$, the pressure of desorbed hydrogen from $\text{LaNi}_{4.85}\text{Al}_{0.15}$ results in an absorption heat level of $50\text{ }^{\circ}\text{C}$ in C5 which can be dissipated to ambient (upper dotted orange arrow). At temperatures of $90\text{ }^{\circ}\text{C}$ the absorption heat of C5 can only be dissipated at ambient temperatures below $10\text{ }^{\circ}\text{C}$ (lower dotted orange arrow). Complete regeneration might therefore not be possible in all cases.

As mentioned earlier, the hydrogen-supplying material C5 is known to possess fast reaction kinetics. This is particularly important, because desorption leads to a decrease in temperature and hence in reaction rate. For the heat-generating material, the absorption heat increases the temperature and consequently its reaction rate. However, comparably high rate coefficients are necessary for a high thermal power. Due to the lack of data, the kinetic properties of $\text{LaNi}_{4.85}\text{Al}_{0.15}$ as well as the pressure-concentration isotherms for both materials are obtained as part of this work.

2.2. Methodology and test bench for material characterization

This chapter provides detailed information about the procedures for thermodynamic and reaction rate measurements as well as the test bench built for the material characterization.

The chosen material pair for this work, $\text{LaNi}_{4.85}\text{Al}_{0.15}$ and C5, has to be characterized in the lower temperature range due to the lack of published properties. For $\text{LaNi}_{4.85}\text{Al}_{0.15}$, no thermodynamic values below 25 °C have been published and no reliable kinetic data is available. The rate coefficients of C5 have been investigated down to -20 °C [60], which will be used in this work, however, PCI measurements are only published down to 0 °C. Precise knowledge about the intrinsic properties is pivotal for well interpretation of laboratory scale experiments and identifying the factors influencing the specific thermal power.

Therefore, the necessary pressure-concentration isotherms (PCI) for both materials as well as the kinetic data for $\text{LaNi}_{4.85}\text{Al}_{0.15}$ in the considered temperature range are obtained in this work. PCIs were measured between -20 and 130 °C for $\text{LaNi}_{4.85}\text{Al}_{0.15}$ and -30 and 35 °C for C5, which cools further during desorption. The reaction rates of $\text{LaNi}_{4.85}\text{Al}_{0.15}$ are measured between -20 and 40 °C.

2.2.1. Methodology

The characterization of metal hydrides considers hydrogen conversion at a certain temperature. Therefore, for successful measurements, almost isothermal conditions for the metal hydride are crucial in order to relate the property to one temperature value. In particular for fast reactions like the considered ones, this requires careful experimental and reactor design. Figure 9 shows the schematic of metal hydride property measurements. The hydrogen is provided in a large volume at known temperature and pressure, the so called Sieverts' volume (left). It can be connected to the reactor containing the metal hydride at a certain temperature (right). Here, temperature and pressure are measured, too. For dynamic pressure-concentration isotherm measurements, the hydrogen is supplied slowly to the material via a flow rate control to ensure (almost) equilibrium at any time. In contrast, for reaction rate measurements, the hydrogen is provided instantly so the reaction is not limited by the hydrogen supply. Additionally, the design of the test bench and reactor has to exclude limitations of the reaction by gas or heat transfer. All volumes of the test bench have to be known precisely in order to obtain correct hydrogen conversion values.

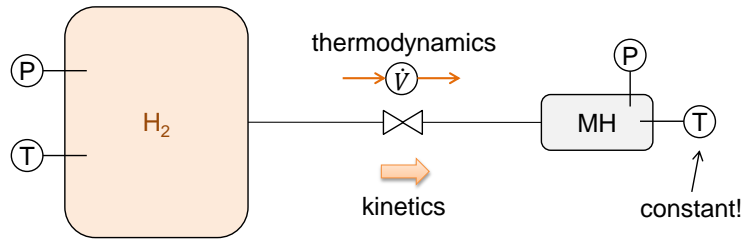


Figure 9. Schematic of thermodynamic and reaction rate measurements

All metal hydrides are handled in a glove box with inert argon atmosphere. The activation of the materials was performed inside the same reactor at which the characterization measurements took place, in order to prevent passivation or side reactions. The experiments were run after activation of the material by pressure swing at respective temperatures.

2.2.2. Test bench

A test bench was designed and built to measure the thermodynamic and kinetic properties of $\text{LaNi}_{4.85}\text{Al}_{0.15}$ and C5 in the temperature range of -30 to 130 °C and a pressure range up to 100 bar (used up to 40 bar). Figure 10 shows the layout of the test bench. For free space measurements, an argon supply is provided (up to 15 bar).

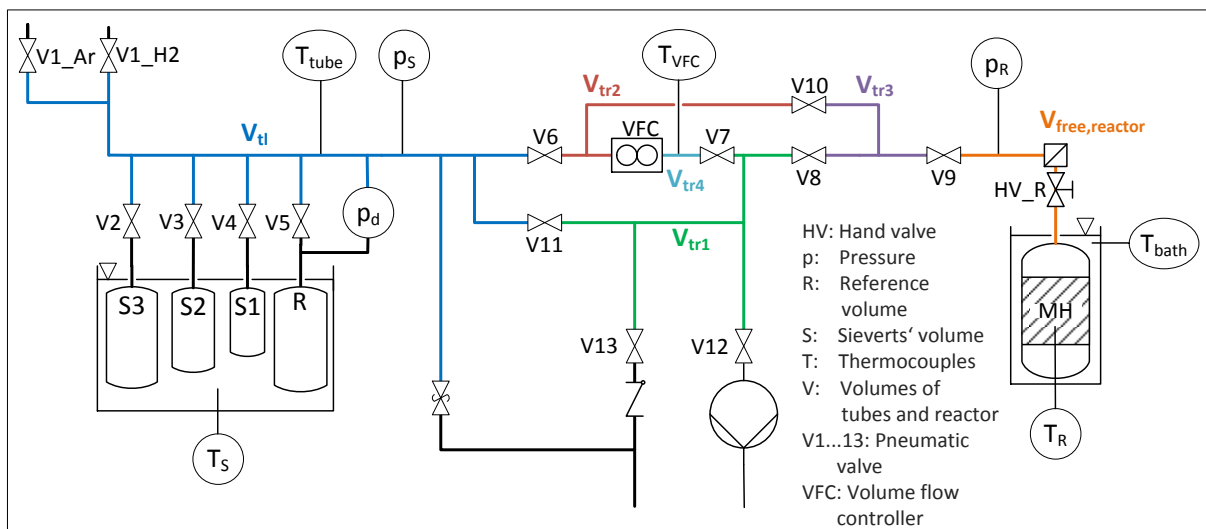


Figure 10. Layout of characterization test bench

Three different Sieverts' volumes or their combination can be used for measurements, depending on the desired pressure difference and mass of the sample. The pressure drop in this volume is measured to obtain the amount of absorbed hydrogen. For the PCI measurements, a differential pressure sensor (p_d) for pressure drops up to 10 bar was used. The reaction rate measurements were balanced via an appropriate pressure sensor (p_s) according to the expected pressure drop (see Table 3). The volumes are surrounded by a

large water reservoir in order to maintain a constant temperature. Additionally, a thermocouple (T_S) is included in the Sieverts' area.

The hydrogen is led into the reactor via the volume flow controller (VFC). Its low flow range allows slow reaction in order to maintain almost equilibrium during PCI measurements. Because its direction of measurement is only one way, for desorption, the gas flow is redirected accordingly. Thermocouples are included in the tube area (T_{tube}) and inside the reactor (T_R). A bypass is included for instant hydrogen supply during reaction rate measurements. Additionally, thermocouples are inserted next to the VFC (T_{VFC}) and inside the thermostatic bath (T_{bath}).

The pressure on the reactor side (p_R) is measured by different pressure sensors in order to achieve precise measurements for all pressure levels (see Table 3). A filter (2 μm) is placed between reactor and test bench to protect the equipment from contamination by metal hydride powder. A vacuum pump³ (VP) is added for activation and evacuation during desorption. A thermostatic bath⁴ tempers the reactor to the desired temperature. The data is logged by a Siemens SIMATIC system in a 0.5 s interval. For the extremely long PCI experiments of up to 72 h, the data was reduced to a 5 s interval. The test bench was designed to run the dynamic pressure-concentration isotherm (PCI) measurements automatically. Hydrogen with a purity of 99.999 % was used for activation and all experiments. A picture of the test bench is given in Figure 11.

³ Vacuum pump by KNF - N 813.4 ANE

⁴ Thermostatic bath Proline RP890 by Lauda



Figure 11. Picture of the characterization test bench

All details on the measurement equipment including the measurement uncertainties are given in Table 3. The derived volumes of test bench and reactors, their measurement and calculation are described in Appendix B.

Table 3. Measurement equipment of the characterization test bench

	notation	manufacturer details	measurement range	measurement precision
pressure	p_d	Keller PD-33X	0 ... 10 bar	± 0.015 bar
	p_s	Selected according to expected pressure drop (reaction rates)		
	$p_{S,5}$	Keller PAA-21Y	0 ... 5 bar	± 0.0125 bar
	$p_{S,40}$	Keller PA-21Y	1 ... 40 bar	± 0.1 bar
	$p_{S,120}$	Keller PA-21Y	1 ... 120 bar	± 1.8 bar
	p_R	Selected according to expected pressure		
	$p_{R,5}$	Keller PAA-21Y	0 ... 5 bar	± 0.0125 bar
	$p_{R,40}$	Keller PAA-21Y	0 ... 40 bar	± 0.1 bar
	$p_{R,120}$	Keller PA-23SY	1 ... 120 bar	± 0.12 bar
	$p_{R,1}$	Pfeiffer CMR 361	0.1 ... 1100 mbar	$\pm 0.2 \% \text{ Rd}^d$
volume flow controller	VFC	Bronkhorst F-221M-PBD-33-V	0.5 ... 25 ml _N /min	$\pm (0.5 \% \text{ Rd} + 0.1 \% \text{ FS})$
temperature	$T_S, T_R, T_{tube}, T_{VFC}, T_{bath}$	thermocouples type K, class 1	-40 ... 1100 °C	± 1.5 K

^d Readout accuracy of SIMATIC system: 0.3 mbar (1100 mbar/ 27648 units = 0.0398 mbar/ unit; 50 Hz: factor 8 → 0.318 mbar)

With all these considerations, the test bench design allows the precise PCI and reaction rate measurements of a large variety of pressure and temperature levels, mass of absorbed and desorbed hydrogen as well as materials quantity.

2.3. Thermodynamics (Pressure-Concentration Isotherm)

Most metal hydrides have been characterized at elevated temperature levels, suitable to the considered applications. For the materials considered in this work, only limited information about their pressure-concentration isotherm is available in literature, in particular at low temperatures (see section 1.3.1). However, the precise values for the considered temperatures in this work are important on the one hand for the evaluation of the experiment performance in laboratory scale. On the other hand, detailed pressure-concentration isotherm data is required for the reaction rate measurements. Due to the lack of data at the low temperature range, these measurements were performed in this thesis.

This section describes the procedure and reactor in detail, explains the analysis and experimental design and finally gives the PCI results, plateau slopes and reaction enthalpies and entropies for both materials at temperature down to -30 °C.

2.3.1. Measurement procedure

The test bench is able to run PCI measurements automatically. Input parameters are the Sieverts' volume combination, the starting pressure level, the end pressure level of the reactor for absorption as well as the hydrogen mass flow and reaction time for both absorption and desorption. During absorption, the hydrogen is supplied to the reactor at the set flow rate. The pressure in the reactor increases slowly until either the set end pressure level or the end of the reaction time is reached. For desorption, the hydrogen is released from the reactor at the set flow rate for the duration of the set reaction time. The pressure can be lowered below ambient pressure by the vacuum pump.

The measurement value of interest is the pressure change in the Sieverts' volume over time and the reactor pressure. From this, the absorbed hydrogen mass can be calculated as a function of time and related to the reaction pressure. The precise pressure differential sensor used for the PCI experiments is not able to measure a pressure increase. Therefore,

the hydrogen conversion during desorption is determined by relation of the hydrogen flow rate to the absorption value (cf. Appendix B).

In order to sustain almost equilibrium, the flow rate was reduced until no further change of the pressure level of the plateau was observed. This determined maximal hydrogen flow rate in this work led to a maximal temperature change of the metal hydride of 3 K at any time.

Exemplary, Figure 12 depicts the pressure course inside the reactor, the pressure drop in the Sieverts' volume for absorption and the hydrogen flow rate for absorption and desorption of experiment # 6 (cf. Table 4). Due to the constant hydrogen flow rate, the pressure in the Sieverts' volume changes constantly over time. Only at the end of desorption, the flow rate decreases due to the decreasing pressure difference until the reaction is over. To take this into account, the flow rate is also considered for the calculation of desorbed hydrogen. The pressure course inside the reactor shows the typical course of a PCI with the distinct formation of the plateau and the clearly visible hysteresis between absorption and desorption.

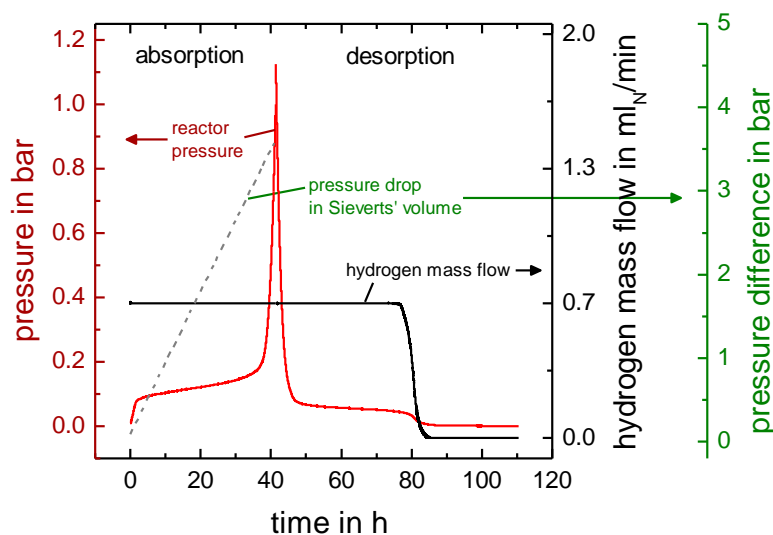


Figure 12. Exemplary measurement results for absorption and desorption (exp. #6)

2.3.2. Reactor design

For near equilibrium measurements, the reactor design has to allow sufficient heat and mass transfer in order to ensure reaction at constant temperature. Due to the small volume flow rates, an inner tube diameter of 9 mm satisfies this requirement, at the same time realizing enough sample mass to generate measurement values well above the measurement

precision. The temperature change inside the reactor was measured by a thermocouple type K at the center of the tube, approx. 1.3 cm above the lower end of the reactor. The design limited the change of temperature of the material to less than 3 K at all times for all measurements. The used reactor is shown in Figure 13. The stainless steel tube ($d_{\text{out}} = 12 \text{ mm}$) had a length of approx. 100 mm. A hand valve protects the material at installation. A filter with a pore size of $0.5 \mu\text{m}$ was added to prevent the material from moving. A sample mass of 10.63 g of $\text{LaNi}_{4.85}\text{Al}_{0.15}$ and 6.20 g of C5 have been used.

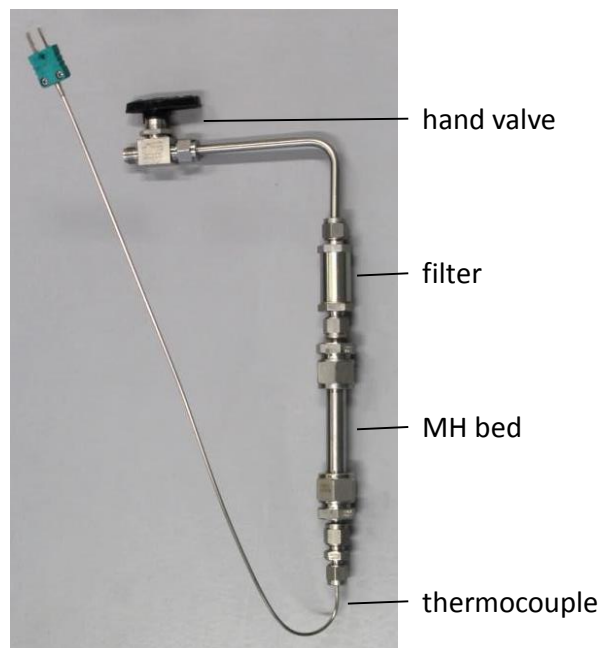


Figure 13. Reactor for dynamic pressure concentration-isotherm measurements

2.3.3. Analysis

For absorption, the hydrogen conversion is calculated from the pressure change in the Sieverts' volume, taking the temporal change of the temperatures in all volumes into account. The desorbed hydrogen mass is calculated using the volume flow value. The calculated results led to lower values than for absorption. This is a commonly seen result in PCI measurements. However, the material had to desorb the same amount as was absorbed, because during the next absorption process, the same hydrogen conversion value was reached (without additional desorption). Additionally, the balance via Sieverts' method during absorption leads to more accurate values than via the flow rate meter during desorption. Therefore, the hydrogen conversion during desorption is normalized by fitting the overall released hydrogen to the value for the absorption. The ideal gas law was used, because the compressibility factor of hydrogen at the considered temperatures and

pressures of below 1.03 [101] is negligible. Details on the calculations are given in Appendix B.

Only the plateau of the PCI is of importance when considering equilibrium properties, because here, the vast majority of hydrogen is converted and the pressure only changes slightly with conversion. The plateau slope for each PCI curve was determined by using equation (4). The equilibrium states for each temperature and both absorption and desorption was determined from the PCI curves. The temperature dependent van't Hoff equation (5) can be fitted to these values resulting in values for the reaction enthalpy and entropy.

2.3.4. Experimental design

LaNi_{4.85}Al_{0.15} is used as heat-generating material between -20 and 20 °C. During regeneration, the material was heated to the temperature level of the considered waste heat between 90 and 130 °C. Therefore, this material is characterized in the whole temperature range between -20 and 130 °C.

C5 is considered as hydrogen-supplying material for the coupled reactions. It is tempered to the considered ambient temperature between -20 and 20 °C. Since desorption leads to temperature decrease, this material is characterized down to -30 °C. Additionally, a PCI was measured at 35 °C.

In order to ensure reaction close to equilibrium, different hydrogen flow rates have been tested at the lowest and, for LaNi_{4.85}Al_{0.15}, additionally at an intermediate temperature, and used for the experiments at higher temperatures. The experiments were performed in a mixed order and some were repeated to minimize systematic errors.

Table 4 and Table 5 give a summary of all performed experiments, including the experiment number indicating the order of conduction, the temperature, used pressure sensor (cf. Table 3), volume flow and the maximal time allowed for reaction. The bold experiment numbers refer to the measurements used for the final PCI curves.

For almost all experiments, the Sieverts' volume V_{S2} with 492.49 ml was used. Only for the measurement of LaNi_{4.85}Al_{0.15} at 130 °C, the volume V_{S1} was used additionally (total Sieverts' volume of 783.89 ml).

Table 4. Experimental design for PCI measurements of $\text{LaNi}_{4.85}\text{Al}_{0.15}$

$\text{LaNi}_{4.85}\text{Al}_{0.15}$				
No. of exp.	T in °C	p-sensor	\dot{V} in ml _N /min	time allowed for reaction in h (abs/des)
6	-20	$p_{R,1}$	0.65	48/69
5			1.3	24/27
7	0		0.65	48/69
11	20	$p_{R,5}$	0.65	72/72
1			2.6	12/12
4	40		1.3	24/24
2			2.2	14/14
3				12/12
8	110	$p_{R,40}$	0.65	52/60
9			1.3	48/48
10	130		1.3	44/78

Since the reaction rate accelerates with increasing temperature, the obtained flow rate is valid for all higher temperatures. At the lowest temperature for the $\text{LaNi}_{4.85}\text{Al}_{0.15}$ experiments, a flow rate of 0.65 ml_N/min showed slightly lower equilibrium pressures than the higher flow rate of 1.3 ml_N/min and hence was used for higher temperatures as well. Due to the wide considered temperature range, this procedure was repeated at 40 °C resulting in a higher sufficient flow rate of 1.3 ml_N/min and hence shorter measurement time.

Experiment # 3 is a repetition of experiment # 2, however, the allowed time for reaction prevented full conversion. Nonetheless, this experiment can show the well repeatability of the experimental set-up. Experiment # 8 is excluded from further consideration due to decreased heat transfer during the experiment caused by an insufficient level of the heat transfer fluid in the thermostatic bath. At the very beginning of experiment # 11, a disturbance of the thermostatic bath occurred. Therefore, the course of the formation of the α -phase was shifted to higher hydrogen conversions. However, the comparison to

Table 5. Experimental design for PCI measurements of C5

C5				
No. of exp.	T in °C	p-sensor	\dot{V} in ml _N /min	time allowed for reaction in h (abs/des)
2	-30	$p_{R,5}$	0.5	96/73
1			0.65	48/62
3	-20		0.65	62/48
5	20	$p_{R,40}$	0.65	72/72
4	35		0.65	94/156

experiment # 1, although at higher hydrogen flow rates, shows almost no difference in the position of the plateau. Therefore, experiment # 1 was considered for the final PCI curve.

For the C5 measurements, in between experiment 2 and 3, two full conversion cycles at -30 and -20 °C were performed, which, however, are not considered further in this work. The maximal hydrogen flow rate was determined at -30 °C. The decrease of the flow rate to 0.5 ml_N/min did not change the position of the plateau; hence the higher flow rate of 0.65 ml_N/min was used for all temperatures.

2.3.5. Results

Since no pressure-concentration isotherms at low temperatures are available for the chosen materials LaNi_{4.85}Al_{0.15} and C5, the PCIs measured here represent the first publication at temperatures below 0 °C for both materials.

The pressure-concentration isotherms were measured dynamically at a fully automated test bench. Low mass flows realized a reaction almost at equilibrium. The hydrogen conversion was calculated using the Sieverts' method for absorption and normalized flow rate for desorption.

This section presents the results for both materials separately, discusses the maintenances of the reaction close to equilibrium for different volume flows, draws the comparison to the literature and presents both final equilibrium lines down to -20 and -30 °C, respectively, including the plateau slope and reaction enthalpies and entropies.

Thermodynamic properties of LaNi_{4.85}Al_{0.15}

Equilibrium state, isothermal conditions and repeatability

For dynamic equilibrium measurements, first of all, it has to be shown that the reaction takes place close to equilibrium. The reaction rate, depending on material kinetics, mass and heat transfer, has to be faster than the hydrogen supply rate. To check if the flow rate is small enough, its value is decreased until no change in the respond pressure can be observed. The PCIs obtained at different hydrogen flow rates at -20, 20 and 40 °C are given in Figure 14.

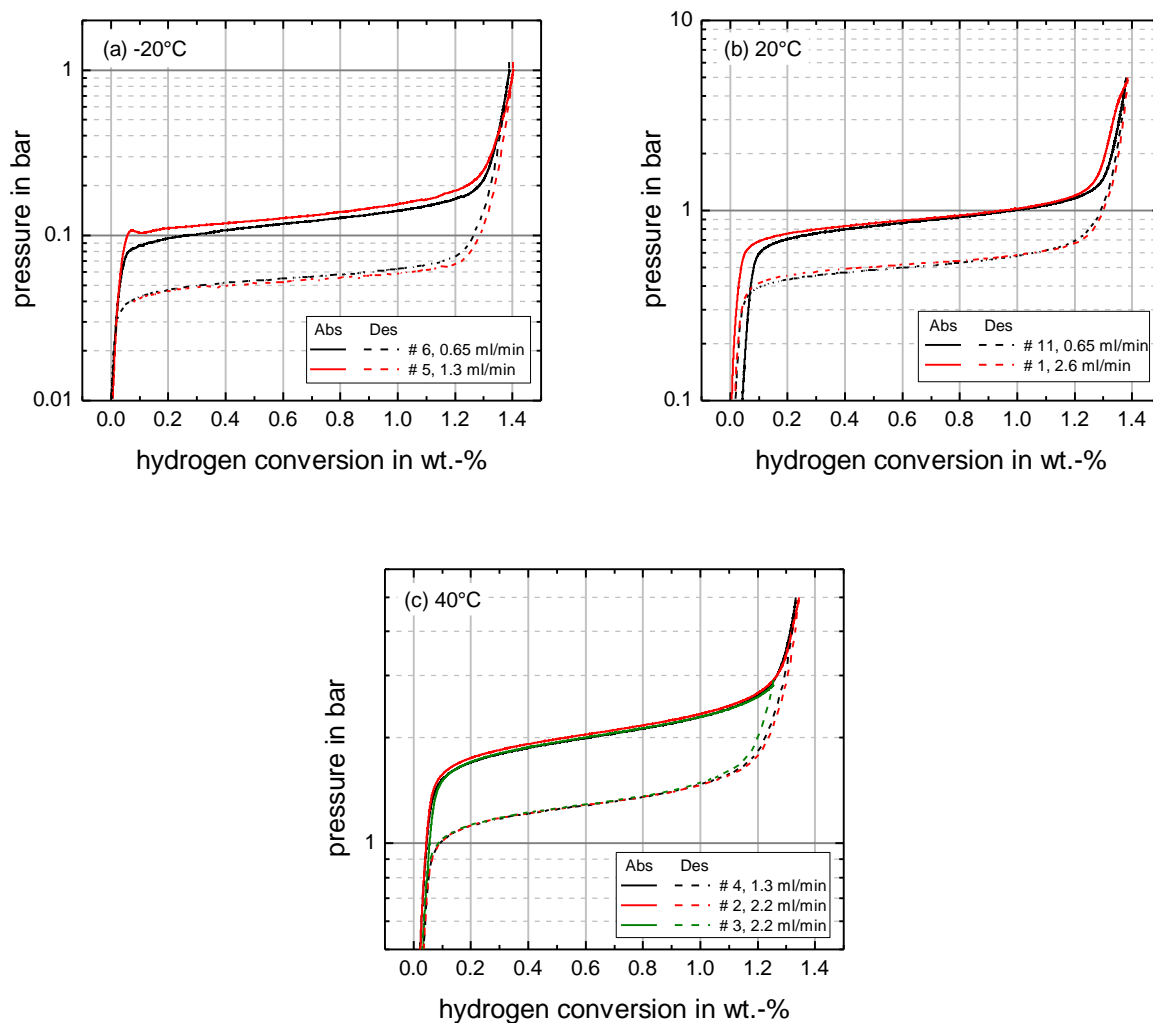


Figure 14. PCI for $\text{LaNi}_{4.85}\text{Al}_{0.15}$ at (a) -20°C , (b) 20°C and (c) 40°C at different hydrogen flow rates and repeated experiments

In order to find the appropriate flow rate for lower temperatures, the volume flow was varied at -20°C . This is shown in Figure 14 (a). Experiment #6 was performed at $0.65 \text{ ml}_N/\text{min}$ and #5 at $1.3 \text{ ml}_N/\text{min}$. Here, a difference between the lines is visible. The lower flow rate of #6 leads to a lower equilibrium pressure during absorption and a higher equilibrium pressure during desorption. This indicates, that the higher flow rate of #5 does not allow enough time to approach equilibrium. Therefore, the lower flow rate of $0.65 \text{ ml}_N/\text{min}$ was chosen for the measurements at low temperatures.

During experiment #11 at 20°C , a disturbance of the thermostatic bath occurred at the very beginning. This led to a shift of the course of the formation of the α -phase to higher hydrogen conversions, as can be seen in Figure 14 (b). However, the comparison to

experiment # 1, although at higher hydrogen flow rates, shows virtually no difference in the position of the plateau. Therefore, experiment # 1 was considered for the final PCI curve.

Figure 14 (c) shows the PCI measurements at 40°C for experiments # 2-4. Experiments # 2 and # 3 were performed at the same mass flow and show the excellent repeatability of the experiments. Since the absorption of # 3 was not allowed enough time for complete conversion, desorption starts at a lower value, too. Otherwise, both experiments agree exceptionally well. Experiment # 4 was performed at a lower hydrogen flow rate. The results are again very similar to the two other experiments; therefore, both flow rates are sufficient for measurements close to equilibrium. Consequently, a flow rate of 1.3 ml_N/min was chosen for the measurements at higher temperatures.

From these considerations, it can be stated that the used hydrogen flow rates allow the approach of the equilibrium state during measurement for all temperatures.

Additionally, the temperature change of the material should not exceed 3 K in order to refer the results to one temperature value. The temperature changes for all experiments are given in the Appendix B. They confirm that the temperature never changes by more than 3 K, as required, and significantly less during the $\alpha+\beta$ -phase. Hence, the acquired data can be related to the set temperature.

Comparison to literature

Two different sources are available at 110 °C, therefore, this temperature is used for comparison. The values from Selvam et. al [54] and Willers [55] are given with the according PCI of this work in Figure 15.

As can be seen there, all values show close agreement, in particular the level of the plateaus for both absorption and desorption agree well. This also confirms a comparable and reliable manufacturing method of the material. Therefore, the expansion to lower temperatures promises reliable results.

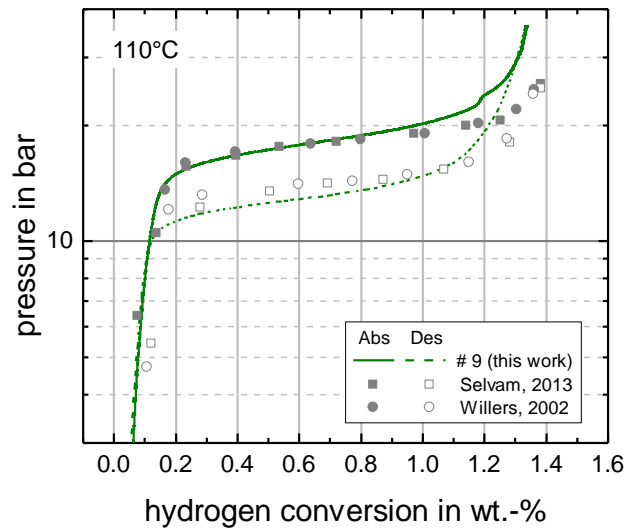


Figure 15. Comparison of results of $\text{LaNi}_{4.85}\text{Al}_{0.15}$ to literature [54]–[56]

Final PCI results

The previous discussion shows that the performed experiments approach equilibrium and can be related to the set temperature of the material. The good agreement with literature allows the extension to lower temperatures. The final PCIs for $\text{LaNi}_{4.85}\text{Al}_{0.15}$ in a temperature range from -20 to 130 °C are given in Figure 16. They represent the first publication of thermodynamic values at temperatures below 25 °C and allow precise description of the equilibrium state down to -20 °C.

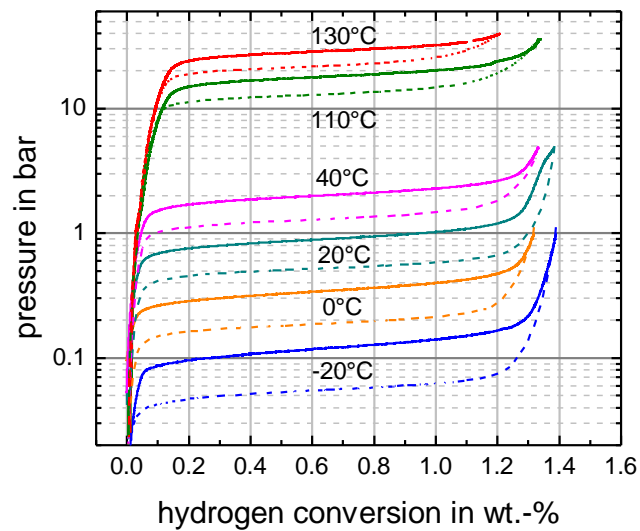


Figure 16. PCI measurements for $\text{LaNi}_{4.85}\text{Al}_{0.15}$ for all temperatures (-20 °C: #6, 0 °C: #7, 20 °C: #1, 40 °C: #4, 110 °C: #9, 130 °C: #10)

The material exhibits a very small plateau slope and small hysteresis compared to other metal hydrides.

Plateau slope and reaction enthalpy and entropy

For the reversible hydrogen conversion only the plateau region is considered. For the determination of the slope, the plateau lines were approximated with a linear regression resulting from equation (4). The mid hydrogen conversion ω_{mid} for all lines is 0.65 wt.%. All values for the resulting slope are given in Appendix B. A comparably small mean value for the plateau slope of $0.004 \text{ wt.}\%^{-1}$ was determined for both absorption and desorption.

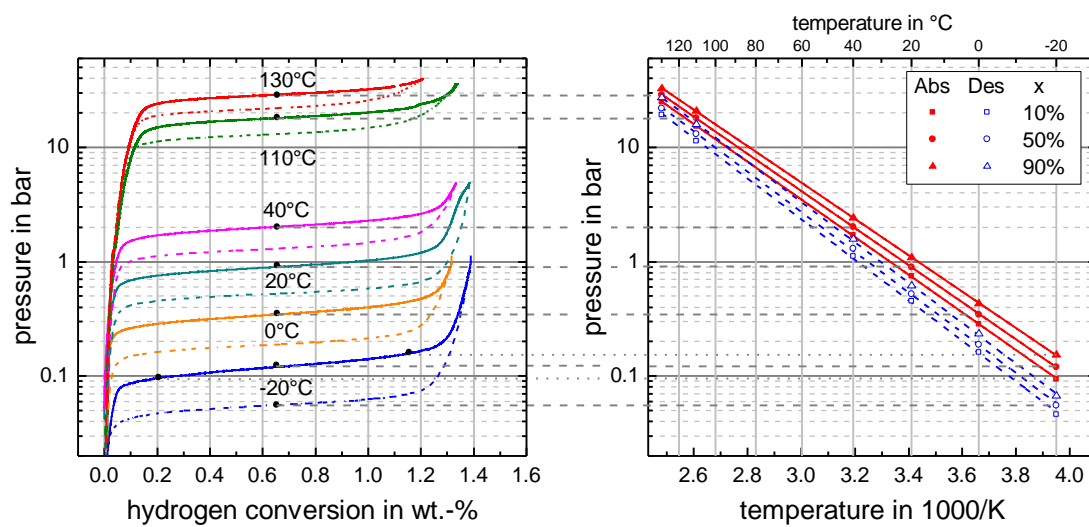


Figure 17. Van't Hoff plot from PCI measurements for $\text{LaNi}_{4.85}\text{Al}_{0.15}$ for absorption (solid) and desorption (dashed)

Equilibrium values for 10, 50 and 90 % of transformed fraction were determined and drawn in a van't Hoff plot, as shown in Figure 17. The regression given in equation (5) leads to the determination of the reaction enthalpy and entropy. All thermodynamic results regarding $\text{LaNi}_{4.85}\text{Al}_{0.15}$ are given in Table 6 and are valid for a temperature range between -20 and 130 °C.

Table 6. Reaction enthalpy, entropy and plateau slope for $\text{LaNi}_{4.85}\text{Al}_{0.15}$

	x in %	$\Delta_R H$ in kJ/mol	$\Delta_R H_{\text{mean}}$	$\Delta_R S$ in J/(mol K)	$\Delta_R S_{\text{mean}}$	m_{pl} in $\text{wt.}\%^{-1}$	ω_{mid} in wt.-%
absorption	10	31.54	31.0	105.05	104.9	0.004	0.65
	50	31.08		105.10			
	90	30.47		104.66			
desorption	10	33.98	33.8	109.08	109.9		
	50	33.70		109.41			
	90	33.76		111.27			

A comparison of the values of the enthalpy and entropy to literature shows only small deviations. The values of Selvam et. al [54] are up to 2 % higher, determined at temperatures between 50 and 110 °C. The enthalpy values of Willers [55], also derived between 50 and 110°C, are 0.6 % higher, whereas the entropy values are smaller by up to 2.7 %.

The observed discrepancies might either be due to differences in the manufacturing process or due to the larger temperature range and the extension to lower temperatures. The results allow precise description of the equilibrium state of the materials down to -20 °C and are also used for the reaction rate measurements.

Thermodynamic properties of $Ti_{0.95}Zr_{0.05}Mn_{1.46}V_{0.45}Fe_{0.09}$ (C5)

Equilibrium state, isothermal conditions and repeatability

In order to performed PCI measurements, the proximity to the thermodynamic equilibrium has to be assured at any time. This section discusses the appropriate hydrogen mass flow for almost equilibrium, the isothermal conditions for the material and the repeatability of the measurements with C5.

For the lowest temperature investigated, where the material shows the slowest reaction rate, the hydrogen mass flow was varied. The PCI curves for -30 °C for two different hydrogen flow rates are given in Figure 18. It can be seen, that the decrease from 0.65 to 0.5 ml_N/min did not affect the results. Hence, reaction close to equilibrium can be achieved with both rates. Therefore, the flow rate was set to 0.65 ml_N/min for all investigated temperatures. Additionally, the results show the extremely good repeatability of the experiments.

The temperature of the material never exceeded a change of more than 1.7 K during the measurements. A figure of all temperature changes is given in the Appendix B.

Hence, the material stayed close to equilibrium and the results can be referred to the intended temperature.

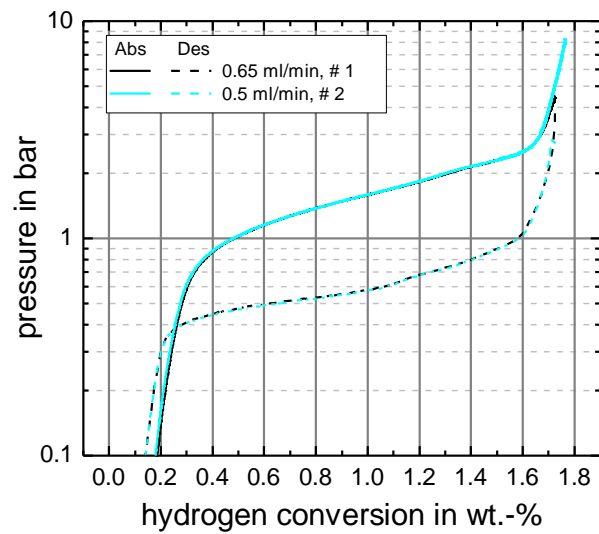


Figure 18. PCI for C5 at -30 °C at different hydrogen volume flow rates and repeated experiments (exp. #1, 2)

Comparison to literature

The results are compared to literature data. Skripnyuk and Ron [60] and Capurso et al. [58] published PCI measurements at 20 °C. The polynomial by Herbrig et. al [61] was used to calculate the values for the same temperature. This data is given in Figure 19 together with the results of this work. As can be seen, there is high correspondence between the data. Some deviations can be identified at the beginning of absorption and desorption, however, the largest variations occur between the different literature values. Therefore, the results derived in this work can also be trusted at lower temperatures.

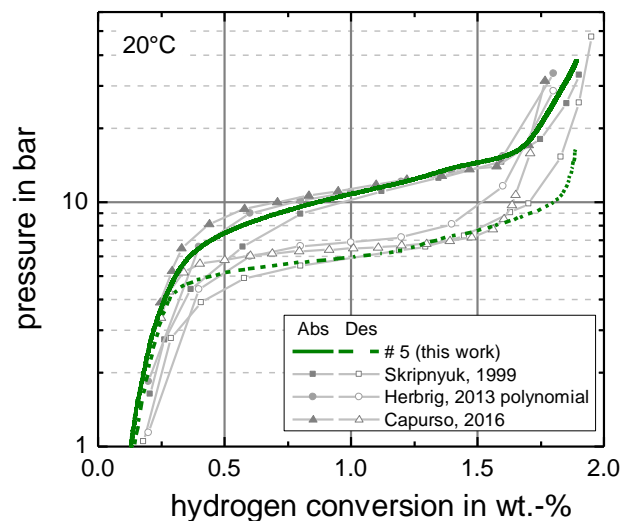


Figure 19. Comparison of results of C5 to literature [58], [60], [61]

Final PCI results

Figure 20 gives the final results of the PCI measurements for C5 between -30 and 35 °C. These results extend the available data for the first time below 0 °C and allow precise description of the thermodynamic behavior of C5 down to -30 °C.

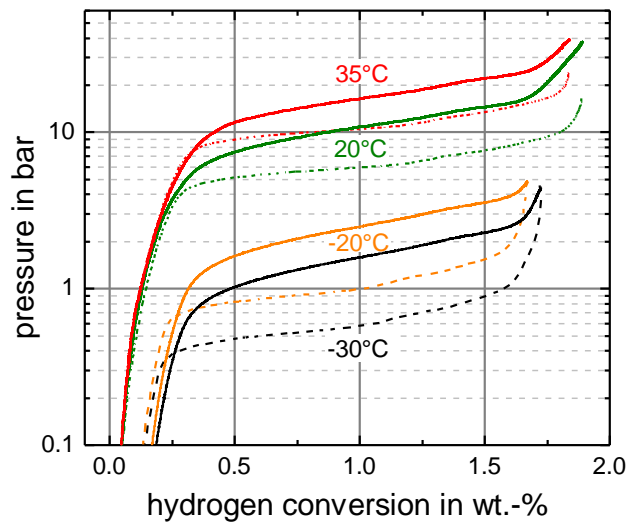


Figure 20. PCI measurements for C5 for all temperatures (-30°C: #1, -20°C: #3, 20°C: #5, 35°C: #4)

Although the experiments have been conducted with great care and possible effects of the analysis have been looked at intensively (see Appendix B), the overall hydrogen conversion shows slightly smaller values for decreased temperatures. This behavior does not coincide with reported general metal hydride properties, from which one would expect an increase of the plateau at lower temperatures. The reason for this deviation is unclear. However, the resulting pressure level of the $\alpha+\beta$ -phase is not affected but allows precise description of the mid-plateau. Hence, the curves were aligned at 50 % conversion and these values were used for further evaluation.

Plateau slope and reaction enthalpy and entropy

The middle of the PCI-plateau corresponds to a hydrogen conversion of 1 wt.-% for all temperatures. A mean plateau slope of 0.72 wt.-%⁻¹ was derived for absorption and 0.53 wt.-%⁻¹ for desorption (see all values in Appendix B). These values are considerably higher than for LaNi_{4.85}Al_{0.15}. This is typical for Hydralloy C-materials, as can also be observed in [61].

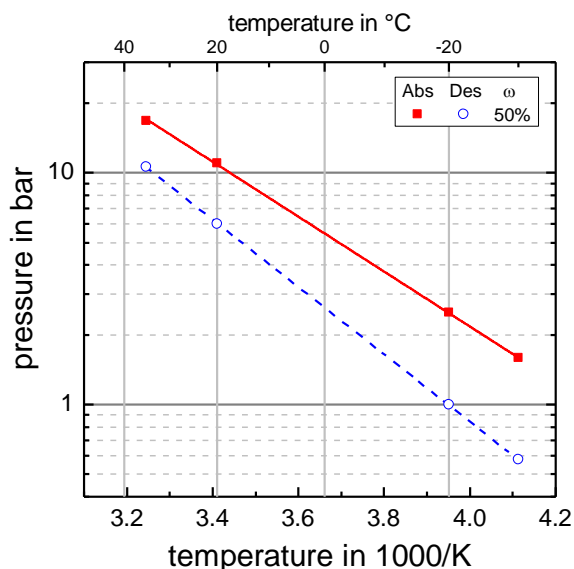


Figure 21. Van't Hoff plot from PCI measurements for C5 for absorption and desorption

The resulting van't Hoff plot for both absorption and desorption is given in Figure 21. The resulting values for the reaction enthalpy and entropy are given in Table 7, together with the plateau slope and mid-plateau value, which are valid for a temperature range between -30 and 35 °C.

The comparison of the obtained values to literature shows significantly larger discrepancies than for $\text{LaNi}_{4.85}\text{Al}_{0.15}$. Interestingly, the largest deviations were found compared to the work of Skripnyuk and Ron [60], although they considered a similar temperature range of -20 to 20 °C. Their enthalpy value is 12.8 % larger for absorption and 5.6 % for desorption. Only one value for the entropy is stated, which differs by +9.6 and -3.1 % from values of this thesis for absorption and desorption, respectively. However, since little information about the PCI measurements were provided, further assessment is difficult and the values of the presented work are hence trusted. Especially, since the comparison to other references [58], [61] show deviations of only 2.0 % or less.

Therefore, the obtained values allow precise description of the thermodynamic properties of C5 down to -30 °C.

Table 7. Reaction enthalpy, entropy and plateau slope for C5

	$\Delta_R H$ in kJ/mol	$\Delta_R S$ in J/(mol K)	m_{pl} in wt.-% ⁻¹	ω_{mid} in wt.-%
absorption	22.69	97.20	0.723	1.0
desorption	27.83	109.90	0.534	

Equilibrium states for both materials

In the previous sections, the PCI measurements for both materials were discussed and detailed results were presented. This section compares the thermodynamic properties of both materials.

The equilibrium line for both materials at 50 % transformed fraction is given in Figure 22. The results reveal the excellent fit of the selected pair to the considered boundary conditions. Some differences between the obtained thermodynamic properties and reported ones were found. The precise values of this work are particularly important for the reaction rate measurements and the analysis of the effects on the coupled reactions.

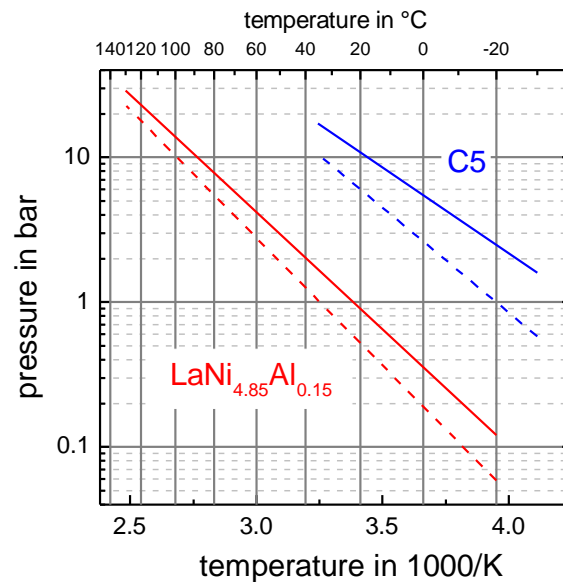


Figure 22. Van't Hoff plot for both LaNi_{4.85}Al_{0.15} (red) and C5 (blue); absorption (solid), desorption (dashed)

2.4. Reaction kinetics

High power applications in vehicles require fast reaction of the metal hydrides. However, reaction rates of thermochemical reactions decreases with decreasing temperature according to Arrhenius. Due to the reaction at very low temperatures in vehicle applications and the lack of detailed knowledge of the reaction rate coefficients in this range, these properties have to be determined for LaNi_{4.85}Al_{0.15} and are required for an appropriate reactor design. For C5, the results provided by Skripnyuk and Ron [60] are used.

In this section, the measurement is described in detail, considering the reactor design, measurement procedure and analysis and experimental design. Then, the results are presented and discussed.

2.4.1. Measurement procedure

The experiments were performed at the same test bench as the PCI measurements. For the reaction rate measurements, different pressure sensors (p_S) with maximal pressures between 5 and 40 bar were used to enable precise results (see Table 3). Hydrogen was supplied by opening the valve of the bypass to ensure instant pressure equalization. Hence, both the Sieverts' and the reactor volume are at the same pressure after equalization.

For an extensive measurement, different end pressures after full conversion were investigated. They relate to different factors f between end pressure and equilibrium pressure at the given temperature according to equation (12):

$$f = \frac{p_{end}(x_{end})}{p_{eq}(T_{MH})} \quad (12)$$

The investigated factors ranged between 2 and 57. For all factors, similar rate coefficients were obtained. Therefore, gas transport was sufficient for at all investigated pressures, which is also discussed in the result section.

The key measurement value is the pressure drop in the Sieverts' volume over time. A typical course is given in Figure 23 for experiment # II-7 (cf. 2.4.4). The steep decrease of the pressure at the very beginning is caused by the gas expansion into the free volume of the reactor after opening the valve. The fast pressure drop even at low pressures shows the excellent gas transfer in the test bench and also through the reaction bed.

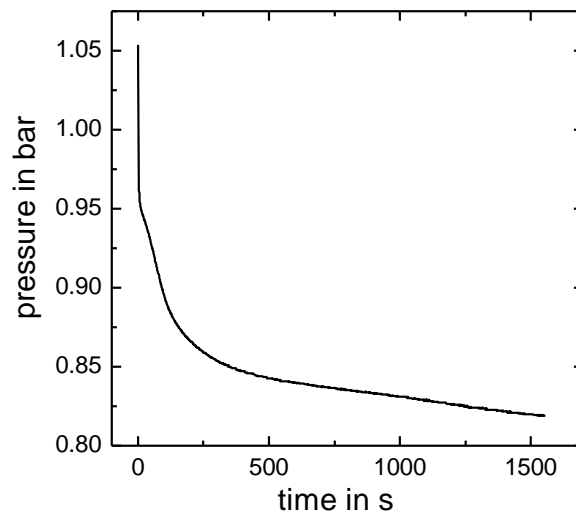


Figure 23. Pressure signal over time (exp. #II-7)

From the measured pressure and material temperature, the hydrogen conversion and the equilibrium pressure can be calculated. This allows the determination of the mechanism and pressure dependence function and hence the rate coefficient value (cf. equation (9)).

2.4.2. Reactor design

Two charges were investigated, both prepared the same way. Aluminum powder with a particle diameter below 160 μm is used as thermal ballast to disperse the heat of reaction quickly. The diameter, on the one hand, is considered to be small enough to mix well with the metal hydride of a diameter of approx. 5 μm and, on the other hand, large enough for high porosity to allow good gas transfer ability through the bed. Additionally, relatively high pressure during the experiments of up to 20 bar further enlarges the gas transport. This, however, might lead to the complete formation of the β -phase. This effect can be minimized by considering measurements only until 80 % are transformed, related to the overall conversion. Different expressions have been calculated for the experiments and the reaction of first order (cf. equation (8) in section 1.2.2) was found to fit all results.

The total sample mass of 21 g contained a metal hydride mass of 0.38 g and an aluminum mass of 20.62 g (factor of 55). The mixture was inserted into a stainless steel tube with an inner diameter of 9 mm ($d_{\text{out}} = 12$ mm). The temperature of the material was measured by a thermocouple type K at a height of approx. 1 cm from the bottom. A picture of the reactor is given in Figure 24. This design allowed a small temperature change of below 3 K for all experiments.

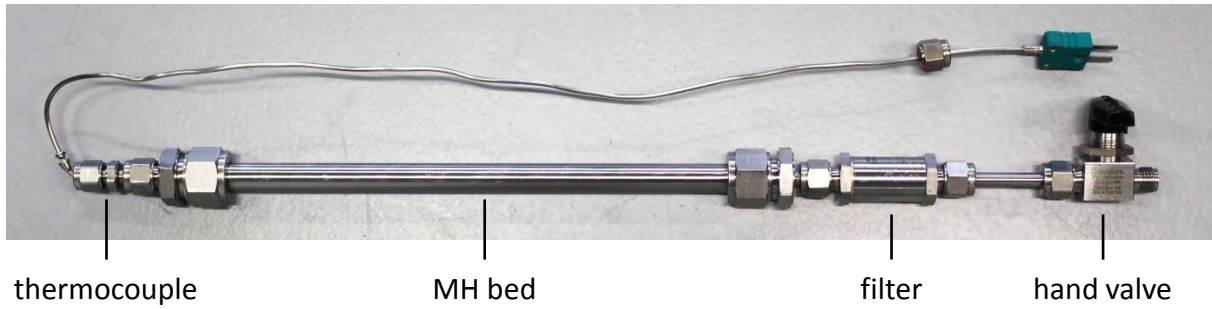


Figure 24. Reactor for reaction rate measurements

2.4.3. Analysis

The reaction rate coefficient is derived from equation (9). For that, the transformed fraction, the equilibrium pressure at material temperature and the pressure in the reactor over time are needed.

For the analysis, the following assumptions are made:

- The temperature of the Sieverts' volume is assumed to stay constant for the whole reaction time
- Due to the very short reaction time, the hydrogen supplied from the Sieverts' volume is assumed to stay at its temperature rather than adopt reactor temperature

The pressure drop due to equalization of the gas, after the valve is opened, is deduced from equation (13) considering the ideal gas law:

$$p_2 = \frac{p_{S1}V_S + p_{R1}V_R \frac{T_S}{T_R}}{V_S + V_R} \quad (13)$$

This value is considered independent of time, because of the marginal changes of the Sieverts' and reactor temperature. The difference between this value and the actually measured one leads to the pressure drop caused by absorption (14):

$$\Delta p_{abs}(t) = p_2 - p_{measure}(t) \quad (14)$$

The absorbed hydrogen mass is calculated from the ideal gas law according to equation (15).

$$\Delta m_{abs}(t) = \frac{\Delta p_{abs}(t) \cdot (V_S + V_R) \cdot M}{R T_S(t)} \quad (15)$$

From this, the hydrogen conversion and the transformed fraction can be derived according to equations (2) and (3). As discussed above, the resulting values are used between 0 and 80 % of transformed fraction.

Based on these results, the antiderivative of the mechanism equation (9) can be calculated [24]. The equilibrium pressure is calculated at the set temperature of the material according to the determined mean thermodynamic characteristics given in Table 6. Since the plateau slope of $\text{LaNi}_{4.85}\text{Al}_{0.15}$ is very small, it is neglected in this calculation. In combination with the measured pressure during the experiment, the pressure dependence function can be derived. If the plot of the coefficient of mechanism and pressure dependence function over time shows a straight line, the correct equations were applied. This is shown in the result section. The slope of this plot yields the rate coefficient, derived by fitting equation (9) to the measurement data.

2.4.4. Experimental design

The experiments were performed at a temperature of -20, 0, 20 and 40 °C. A total of 12 experiments were performed and details are given in Table 8.

The two charges investigated are indicated as I and II. Experiments at the same conditions serve to evaluate the agreement of the different charges (e.g. I-1 and II-7) and the independency of the order of experiments (II-1 and II-5). Experiments with the same end pressures (e.g. II-2, II-4 and II-8) at different temperature were performed in order to either see or exclude their influence. Experiment I-2 yielded unreasonable results and is therefore excluded from further discussion.

Table 8. Experimental design of reaction rate measurements of $\text{LaNi}_{4.85}\text{Al}_{0.15}$

No. of exp.	T in °C	p-sensor	p _{end} in bar	factor f
I-4	-20	$p_{R,5}$	0.24	2
I-1			0.8	7
II-7			1.5	13
I-3			4.2	35
II-1			3.5	10
II-5			20	57
II-6	0	$p_{R,40}$	20	57
I-2	20	$p_{R,5}$	4.2	5
II-3			20	22
II-4			20	22
II-8	40	$p_{R,40}$	20	10

2.4.5. Results

The kinetic data is essential for interpretation of larger scale reactions and for identification of the main influencing factors. Since there is no reliable data available for $\text{LaNi}_{4.85}\text{Al}_{0.15}$, the rate coefficient was determined here.

The pivotal aspect for reaction rate measurements is to enable an isothermal reaction not limited by heat or gas transfer. Therefore, excellent heat transfer is ensured by sufficient thermal ballast, which absorbs the heat of reaction at almost constant temperature.

Isothermal conditions, repeatability and correctness of mechanism and pressure dependency description

The temperature change inside the reactor for all experiments is given in Figure 25 for charge I on the left and charge II on the right hand side. As can be seen here, the temperature increase is always below 3 K, as intended.

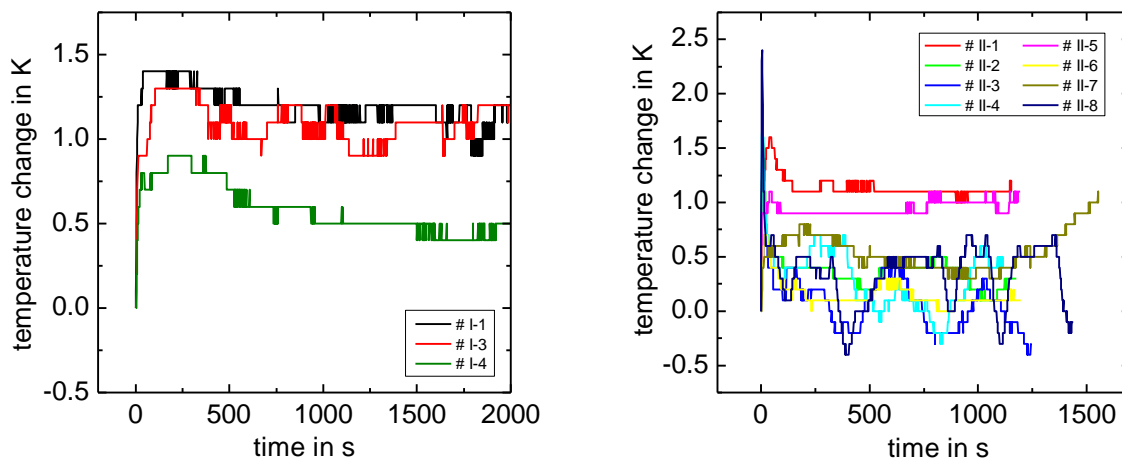


Figure 25. Temperature change in reactor for all experiments of the reaction rate measurements for charge I (left) and II (right)

A total of 12 experiments were performed in a temperature range of -20 to 40 °C. Their remarkable repeatability is depicted in Figure 26 for experiment II-1 and II-5. The pressure drop given on the left hand side agrees exceptionally. A small difference in the course of the transformed fraction and obtained coefficient of mechanism and pressure function can be seen. However, the resulting rate coefficients differ only marginal (0.00143 and 0.00122 1/s). Hence, the experiments show well repeatability.

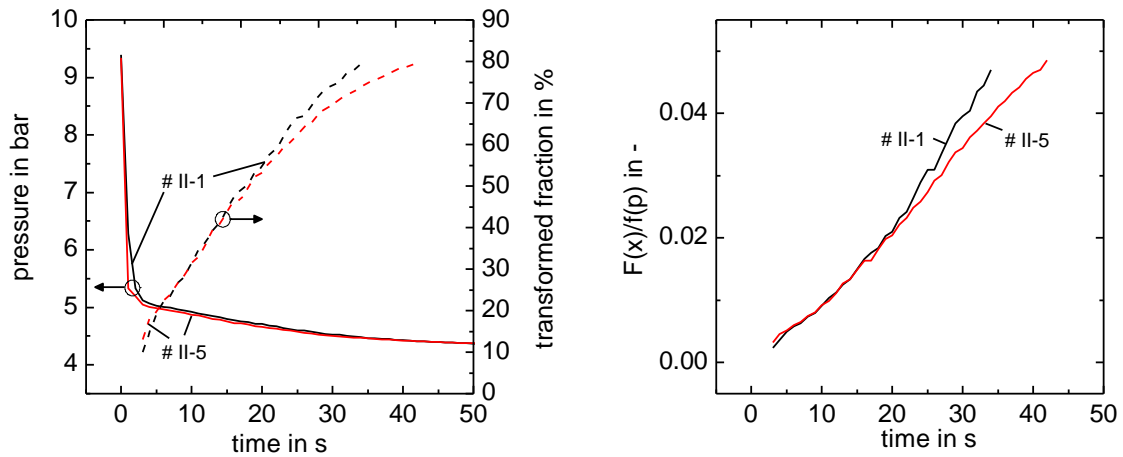


Figure 26. Repeatability of experiments (exp. #II-1 and II-5); pressure drop and transformed fraction (left) and obtained coefficient of mechanism and pressure function (right)

For all experiments, the coefficient of the antiderivative of the mechanism term and the pressure dependence function showed a reasonable straight course; hence the correct equations were used. These lines were fitted for a transformed fraction up to 80 % and the rate coefficient was derived according to equation (9). An example curve is illustrated in Figure 27 for experiment # II-7. Here, the coefficient of determination R^2 is 97.1 %. This is the smallest value for all experiments, showing the good agreement of the measurements to the used mechanism and pressure function. The rate coefficient for this experiment is $8.11 \cdot 10^{-4} \text{ 1/s}$.

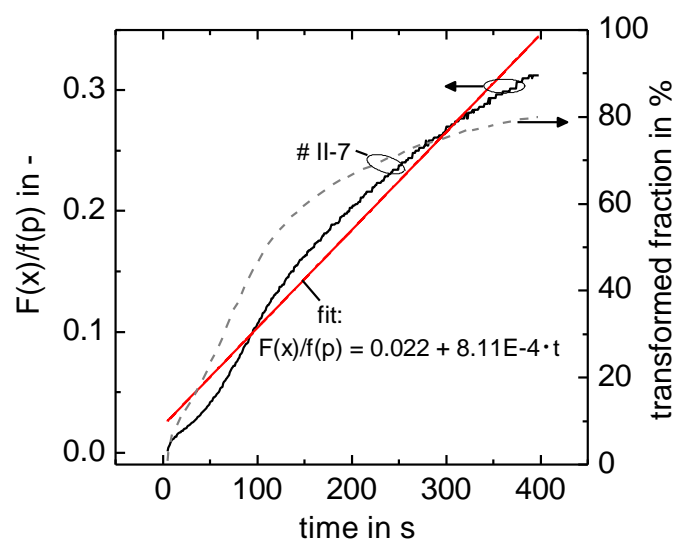


Figure 27. Coefficient of mechanism and pressure function, including fit function and transformed fraction (exp. #II-7)

Rate coefficient for $\text{LaNi}_{4.85}\text{Al}_{0.15}$

The derived rate coefficients for all experiments are given in Figure 28 together with the values for C5 from [60]. The values derived at the same temperature agree excellent. This emphasizes the good mass transfer within the bed at all investigated pressures; hence the reaction is never limited by gas transport. The apparent spread of the coefficients at low temperatures is due to the logarithmical representation of the results. The explicit values are also given in Table 9.

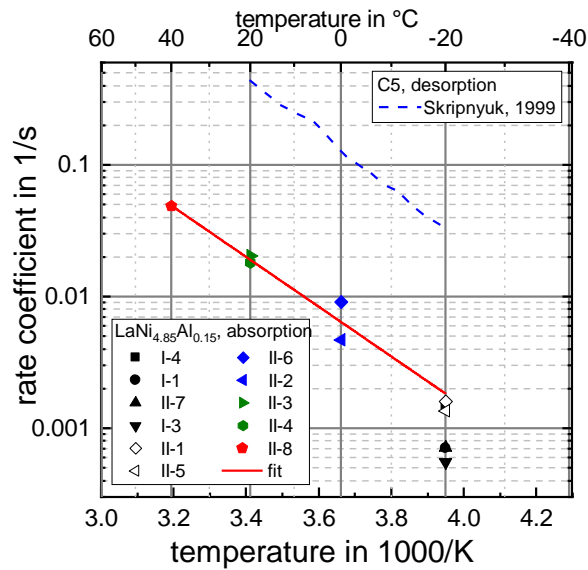


Figure 28. Rate coefficients for $\text{LaNi}_{4.85}\text{Al}_{0.15}$ for all performed experiments and for C5 [60]

The determined regression according to equation (10), given as red line in Figure 28, has a coefficient of determination of 99.1 %. From this, the pre-exponential factor and the activation energy can be determined to $A = 53,726 \text{ s}^{-1}$ and $E_a = 36,202 \frac{\text{J}}{\text{mol}}$. The resulting Arrhenius term is as follows (16):

$$k(T) = 5.4 \cdot 10^4 \frac{1}{\text{s}} \cdot \exp\left(\frac{-36.2 \frac{\text{kJ}}{\text{mol}}}{RT}\right) \quad (16)$$

As discussed in section 1.3.1, only two publications exist on kinetic determination of $\text{LaNi}_{4.85}\text{Al}_{0.15}$, which, however, only state measurements without detailed information about isothermal conditions or discussion of unexpected results. With the careful considerations of reaction limitations, isothermal conditions and experimental design, this work presents the first values down to $-20 \text{ }^\circ\text{C}$.

Table 9. Results of all reaction rate experiments

No. of exp.	T in °C	p_{end} in bar	factor f	k in 1/s
I-4	-20	0.24	2	0.00148
I-1		0.8	7	7.08861E-4
II-7				7.16806E-4
I-3		1.5	13	5.56077E-4
II-1		4.2	35	0.00159
II-5				0.00136
II-6	0	3.5	10	0.00911
II-2		20	57	0.00469
II-3	20	4.2	5	0.02057
II-4		20	22	0.01828
II-8	40	20	10	0.04887

Effect of aluminum substitution

The effect of the substitution of nickel by aluminum on the reaction kinetics is discussed controversy in literature. Therefore, the obtained rate coefficient values for $\text{LaNi}_{4.85}\text{Al}_{0.15}$ are compared to the ones for LaNi_5 from literature in Figure 29 in order to contribute to this debate. As can be seen, the slope of the line for $\text{LaNi}_{4.85}\text{Al}_{0.15}$ is similar to the literature values for LaNi_5 , however, at a considerably higher level. Hence, it can be stated, at least for the investigated derivative, that aluminum contributes to increased reaction kinetics.

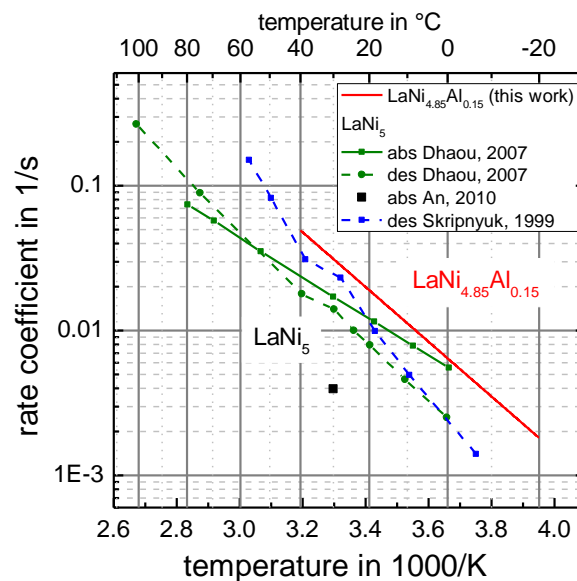


Figure 29. Rate coefficient for $\text{LaNi}_{4.85}\text{Al}_{0.15}$ compared to LaNi_5 [21], [56], [60]

Conclusion

The comparison of the materials in this work (Figure 28) shows, that the rate coefficient of $\text{LaNi}_{4.85}\text{Al}_{0.15}$ is lower than the one of C5, but still shows high values. This combination fits well to the intended application. $\text{LaNi}_{4.85}\text{Al}_{0.15}$ as heat-generating material will increase its temperature during discharge and hence increase its reaction rate. C5, on the other hand, as hydrogen-supplying material will cool down due to desorption and hence decrease its reaction rate.

The characteristics of the reaction rates given in Figure 28 allow in principle for a large temperature change. The highest reaction rate could be realized, if the hydrogen-providing material does not decrease its temperature. However, this requires some effort for heat transfer in the reactor of C5 in laboratory scale, e.g. by an increased portion of heat transfer area and hence passive reactor material. This decreases the temperature change in the material and hence benefits both discharge and regeneration. For this reason, a large ratio of reactor to metal hydride mass of up to 3.5 was allowed for the reactor design in this work. The results of the laboratory scale experiments in the following chapter will show the performance of the reactor design and the influencing factors on the specific thermal power and lead to suggestions for further improvements of the design.

3. Experiments in laboratory scale

Thermal power obtained in larger scale in previous studies did not satisfy requirements for automotive applications and no systematic investigation of its influencing factors has been provided. This work intends to expand the range of specific thermal power reached with metal hydrides by using an optimized reactor design for high power and to perform a systematic investigation of different influencing factors.

This chapter provides all details on the experiments in laboratory scale. Around 1 kg of the heat-generating metal hydride storing around 150 kJ was investigated in a high thermal power reactor. The same design was used for the hydrogen-providing material. In order to be able to identify the influencing factors separately, experiments with each reactor in a single reaction were performed first. Then, the coupled reactions were investigated in detail.

3.1. Methodology

For the laboratory scale investigation in this work with sample masses of 960 g for $\text{LaNi}_{4.85}\text{Al}_{0.15}$ and 615 g for C5, large scale effects such as mass and heat transport limitations can be assumed. Therefore, the considered scale allows deductions of the potential for the application in vehicles.

In order to investigate the achievable specific thermal power at automotive boundary conditions, a test bench and a reactor design was developed. The focus was set on the design of high thermal power. Two identical reactors were filled with $\text{LaNi}_{4.85}\text{Al}_{0.15}$ and C5, respectively, and investigated at the test bench which can provide the relevant boundary conditions. The experiments were carefully designed to exclude influences other than the investigated factors. The reactors, the test bench and experimental design are explained in detail in the following.

Even though the system design is inspired by general vehicle applications to investigate the potential under relevant boundary conditions, it does not claim to be a mature component considering all aspects for vehicle integration. However, the results are still close to the real boundary conditions and therefore allow predictions of the potential.

3.1.1. Reactor design

The reactor design focuses on high thermal power. However, the material properties pose significant challenges. Metal hydride powders have low thermal conductivity in the order of $1 \text{ W}/(\text{mK})$ [94]. Either the effective thermal conductivity of the bed can be increased, e.g. by mixing with graphite and compressing the bed [95], [96]. Or the distance from the origin of reaction to the heat transfer area must be short for fast heat exchange. However, small bed widths require large surface areas and hence increase the weight of the reactor. Moreover, in order to realize fast reaction rates, the hydrogen gas transport through the powder bed must not be limiting. All these aspects have to be accounted for by the design of the reactor.

The intention was to design a modular system as illustrated in Figure 30, based on a tube bundle heat exchanger, which satisfies the requirements mentioned above. A gap at the top allows free axial gas flow. Due to the small reactor diameter and large heat transfer area, the heat and gas transport are assumed to be independent of the radius of the reactor. Then, by conducting heat to the heat transfer fluid, a reaction front establishes moving in axial direction. Such a design allows increasing either the duration of discharge at the same maximal thermal power by axial extension. Or, the maximal thermal power value can be increased for the same duration by radial extension, however, without decreasing gas penetration. In practice, this could be realized by using several reactors either in serial or parallel sequence for extended duration or peak value, respectively. Therefore, the obtained peak value is the main performance indicator for the preheater.

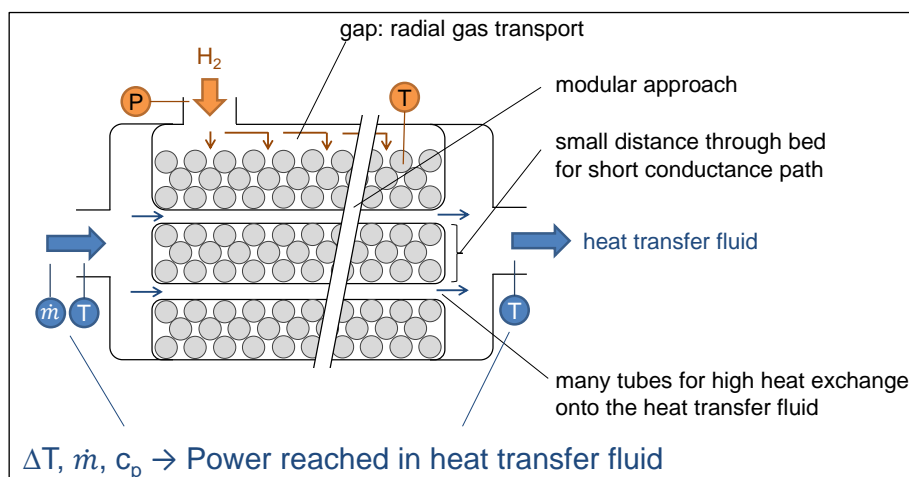


Figure 30. Modular reactor design for laboratory scale

As discussed in the kinetic section, a large passive thermal mass of the reactor of the hydrogen-providing material is used in order to realize small temperature changes. The heat-

generating material is supposed to increase its temperature in order to provide thermal energy at an elevated temperature level. This could be realized with the chosen materials due to their different hydrogen conversion capacities ($\omega_{\text{LaNi}_{4.85}\text{Al}_{0.15}} \approx 1 \text{ wt.-%}$ and $\omega_{\text{C5}} \approx 1.5 \text{ wt.-%}$). For the same amount of hydrogen, about 50 % more $\text{LaNi}_{4.85}\text{Al}_{0.15}$ is required. Stored in the same reactor, this leads to a smaller ratio of reactor to metal hydride mass for the heat-generating material ($r_{\text{LaNi}_{4.85}\text{Al}_{0.15}} = 2.2$, $r_{\text{C5}} = 3.4$)⁵. The given experimental values include all thermal losses due to the thermal mass and temperature change of the materials, reactors and heat transfer fluid (HTF).

The micro tube bundle heat exchanger used in this work is given in Figure 31. Metal hydride powder is located on the shell side, the HTF flows through the tubes. In order to ensure well axial gas transport, a gap at the top of the horizontal reactors is ensured (clipped baffle plates).

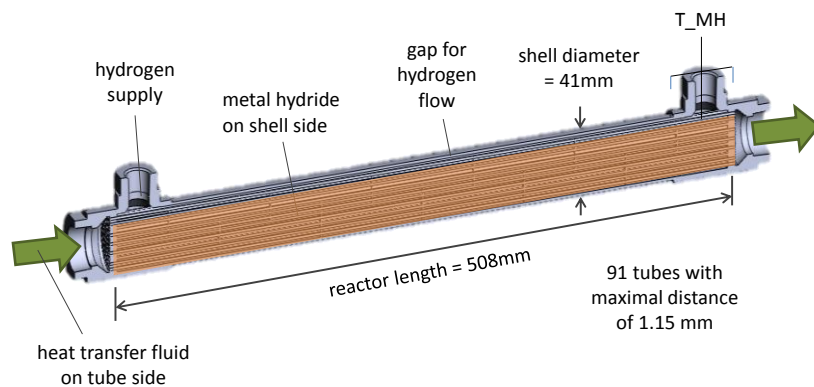


Figure 31. Laboratory scale reactor in detail

Commercially available heat exchangers by Exergy Heat Transfer Solutions (Model # 00256-06 with clipped baffles) are used to realize a high thermal power. They consist of 91 tubes with an outer diameter of 2.4 mm and 508 mm of length, a total diameter of 41 mm and a maximal distance to the tubes between 0.6 and of 1.15 mm (cf. Figure 32). The reactor mass is 2.09 kg. The reactors were filled with the corresponding amount of material so both can store about the same amount of hydrogen. Reactor 1 contains 960 g of $\text{LaNi}_{4.85}\text{Al}_{0.15}$ and reactor 2 contains 615 g Hydralloy C5.

⁵ $m_{\text{LaNi}_{4.85}\text{Al}_{0.15}} = 960 \text{ g}$, $m_{\text{C5}} = 615 \text{ g}$, $m_{\text{reactor}} = 2090 \text{ g}$

The temperatures of the HTF are measured at the inlet and outlet of each reactor and the mass flows are measured behind the reactors. Details on all measurement equipment are given in Table 10. To account for the lower accuracy of the HTF mass flow of reactor 2, the value is smoothed by the Savitzky-Golay method in a 10 point interval [102].

The sophisticated design of the commercial heat exchanger allows temperature measurement only at one position. The material temperature was hence measured by a thermocouple Type K at the end of the reactor through the sealed outlet of the shell side. Unfortunately, the thermocouple inside reactor 1 failed, hence, only the temperature of C5 can be used. This temperature information at one spot of the whole reactor of course only represents the local temperature. However, it can be used for approximation of the overall reaction.

The pressure and hydrogen flow are measured in between the reactors or in front of each reactor for the single reactions. The HTF is tempered by two thermostatic baths⁶. The measurement values are recorded in a 1 s interval. Hydrogen with a purity of 99.999 % was used for activation and all experiments.

Table 10. Measurement equipment of laboratory scale test bench

	notation	manufacturer details	measurement range	measurement precision
pressure	p_s	Keller PAA-21Y	0 ... 40 bar	± 0.1 bar
temperature	$T_{HTF1,in}^e$, $T_{HTF1,out}^e$, $T_{HTF2,in}^e$, $T_{HTF2,out}^e$	Pt100 (DIN EN 60751), class A	-100 ... 450 °C	± (0.15 + 0.0020 t ^f)
	T_{MH1}^g , T_{MH2}	thermocouples type K, class 1	-40 ... 1100 °C	± 1.5 K
mass flow meter of HTF	MFM_1	Endress & Hauser Coriolis Promass 83F	set to 0...1000 kg/h	± 0.10 % Rd
	MFM_2	Endress & Hauser Coriolis Promass 80F		± 0.15 % Rd
volume flow meter of H₂	VFM_{H_2}	Bronkhorst F-112AC- M10-AGD-33-V	0-100 l _N /min extendable to 130 l _N /min	± (0.5 % Rd + 0.1 % FS)

^e Calibrated at test bench in considered temperature range, see Appendix C

^f Modulus measurement value

^g Not used for results due to measurement error

⁶ Thermostatic baths FP 51 by Julabo and Proline RP890 by Lauda

The used heat transfer fluid is SilOil M40.165/220.10 by Huber Kältemaschinenbau AG (Germany). Its thermal capacity $c_{p,HTF}$ in J/(gK) was measured at our institute with the differential scanning calorimetry method and is calculated for the mean temperature in °C at every time step (equation (17)). The accuracy of the measurement is $\pm 10\%$.

$$c_{p,HTF} = 0.0013 T + 1.6718 \quad (17)$$

The key value is the specific thermal power actually transferred to the heat transfer fluid. This is calculated by the temperature difference of the HTF at the inlet ($T_{HTF,in}$) and outlet ($T_{HTF,out}$) of the reactors, the mass flow (\dot{m}_{HTF}) and the thermal capacity of the HTF ($c_{p,HTF}$). The specific thermal power in kW/kg is calculated according to the following equation:

$$P_{HTF} = \frac{\dot{m}_{HTF} c_{p,HTF} (T_{HTF,out} - T_{HTF,in})}{m_{MH}} \quad (18)$$

This calculation already considers all losses to ambient and due to heat conduction from the spot of reaction to the HTF.

The overall thermal energy in kJ released to the HTF is calculated by integrating the specific thermal power over time as given in equation (19).

$$Q = \int_{t=0}^t P \cdot m_{MH} dt \quad (19)$$

With the reaction enthalpy, the converted hydrogen mass in g can be calculated by equation (20).

$$m_{H_2,HTF} = Q \cdot M / \Delta_R H \quad (20)$$

With the mass of metal hydride, the hydrogen conversion can be calculated according to equation (2).

An uncertainty analysis was performed for the measurement results. The probable error for both the specific thermal power and the hydrogen conversion was about $\pm 11\%$ for all experiments. Details on the calculation are provided in Appendix C. For clearer illustration, the uncertainty is only indicated where appropriate in the result section and only close to the end of the experiment.

An experiment consists of two half-cycles: regeneration and heat generation. For regeneration, the thermostat tempering reactor 1 is set to the given regeneration temperature. The regeneration temperature of the single $\text{LaNi}_{4.85}\text{Al}_{0.15}$ experiment was set to 130 °C in analogy to the investigated experiment of the coupled reactions for better comparison. While the regeneration pressure of the coupled reactions is set by keeping reactor 2 to ambient temperature, reactor 1 in the open system desorbs against ambient pressure. As soon as all temperatures are at steady-state, the valve either to reactor 2 (coupled reactions) or to the ambient pressure (single reaction) is opened. The regeneration is over as soon as the pressure value is at steady-state. Then the valve is closed and reactor 1 is also tempered to ambient temperature. The heat generation experiment can start when all temperatures are at the simulated ambient temperature (e.g. -20 °C) in steady-state. The valve is opened to either reactor 2 (coupled reactions) or the hydrogen gas cylinder via a mechanical pressure regulator (single reaction).

An example course of the measurement values and the resulting thermal power is given in Figure 34 for experiment # 1 (see Table 11 for conditions). In all experiments, the valve was opened at time zero.

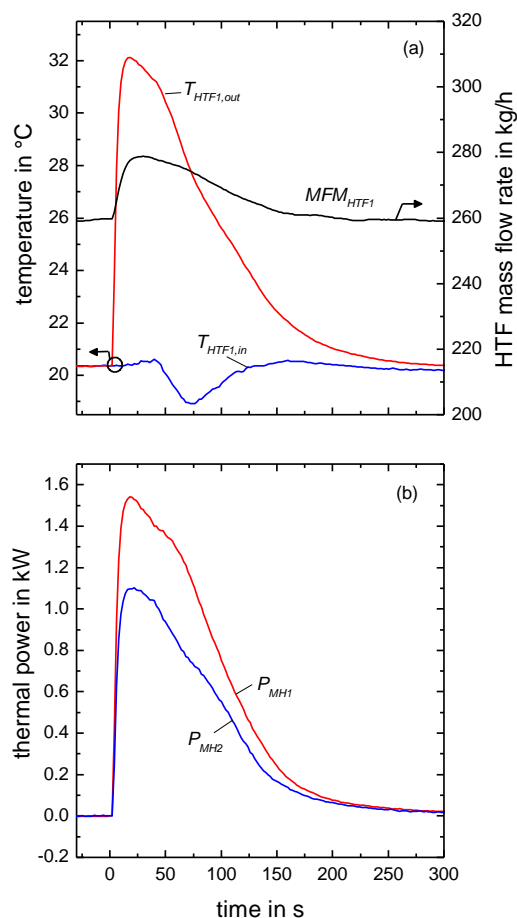


Figure 34. (a) Measurement data of reactor 1 and (b) calculated thermal power of reactor 1 and 2 (exp. #1)

Due to the high thermal power led into the HTF by reactor 1, the thermostatic bath started cooling at full power, leading to a small decrease in the inlet temperature. Nonetheless, a large temperature increase of the HTF could be sustained by the reaction, as can be seen from its outlet temperature. Also, the HTF pump is affected by the temperature increase, leading to slightly higher flow rates of less than 8 %. This is accounted for in the analysis, where the mass flow and the HTF temperatures are considered at any time step for the calculation.

The resulting thermal power is given in absolute values here (Figure 34, (b)). The heat generation (P_{MH1}) reaches higher values than the cold generation (P_{MH2}), due to the higher reaction enthalpy of $\text{LaNi}_{4.85}\text{Al}_{0.15}$ ($\Delta_R H_{\text{LaNi}_{4.85}\text{Al}_{0.15}, \text{abs}} = 31.0 \text{ kJ/mol}$; $\Delta_R H_{\text{C5, des}} = 27.8 \text{ kJ/mol}$).

From this consideration it is concluded that the values acquired at the described test bench yield precise results of the thermal power.

3.1.3. Experimental design

The experiments were designed carefully in order to exclude effects on the results by their order or any changes in the material.

During the measurement, the temperature of the materials and hence their equilibrium pressure change. Therefore, always both the temperature and pressure condition change during the experiment. In order to investigate each influencing factor separately, experiments of the single reaction were performed at similar conditions.

For the coupled reactions, the influence of the heat exchange of the reactor was investigated by variation of the HTF mass flow, and the influence of the regeneration and the ambient temperature was examined. For the single reaction of $\text{LaNi}_{4.85}\text{Al}_{0.15}$, also the HTF mass flow and ambient temperature was considered. Additionally, the driving pressure gradient was varied in order to investigate the impact of high pressures. The single C5 reaction was investigated in terms of its response to near equilibrium at $-20\text{ }^\circ\text{C}$ and the variation of the ambient temperature. The experiments were performed in a mixed order and some were repeated to minimize systematic errors.

Table 11. Experimental design of the coupled reactions in laboratory scale

Coupled reactions			
No. of exp.	T_{amb} in $^\circ\text{C}$	T_{reg} in $^\circ\text{C}$	\dot{m}_{HTF} in kg/h
8	-20	130	150
12			
15			
2		90	250
10			
16			
7	130	250	
14			
6			
4	0	110	250
13		90	
3			
5	20	130	150
1			250
11			425
9			

Table 12. Experimental design of the single reactions in laboratory scale

Single reaction			
No. of exp.	T _{amb} in °C	p in bar	m _{HTF} in kg/h
LaNi_{4.85}Al_{0.15}			
I	-20	1.5	250
VIII			
IX			
XI			
II		3	425
IV			
X			
III	0	10	250
VI		1.5	
V			
VII		3	
		20	
Ti_{0.95}Zr_{0.05}Mn_{1.46}V_{0.45}Fe_{0.09} (C5)			
XVI	-20	1	250
XVII			425
XV			230
XII	10		250
XIII			
XIV			

First, several experiments have been performed to test the bench, measurement equipment and experimental procedure (not shown here). Afterwards, the coupled reactions were investigated (Arabic numerals, Table 11), followed by the single reactions (Roman numerals, Table 12). In between the coupled and single reactions shown, additional experiments on cold generation for both coupled and single reaction of C5 were performed, which are not shown in this work. The regeneration conditions for the single reactions were 130 °C and 1 bar for LaNi_{4.85}Al_{0.15} and the respective ambient temperature for the discharge experiment and 30 bar for C5.

Experiment # VIII for the single reaction of LaNi_{4.85}Al_{0.15} yielded unreasonable results and is therefore excluded from further discussion. The experimental time of run # XIII was too short to allow full conversion and is therefore also not considered further.

3.1.4. Repeatability

Several experiments were repeated several times throughout the experimental period in order to exclude errors in the measurement itself or changes inside the material over time. The results in terms of pressure course, specific thermal power and hydrogen conversion are

shown in Figure 35 for the experiments at -20 °C for the coupled and single reaction of $\text{LaNi}_{4.85}\text{Al}_{0.15}$, and at 20 °C for the single reaction of C5.

For the coupled reactions (Figure 35, left) the experiments at ambient temperature of -20 °C, regenerated at 130 °C and a HTF mass flow of 250 kg/h are compared. The course of the pressure and the specific thermal power are very similar. In experiment 2 (green solid line) a marginal higher peak value of 0.64 kW/kg is reached compared to 0.61 and 0.60 kW/kg of the other two experiments (10 and 16), but is still within the same range. The integration of the reached power level over the measurement duration leads to excellent agreement of the courses and end values for the hydrogen conversion.

The compared experiments for the single reaction of $\text{LaNi}_{4.85}\text{Al}_{0.15}$ (Figure 35, middle) were performed at -20 °C, a HTF mass flow of 250 kg/h and supply pressure of 1.5 bar. The pressure courses agree perfectly for each experiment. The measured specific peak thermal power values are between 1.39 and 1.49 kW/kg. This variance is very small and the curves still lie close together. Nevertheless, it causes a small difference in the hydrogen conversion, which is obtained by integrating the specific thermal power over time. Since no general trend can be observed, the deviation rather shows the sensitivity of the system to operation conditions.

For the single reaction of C5, the experiment at 20 °C and a HTF mass flow of 250 kg/h was repeated (Figure 35, right). As mentioned above, the experiment time of run XIII was too short and it is therefore not considered. Thus, the results of experiments XII and XIV are given. The courses of hydrogen pressure, specific thermal power as well as hydrogen conversion agree excellent.

Hence, it can be stated that no changes occurred in the material and inside the reactor and results are independent of the sequence of the experiment. Thus, the laboratory experiments show excellent repeatability.

Therefore, one experiment for each condition was chosen and is used for the discussions in the following (bold in Table 11 and Table 12).

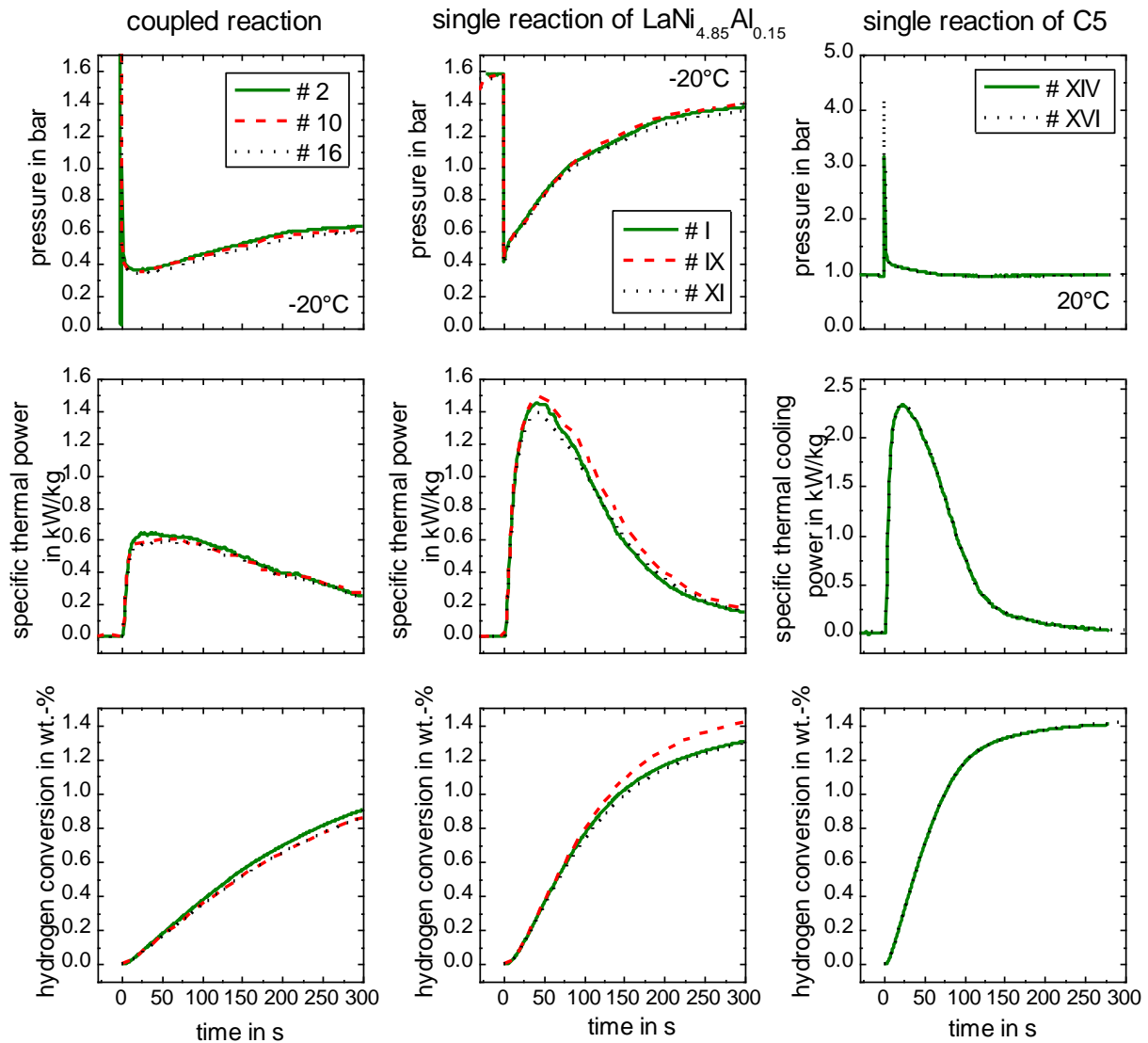


Figure 35. Repeatability of laboratory experiments

In the following sections, the results are given first for the single reaction for both materials separately and then for the coupled reactions. In the subsequent chapter 4, the influencing factors on the specific thermal power are identified by comparing both single and coupled laboratory experiments and taking the material properties from chapter 2 into account.

3.2. Single reaction

Due to the complexity of the coupled reactions, where any change of a parameter influences all others, the single reactions of both materials were investigated separately.

3.2.1. Absorption of $\text{LaNi}_{4.85}\text{Al}_{0.15}$

Possible influencing factors on the specific thermal power have been varied for the single reaction of $\text{LaNi}_{4.85}\text{Al}_{0.15}$, such as the HTF mass flow, the ambient temperature and the hydrogen supply pressure. The material was regenerated at 130 °C and 1 bar. Then, the reactor was tempered to the intended ambient temperature, and the hydrogen supply pressure and designated HTF mass flow were set. After steady state, the valve was opened to trigger the reaction.

Variation of mass flow of heat transfer fluid

The mass flow of HTF was varied between 250 and 425 kg/h at -20 °C and with a hydrogen pressure of 1.5 bar. The results are depicted in Figure 36. The experiment with higher mass flow shows a specific thermal peak power of 1.55 kW/kg. This value is only slightly above the experiment with lower mass flow, which reaches a value of 1.45 kW/kg. The effect can be seen only within the first 100 s, after this, both curves meet and then follow the same path. The hydrogen conversion increases slightly faster for the higher mass flow, then continues with a distance to the curve of the lower flow. Considering the measurement uncertainty indicated as error bars close to the end of the reaction, quite similar overall hydrogen conversions are reached.

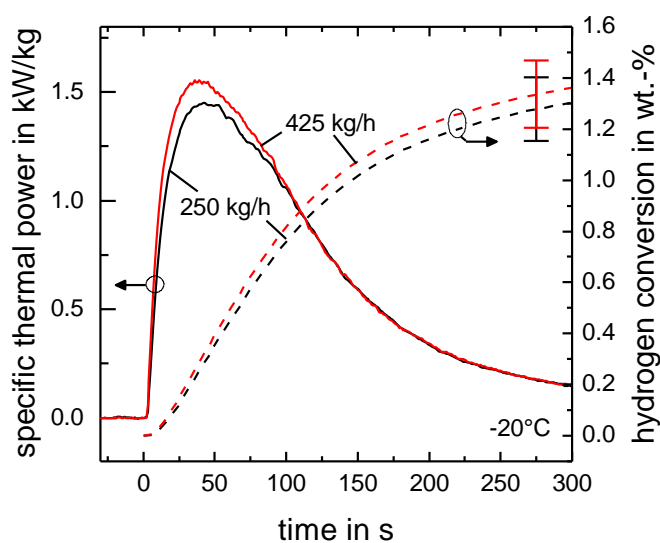


Figure 36. Single reaction of $\text{LaNi}_{4.85}\text{Al}_{0.15}$ – Variation of HTF mass flow, including measurement uncertainties of hydrogen conversion (exp. #I, II)

At the given experiments, the mass flow was almost doubled, however, only marginal benefits can be observed. Therefore, the limitation at these conditions seems to be on the bed side. The hydrogen supply pressure of 1.5 bar is more than 10 times higher than the material equilibrium pressure at -20 °C of 0.12 bar. The distance to the thermodynamic equilibrium seems therefore large enough. Since the constant supply pressure leads to an almost constant equilibrium temperature, the resulting driving temperature difference between reacting material and HTF seems to limit the heat exchange, independent of the HTF mass flow. The effect of the pressure distance to equilibrium on the specific thermal power is further investigated later in this section.

Variation of ambient temperature at constant pressure

The ambient temperature was varied between -20 and 20 °C for a supply pressure of 3 bar and between -20 and 0 °C for a supply pressure of 1.5 bar. For all experiments, the HTF mass flow was 250 kg/h. The results of the specific thermal powers and hydrogen conversions are given in Figure 37. The trends are the same for both supply pressures. The specific thermal power decreases with higher ambient temperature and the time of heat supply increases. The peak values for 3 bar are 2.67, 2.20 and 1.57 kW/kg for -20, 0 and 20 °C, respectively, and 1.45 and 1.07 kW/kg for -20 and 0 °C, respectively, for 1.5 bar. A similar trend is evident for the hydrogen conversion. For higher ambient temperatures, the slope decreases and it takes more time to reach the final value. Considering the measurement uncertainty indicated close to the end of the reaction, the final values of the hydrogen conversion agree well for each supply pressure value.

At a first glance, these findings of decreasing specific thermal power at increasing temperature seem to be in contradiction to Arrhenius's law. However, since the supply pressure is fixed, a decrease of the starting temperature of the reaction leads to a higher distance to the respective equilibrium temperature at the given pressure. Therefore, the increased temperature difference to the HTF allows faster heat exchange and hence higher thermal power. An impact of the starting temperature is not visible. In order to affirm this statement, the pressure gradient at a constant temperature is also investigated in the following section.

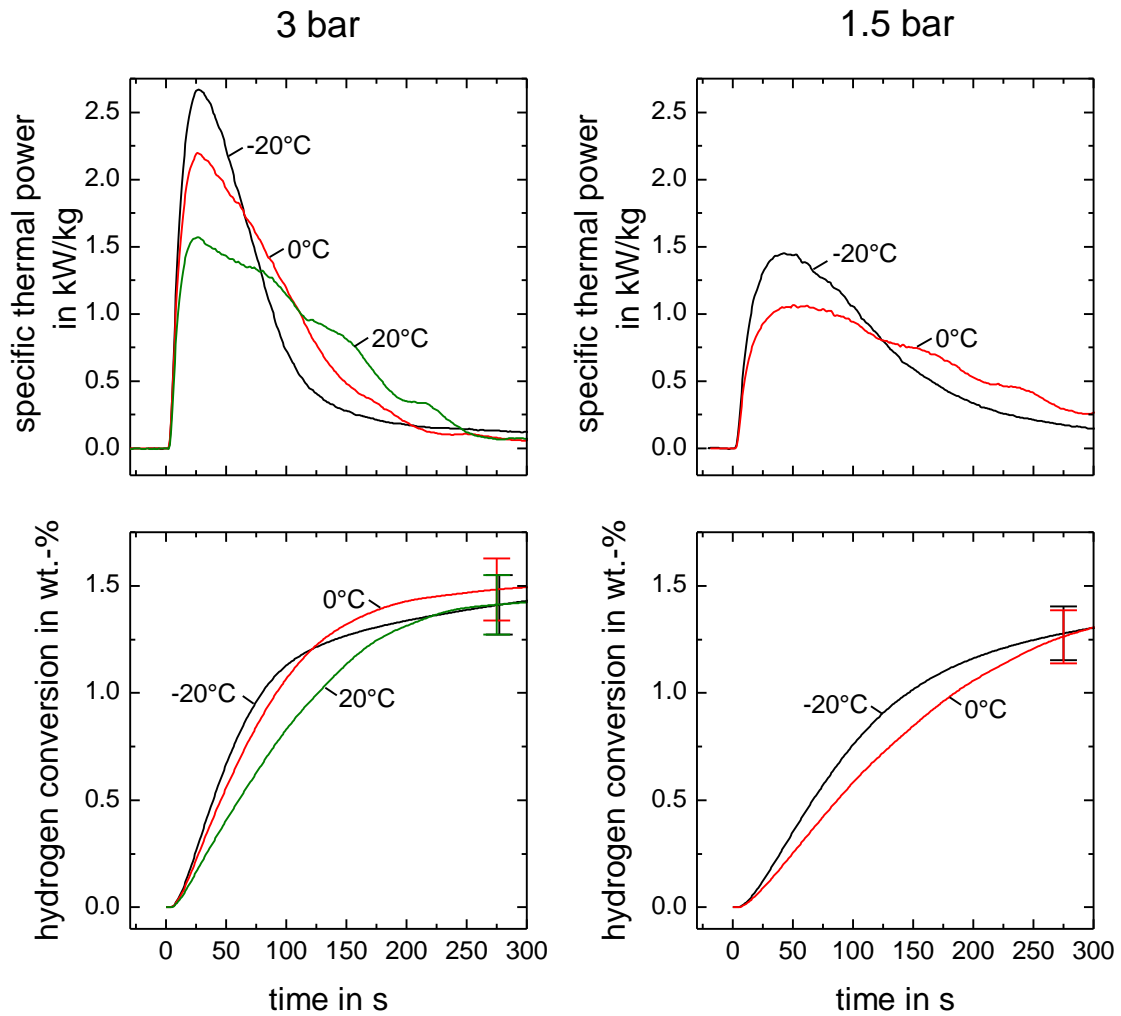


Figure 37. Single reaction of $\text{LaNi}_{4.85}\text{Al}_{0.15}$ – Variation of ambient temperature, including measurement uncertainties of hydrogen conversion (exp. #I, IV, V, VI, VII)

Variation of supply pressure at constant temperature

The supply pressure was varied between 1.5 and 10 bar for an ambient temperature of $-20\text{ }^{\circ}\text{C}$ and between 1.5 and 3 bar for an ambient temperature of $0\text{ }^{\circ}\text{C}$. The resulting specific thermal powers and hydrogen conversions are shown in Figure 38. For both simulated ambient temperatures, the specific thermal power increases significantly with supply pressure both in slope and peak value. The reached peak values for $-20\text{ }^{\circ}\text{C}$ are 1.45 kW/kg at 1.5 bar, 2.67 kW/kg at 3 bar and 5.36 kW/kg at 10 bar, respectively. For $0\text{ }^{\circ}\text{C}$, they are 1.07 kW/kg at 1.5 bar and 2.20 kW/kg at 3 bar, respectively. The hydrogen conversion increases faster, reaches higher values and the heat production stops consequently earlier with increasing supply pressure. The maximum temperature increase of the HTF at $-20\text{ }^{\circ}\text{C}$ was 12 K at 1.5 bar and 43 K at 10 bar (not shown).

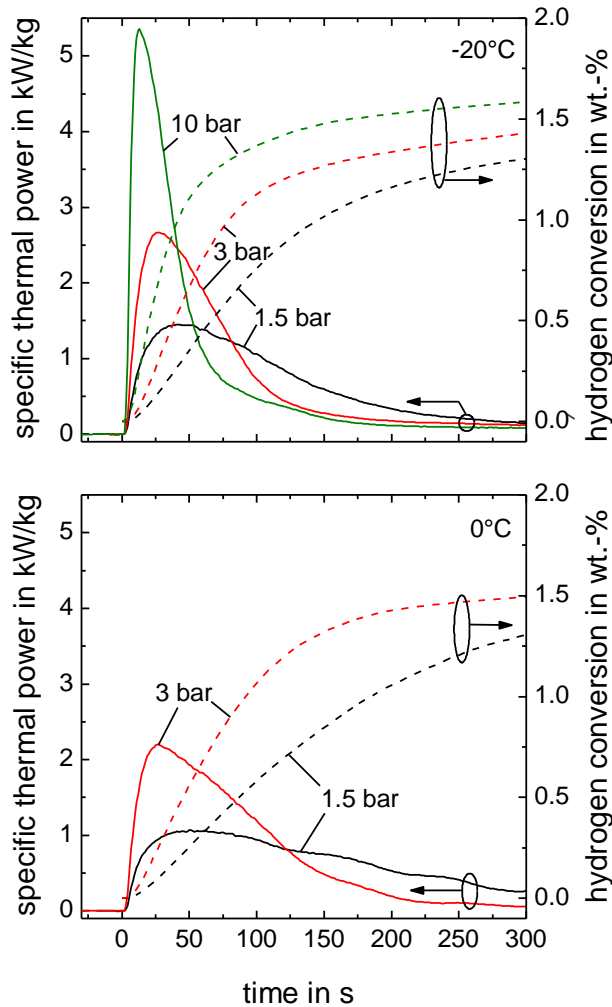


Figure 38. Single reaction of $\text{LaNi}_{4.85}\text{Al}_{0.15}$ - Variation of supply pressure (exp. #I, IV, X at -20°C and #V, VI at 0°C)

Since for the single reaction the supply pressure can be adjusted independently from the ambient temperature, a higher pressure increases intrinsically the equilibrium temperature and hence the distance to the constant HTF temperature. The larger temperature difference allows increased heat exchange and explains the increase in specific thermal power with increased supply pressure.

Therefore, even at low temperatures, the material is not kinetically limited, because it heats up during reaction, leading to increased rate coefficients. The specific thermal power rather depends on the temperature difference between material and HTF, which is determined by the supply pressure. Hence, high supply pressures allow high specific thermal power.

Conclusions from single reaction of LaNi_{4.85}Al_{0.15}

The presented results for the single reaction of LaNi_{4.85}Al_{0.15} yield specific thermal power values of more than 5 kW/kg at -20 °C. They represent the first and very high values achieved at these temperatures so far. Additionally, the temperature range investigated for metal hydrides in literature is extended further to lower temperatures, enabling considerable better prediction for preheating applications in vehicles.

Furthermore, the extensive variation of different influencing factors draws a clear picture of important effects for the specific thermal power. For the given geometry, an increase of the heat transfer onto the HTF by increased mass flow does not improve the results considerably.

Both the variation of ambient temperature and pressure lead to the same conclusion: the distance to equilibrium has a significant effect on the specific thermal power, almost independent of the temperature at which the reaction starts. This distance can be increased by lowering the temperature or increasing the supply pressure. Both effects were shown to influence the specific thermal power substantially. However, in regard to the application, the ambient temperature usually cannot be influenced. Hence, the controllable parameter of the system is the supply pressure.

Therefore, metal hydrides, in particular the investigated material, show the potential for large specific thermal power at automotive boundary conditions. The designed system can supply heat at -20 °C with a thermal peak power of more than 5 kW/kg_{MH} and 1.7 kW/kg_{system}, which would already be able to meet today's requirements with a system of a few kilograms, however, only if hydrogen is supplied externally.

3.2.2. Desorption of Ti_{0.95}Zr_{0.05}Mn_{1.46}V_{0.45}Fe_{0.09} (C5)

The response of the C5 desorption reaction was obtained at conditions close to equilibrium, in order to allow better understanding of thermodynamic limitations of the coupled reactions. Additionally, the influence of the ambient temperature was examined.

The material was regenerated at the considered ambient temperature of the subsequent discharge experiment and a hydrogen pressure of 30 bar. For discharge, the pressure was lowered to 1 bar and the valve of the reactor was opened. Due to test bench limitations, the

desorption pressure could not be varied. The generated specific cooling power is given in positive values.

Response close to thermodynamic equilibrium

The response of C5 was investigated at -20 °C and a desorption pressure of 1 bar, which correlate with the equilibrium desorption pressure at 50 % transformed fraction. The intention was to learn about the shape and magnitude of the specific thermal power of reactions close to equilibrium. This allows assessments of limitations of the coupled reactions. To verify that the reaction is actually limited due to the small distance to equilibrium, an increased HTF mass flow has to show a very similar course. Therefore, two experiments at 250 and 425 kg/h, respectively, were performed.

The resulting specific thermal power and hydrogen conversion are given in Figure 39. The shapes of both specific thermal power curves follow the same trend and show significant differences to the ones obtained at larger distances to equilibrium. A distinct, initial thermal peak is observed, which, however, decreases rapidly within less than 50 s. Then, the curve continues almost as a straight line at low power values for a long time. This trend is different to the typical observed courses with a steep increase at the beginning and slower, curved decrease after the peak value was reached.

The fast reaction indicated by the initial peak occurs during the dissolution of the β -phase for approx. 0.2 wt.-% of released hydrogen. Here, the pressure difference to the constant system pressure is extremely large and hence enables fast reaction. Within this short period, increased heat transfer by higher HTF mass flow yields also higher peak values (1.01 kW/kg at 250 kg/h and 1.23 kW/kg at 425 kg/h). Thereafter, however, the courses for both mass flow rates meet after about 25 s and follow the same path from then on. The linear shape can be explained by the thermodynamic limitation. The decreasing specific thermal power value follows the decreasing pressure difference from the sloped equilibrium pressure to the constant system pressure, which results in a constantly decreasing temperature difference. The hydrogen conversion fits well to this explanation. During the higher thermal peak at higher HTF mass flow, marginal more hydrogen is desorbed. After the specific thermal power curves meet, the hydrogen conversion curves continue with a constant distance, independent of the HTF mass flow.

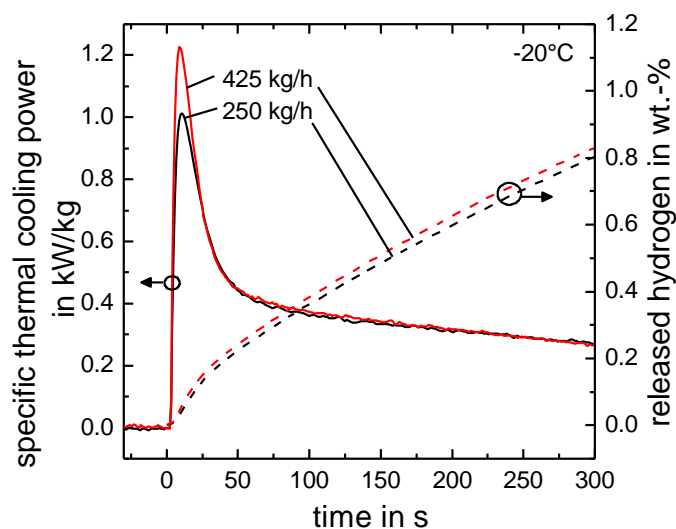


Figure 39. Single reaction of C5 – Response close to equilibrium (exp. #XVI, XVII)

These experiments show a considerably different course of the thermal power compared to conditions further away from equilibrium. This shape is not influenced by a change in HTF mass flow. Therefore, the results show the effect of conditions close to equilibrium on the thermal power.

Variation of ambient temperature at constant pressure

For the experiments in this section, the temperature was varied between 10 and 20 °C at a constant HTF flow rate of 230 - 250 kg/h and desorption pressure of 1 bar. For both experiments, the system pressure and the material temperature are given in Figure 40.

Right after the valve is opened, the pressure increases steeply and then decreases again drastically for both experiments. At the higher temperature, the pressure at the outlet of the reactor sustains higher values within the first 50 s. Both pressure curves decrease to 1 bar after around 100 s and stay there from then on. Initially, both temperature courses show a very fast, substantial temperature decrease of more than 20 K after the valve is opened, followed by a fast recovery. The curve measured at 10 °C forms a plateau at around -8 °C with even a slight temperature decrease. The temperature then rises further until the valve is closed after 184 s, leading to a slightly steeper increase of the temperature. The measured temperature at 20 °C recovers faster and then, interestingly, declines again considerably. Subsequently, the curve rises continuously.

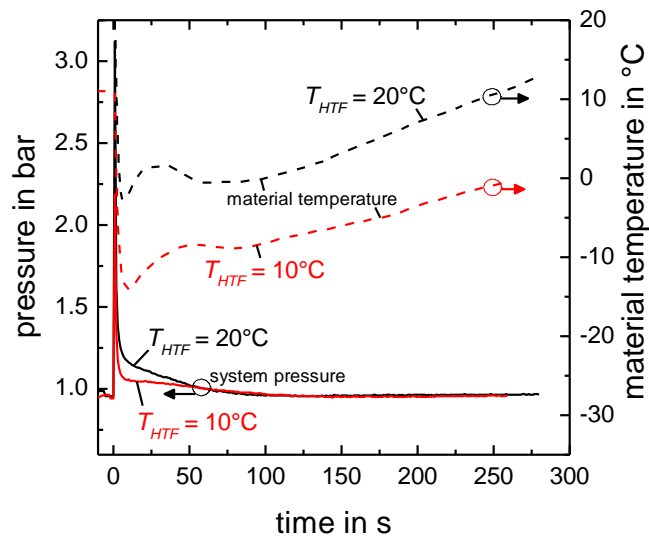


Figure 40. Single reaction of C5 – Pressure and temperature at varied ambient temperatures (exp. #XII, XV)

The steep drop in temperature at the beginning can be explained by the dissolution of the β -phase, where large differences to the system pressure occur. As the transformed fraction decreases, the pressure difference between equilibrium and system decreases. This leads to a decreased reaction rate and hence the material temperature increases. Once the PCI-plateau is reached, the temperature rises more slowly or might even form a plateau, because the equilibrium temperature at a constant pressure changes more slowly here as the hydrogen conversion decreases further. However, the plateau cannot serve as explanation for an anew decrease of the temperature. This illustrates an unexpected behavior of C5, which has not been reported yet. A similar characteristic is also observed for an experiment of the coupled reactions. This phenomenon is discussed further at the end of this chapter (cf. section 3.4).

The cooling power and the hydrogen conversion for the discussed experiments are given in Figure 41. The effect of the starting temperature of the reaction is obvious from the different curves. For 20 °C, a high peak value of 2.33 kW/kg is reached. This value decreases to 1.76 kW/kg at 10 °C. Full conversion is also reached earlier for the higher temperature, which results in a steeper decline of the specific thermal power.

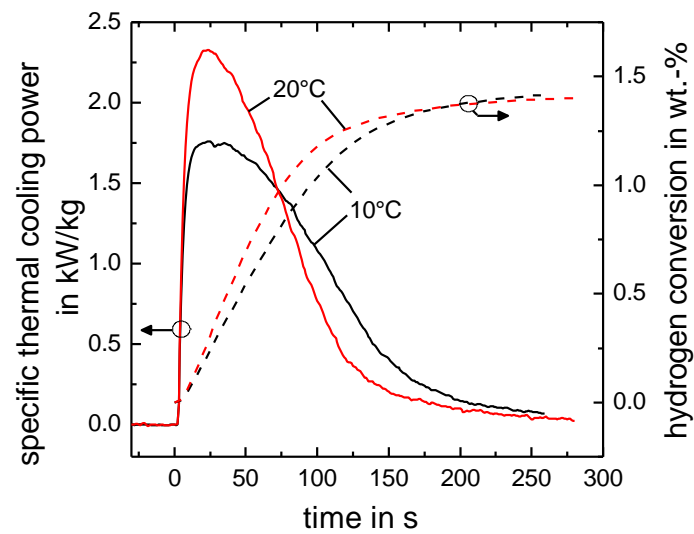


Figure 41. Single reaction of C5 – Specific thermal power and hydrogen conversion at varied ambient temperatures (exp. #XII, XV)

The higher starting temperature of the reaction results in a larger distance to the equilibrium temperature at the constant desorption pressure. This leads to a faster heat exchange and hence to higher thermal power. Therefore, the results show the large effect of the distance to equilibrium on the thermal power.

Conclusions from single reaction of C5

The material shows high specific thermal power values of up to 2.3 kW/kg at 20 °C corresponding to the largest pressure difference to the atmospheric pressure and hence to the largest temperature difference between material and HTF. A specific thermal power of 1.8 kW/kg at 10°C was obtained, which is slightly lower than the one published by Linder [81] of 2.1 kW/kg at 13 °C and higher than the one reported by Weckerle [82] of 1.3 kW/kg, however, the latter represents the mean value. Hence, the obtained value is comparable to reported specific thermal power of open systems.

The shape of the resulting thermal power curve is considerably different, if the reaction conditions are very close to equilibrium, compared to experiments further away, as shown at higher starting temperatures of the reaction. The distance to equilibrium was found to affect the specific thermal power considerably. For desorption, the distance can be increased by increased temperature or by decreased system pressure, although the latter could not be tested for the single desorption reaction due to test bench limitations. It can be achieved,

however, by a coupled reaction with another material with low equilibrium pressure. The combination with $\text{LaNi}_{4.85}\text{Al}_{0.15}$, as investigated in the next chapter, leads to reduced pressures at $-20\text{ }^{\circ}\text{C}$ as the hydrogen is sucked out of the C5 reactor.

However, for the desorbing material, the hydrogen release causes a drop in temperature and therewith a decrease of the reaction rate. Therefore, the material was selected according to its high rate coefficient values. As found in section 2.4, $\text{LaNi}_{4.85}\text{Al}_{0.15}$ shows lower rate coefficient values than C5. However, the absorption of $\text{LaNi}_{4.85}\text{Al}_{0.15}$ leads to an increase of its temperature and therefore an increase of its rate coefficient values. It has to be investigated whether the temperature decrease of C5 due to desorption poses a constraint on the coupled reactions at $-20\text{ }^{\circ}\text{C}$. The according experiments have been performed and are described in the following section.

3.3. Coupled reactions

Due to the complexity of the coupled reactions, where any change of a parameter influences all others, each material has been investigated separately with only one boundary condition variation at a time. The results showed that the heat-generating material is capable of supplying high specific thermal power even at $-20\text{ }^{\circ}\text{C}$, and the largest effect on both single reactions poses the distance to equilibrium, either in terms of temperature or pressure.

For the coupled reactions, the degree of freedom is decreased, because the desorption pressure of the hydrogen-proving material is defined by its temperature. The maximal pressure difference of the reacting pair is set by their thermodynamic properties. From a pure thermodynamic point of view, the pressure difference could be up to ten times the absorption pressure of $\text{LaNi}_{4.85}\text{Al}_{0.15}$. However, the achieved pressure difference decreases due to reaction dynamics and transport losses between the reactors and inside the beds. Therefore, this section investigates the coupled reactions related to their possible capability for preheating vehicle components as well as their influencing factors.

During regeneration, reactor 1 is tempered to the according regeneration temperature, whereas reactor 2 stays at ambient temperature. The materials are allowed to exchange hydrogen until no further change in pressure or temperature is observed and the valve is

closed. For discharge, reactor 1 is also tempered to the considered ambient temperature. At steady state, the valve is reopened to allow hydrogen flow from reactor 2 into reactor 1.

The heat exchange of the reactor was investigated by variation of the HTF mass flow. Also, the influence of different regeneration and ambient temperature levels was explored.

3.3.1. Variation of mass flow of heat transfer fluid

The mass flow of the HTF was varied between 150 and 250 kg/h for ambient temperature of -20 °C and between 150 and 425 kg/h for ambient temperature of 20 °C. The resulting specific thermal power and hydrogen conversion are shown in Figure 42. Considering the measurement uncertainty indicated as error bars close to the end of the reaction, at an ambient temperature of -20 °C (Figure 42 (a)), no deviation is evident in specific thermal power or hydrogen conversion. The specific thermal power reaches peak values of about 0.6 kW/kg. At ambient temperature of 20 °C (Figure 42 (b)), the specific peak thermal power of reactor 1 increases from 1.29 kW/kg for 150 kg/h to 1.61 kW/kg for 250 kg/h and reaches the highest values of 1.78 kW/kg for a HTF flow of 425 kg/h. The hydrogen conversion curve is steeper for higher HTF mass flows but all reach the similar end value of about 1 wt.-%.

The following conclusions can be drawn from these experiments. The overall hydrogen conversion is independent of the HTF mass flow in the investigated ranges. Only the development over time at low mass flow rates and high ambient temperatures show small sensitivity.

An increase of the HTF mass flow does not show any effect at -20 °C. However, at 20 °C, the power increases significantly with the mass flow, indicating an influence of the HTF mass flow on the overall heat transfer of the reactor at high thermal power values. Consequently, for low temperatures, the power density of the coupled reactions seems to be intrinsically limited.

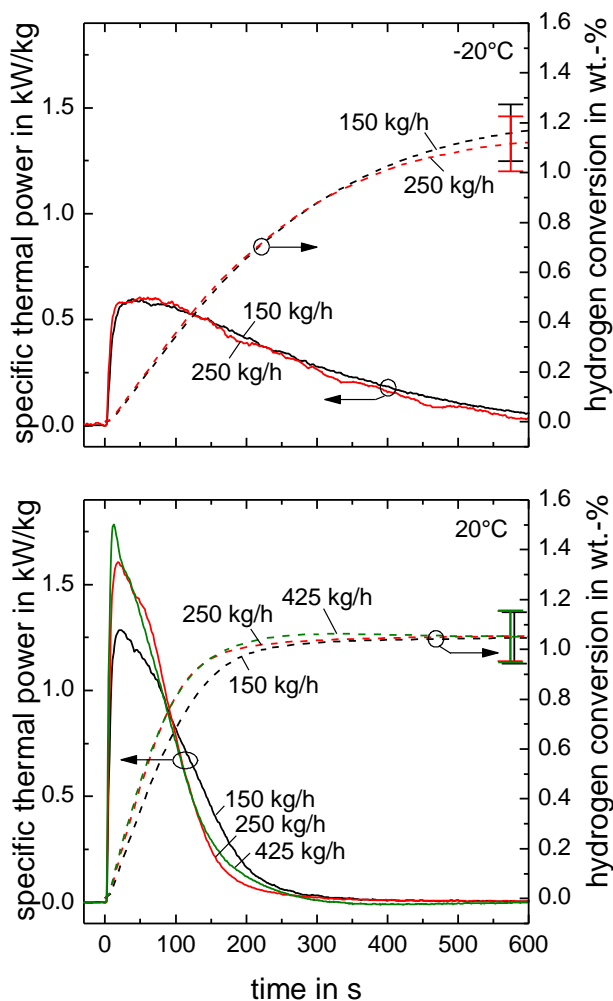


Figure 42. Coupled reactions - Variation of mass flow of heat transfer fluid, including measurement uncertainties of hydrogen conversion (exp. #12, 10 at -20 °C and #5, 1, 9 at 20 °C)

For the high thermal power demand at 20 °C, the temperature of C5 shows an interesting behavior. The course of temperature and hydrogen conversion for all three mass flows is given in Figure 43. First a steep decline in temperature with a subsequent recovery can be observed for all mass flows. This can be explained by the large pressure difference between the β -phase of C5 and the system pressure. For the lower HTF mass flows, a temperature plateau forms before rising to HTF temperature after the reaction is over. However, for a mass flow of 425 kg/h, a new decline in temperature can be observed. As also discussed for the single reaction of C5 (see section 3.2.2), a plateau formation can be explained by thermodynamics, however, a temperature decline hints to a kinetic effect. This phenomenon is discussed further at the end of this chapter (cf. section 3.4).

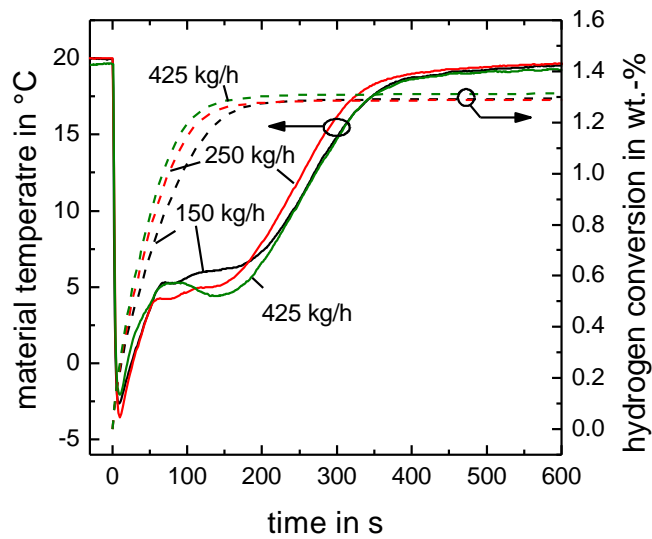


Figure 43. Coupled reactions – Temperature of C5 and hydrogen conversion for HTF mass flow variation at 20 °C (exp. #5, 1, 9)

3.3.2. Variation of regeneration temperature

For ambient temperature of -20 °C and 0 °C the regeneration temperature was varied between 90 and 130 °C. In all cases the HTF mass flow was set to 250 kg/h. The resulting specific thermal power and hydrogen conversion are shown in Figure 44. The measurement uncertainty of the hydrogen conversion is indicated by error bars.

For ambient temperature of -20 °C (Figure 44 (a)), there is no significant difference evident in the course of both the specific thermal power and hydrogen conversion. Their peak values are 0.61 kW/kg and 1.06 wt.-% at regeneration temperature of 90 °C and the same specific thermal power value and 1.10 wt.-% at 130 °C. Hence, the increase of the regeneration temperature level does not have any effect.

For ambient temperature of 0 °C (Figure 44 (b)) the course of specific thermal power and hydrogen conversion for regeneration temperatures of 110 and 130 °C agree excellent. The specific thermal power curve for the regeneration temperature for 90 °C reaches slightly lower peak values, decreases earlier and the hydrogen conversion reaches a smaller end value, indicating that 90 °C might not be sufficient for complete regeneration. The explicit values reached are 0.84, 1.07 and 1.10 wt.-% of exchanged hydrogen with thermal peak values of 1.09, 1.14 and 1.14 kW/kg at regeneration temperatures of 90, 110 and 130 °C, respectively.

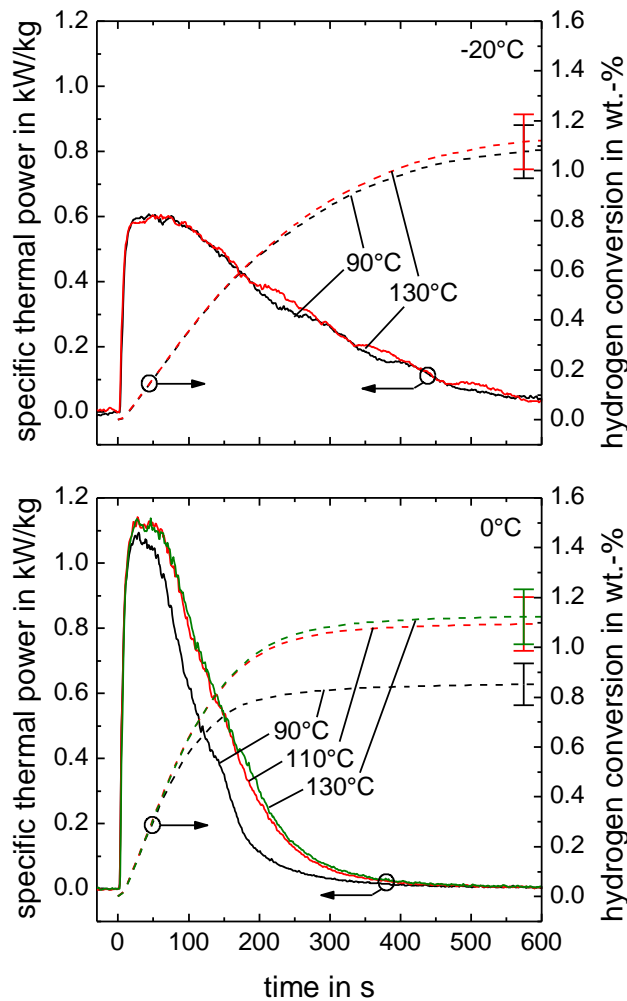


Figure 44. Coupled reactions - Variation of regeneration temperature, including measurement uncertainties of hydrogen conversion (exp. #7, 10 at -20 °C and #3, 4, 6 at 0 °C)

Consequently, at -20 °C, a regeneration temperature of 90 °C or a temperature difference of 110 K is sufficient since increasing the regeneration temperature does not have an impact on the specific thermal power. At 0 °C, however, a regeneration temperature of 110 °C is necessary to reach the highest specific thermal power value. Further increase does not improve the specific thermal power. Therefore, a certain temperature difference independent of ambient temperature has to be exceeded for complete regeneration, in the present case this value is around 110 K. A further increase does not have any positive impact on the performance of the system. The required difference is actually determined by the chosen metal hydride pair. Their distance in the van't Hoff-plot (see Figure 22) defines the required temperature difference to reach a higher pressure in reactor 1 than in reactor 2 for regeneration. The magnitude of the actually needed pressure difference is influenced by heat and gas transfer of the reactor design. The absolute temperature level plays a minor

role. Consequently, further increase of the regeneration temperature level and hence the pressure difference between the reactors does not affect the specific thermal power.

For the application in vehicles, this means that at lower ambient temperatures, a lower waste heat temperature level from the engine for regeneration is sufficient for complete regeneration as compared to higher ambient temperatures.

3.3.3. Variation of ambient temperature

Different considered ambient temperatures lead to a change of equilibrium pressure in both reactors. This affects both the thermodynamic and kinetic states of the materials and is investigated here for -20, 0 and 20 °C.

In Figure 45, the pressure gradient, the specific thermal power of reactor 1 and the hydrogen conversion is given for experiments with varying ambient temperature ($T_{\text{reg}} = 130$ °C, 250 kg/h mass flow of HTF). The measurement uncertainty of the hydrogen conversion is indicated by error bars.

The system pressure drops substantially with decreasing ambient temperature. At 20 °C, the peak pressure value is 2.5 bar, at 0 °C it is around 1 bar and at -20 °C it is around 400 mbar with a peak value of 614 mbar after 321 s. This strong dependency on the ambient temperature is also evident both in the specific thermal power and in the course of hydrogen conversion. Correspondingly, the peak values of specific thermal power increase from 0.61 kW/kg for -20 °C ambient temperature to 1.14 kW/kg at 0 °C to 1.61 kW/kg for 20 °C. The hydrogen conversion curve rises slower for lower starting temperatures. However, the end value at 600 s is comparable for all experiments (1.10, 1.10 and 1.03 wt.-% for -20, 0 and 20 °C, respectively). The maximal temperature rise of the HTF was 5 K at -20 °C and 12 K at 20 °C (not shown). These experiments were additionally performed for different values for regeneration temperature and HTF mass flow (see Table 13). In all cases, the results follow the trend described here.

Since for the coupled reactions the same ambient temperature applies to reactor 1 and to reactor 2, the pressure of the provided hydrogen changes as well. Both equilibrium pressures in the reactors decrease with decreasing ambient temperature. The pressure below 1 bar at -20 °C might limit the mass transfer in the system and therefore the reaction.

Another possibility might be reduced reaction rates of either one of the materials at lower temperatures. This point is discussed further in chapter 4.

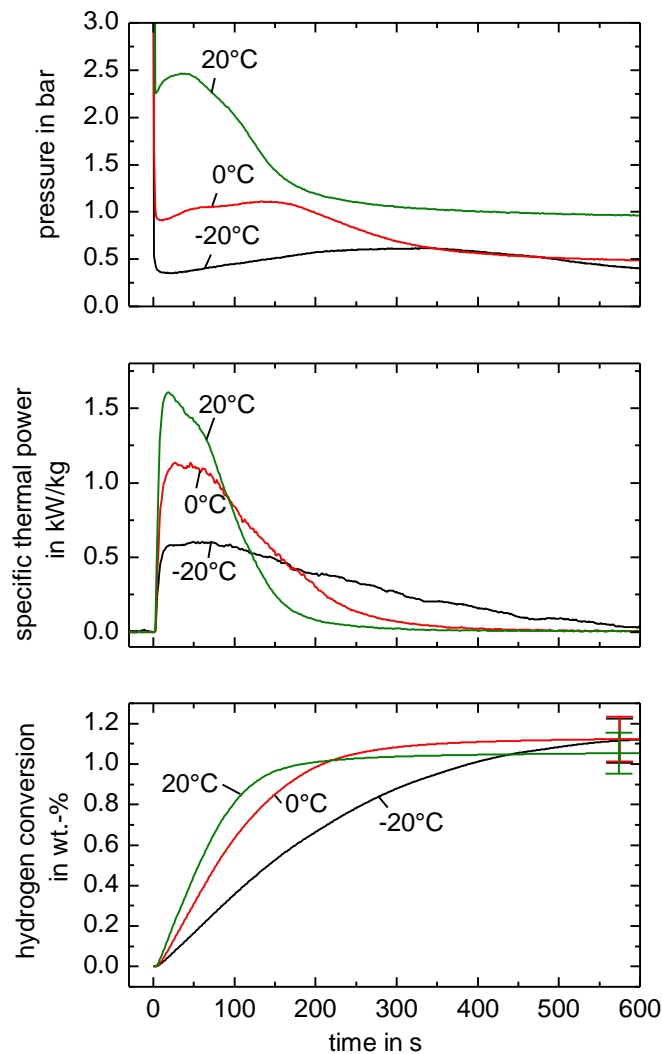


Figure 45. Coupled reactions - Variation of ambient temperature, including measurement uncertainties of hydrogen conversion (exp. #10, 6, 1)

3.3.4. Conclusions from coupled reactions

The scarce data availability for coupled metal hydride reactions in general was discussed in section 1.3.2. Additionally, no value above 500 W/kg was reported. The results of the presented study largely exceed literature values and the investigated temperature range and expand the knowledge about potential applications of metal hydride, e. g. in vehicles. Of all investigated influencing factors, such as HTF mass flow, regeneration and ambient temperature, by far the largest impact is observed for the ambient temperature.

In the given geometry, the mass flow of the HTF has only little impact on the specific thermal power and this only at high power values at high temperatures. Hence, the reactor design allows well thermal transfer onto the HTF at the considered boundary conditions.

The investigation of the regeneration temperature shows, that the distance to ambient temperature is the important value rather than the absolute temperature level during regeneration. For the investigated metal hydride couple, a temperature difference of around 110 K is found to allow complete conversion of the system.

The strong influence of the ambient temperature led to a substantial decrease of the specific thermal power with decreasing temperature. The peak value of up to 1.6 kW/kg at 20 °C decreases to 1.1 kW/kg at 0 °C and further to 0.6 kW/kg at -20 °C. This effect could be caused by different mechanisms, such as gas transport at lower pressure or limiting kinetics of either material. In order to answer this question, the comparison between the material characteristics and the results of the single and coupled reactions has to be drawn. This is discussed in the following chapter 4.

3.4. Characteristics of $\text{Ti}_{0.95}\text{Zr}_{0.05}\text{Mn}_{1.46}\text{V}_{0.45}\text{Fe}_{0.09}$ (C5)

During the investigation in laboratory scale, the hydrogen-providing material C5 revealed an interesting behavior. During experiments, in which very fast reaction is demanded from the material, the temperature course of C5 shows two negative peaks. This is the case for the single reaction at 20 °C with a high temperature difference to equilibrium (exp. # XVI), as well as for the coupled reactions at 20 °C and the highest HTF mass flow of 425 kg/h (exp. # 9). The temperature courses are given in Figure 46. Both lines show a steep decrease and a sharp peak within the first 10 s. Subsequently, both temperatures increase. Then, however, both curves show another decrease in temperature, where the peak occurs earlier and more pronounced for the single reaction than for the coupled one.

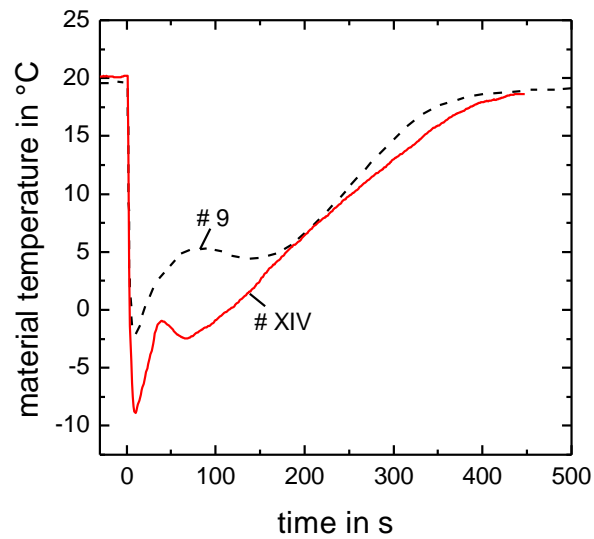


Figure 46. Temperature course of C5 at experiments with high reaction rates (single reaction at 20 °C, exp. #XIV; coupled reactions at 20 °C and HTF mass flow of 425 kg/h, exp. #9)

The behavior can be explained as follows, as already discussed in section 3.2.2. The steep drop in temperature at the beginning is caused by the dissolution of the β -phase, where large differences to the system pressure occur. As the transformed fraction decreases, the pressure difference between equilibrium and system decreases. This leads to a decreased reaction rate and hence the material temperature increases. Once the PCI-plateau is reached, the temperature rises more slowly or might even form a plateau, because the equilibrium temperature at a constant pressure changes more slowly here as the hydrogen conversion decreases further. However, the plateau cannot serve as explanation for an anew decrease. This temperature decline hints to an anew increase in the reaction kinetics of C5.

To the authors' knowledge, a decrease and subsequent increase of rate coefficients was never reported before for C5 or other Hydralloy C-materials. A detailed investigation of this behavior is beyond the scope of this work. Therefore, only an assumed theory can be given here.

In AB_2 alloys, hydrogen can occupy different interstitial in the lattice [103]. It seems reasonable, that the kinetics of the occupation is different for different types of interstitial. This could also explain the steep PCI-plateau for C5 as the result of an overlap of different processes at different equilibria.

As mentioned in the introduction section, different steps are involved during the reaction. A change of the rate determining step with increasing hydrogen conversion values might also lead to a change of the reaction rate. Such a change of the hydriding controlling step was reported in literature for other materials. E.g. a change from nucleation and growth of the hydride phase as rate controlling step to hydrogen diffusion through the hydride phase at higher hydrogen conversions was reported for LaNi₅ by Inomata et. al [70], for FeTi by Park and Lee [104] and for MIn₅ at higher pressures by Wang et. al [105].

Therefore, the decrease and subsequent increase in kinetics could be explained by either different kinetics for different interstitial or a change in rate controlling step or a combination of both.

3.5. Summary of all laboratory scale experiments

This section provides a summary of all experiments in laboratory scale for both the single and the coupled reactions. The boundary conditions, resulting specific thermal power, thermal energy and hydrogen conversion are given in Table 13. Due to the faster reaction, shorter periods for the single reactions of 300 and 60 s are considered for LaNi_{4.85}Al_{0.15} and C5, respectively. The probable error for both the specific thermal power and the hydrogen conversion was about $\pm 11\%$ for all experiments. Details on the uncertainty analysis are given in Appendix C.

As stated in the review section, no work on heat generation at temperatures below 20 °C has been published. The here presented investigations greatly enlarge the temperature range of available experiments and yield the first heat thermal power results at -20 °C published so far.

For the single reaction of LaNi_{4.85}Al_{0.15}, a specific thermal power value of more than 5 kW/kg at -20 °C is achieved. This represents the first and very high values achieved at these temperatures so far. The single reaction of C5, resulting in specific thermal power values of up to 2.3 kW/kg at 20 °C, are comparable to reported thermal cooling power of open systems.

Table 13. Specific thermal power, thermal energy and hydrogen conversion for all experiments in laboratory scale

Single reaction							
No. of exp.	T _{amb} in °C	p in bar	m _{HTF} in kg/h	P _{peak} in kW/kg _{MH}	q _{300s} in kJ/kg _{MH}	ω _{300s} in wt.-%	
LaNi_{4.85}Al_{0.15}							
I	-20	1.5	250	1.45	202.09	1.28	
IX				1.49	220.29	1.39	
XI				1.39	200.12	1.27	
II		3	250	1.55	211.15	1.34	
IV				2.67	221.58	1.40	
X				5.36	245.87	1.56	
III	1.16			200.91	1.27		
VI	0	1.5	250	1.07	202.46	1.28	
V	3	250	2.20	231.45	1.46		
VII			20	1.57	220.66	1.40	
Ti_{0.95}Zr_{0.05}Mn_{1.46}V_{0.45}Fe_{0.09} (C5)							
	T _{amb} in °C	p in bar	m _{HTF} in kg/h	P _{peak} in kW/kg _{MH}	q _{60s} in kJ/kg _{MH}	ω _{60s} in wt.-%	
XVI	-20	1	250	1.01	36.13	0.25	
XVII			425	1.23	38.78	0.27	
XV	10		230	1.76	93.20	0.66	
XII	20		250	2.33	116.98	0.82	
XIV				2.32	117.00	0.82	
Coupled reactions							
No. of exp.	T _{amb} in °C	T _{reg} in °C	m _{HTF} in kg/h	P _{peak} in kW/kg _{MH}	q _{600s} in kJ/kg _{MH}	ω _{600s, LaNi_{4.85}Al_{0.15}} in wt.-%	
8	-20	130	150	0.57	179.15	1.13	
12				0.60	181.20	1.15	
15				0.60	184.61	1.17	
2				0.64	178.52	1.13	
10				0.61	173.79	1.10	
16			250	130	0.60	167.17	1.06
7					0.61	167.91	1.06
14					0.61	169.64	1.07
6					1.14	174.22	1.10
4					1.14	169.61	1.07
13	0	110	250	1.11	169.11	1.07	
3	20	130	250	1.09	132.08	0.84	
5				1.29	162.18	1.03	
1				1.61	162.65	1.03	
11				1.58	164.23	1.04	
9				1.78	163.04	1.03	

For the coupled reactions, the value of 600 W/kg at -20°C exceeds the specific thermal power value of 480 W_{heat}/kg by Qin [80]. It is slightly smaller than the result of 780 W_{cold}/kg by Linder [43]. However, both values have been obtained at 20 °C, hence at 40 K above the presented one. At comparable temperature, a specific thermal peak power of 1.6 kW/kg was obtained in this work. Therefore, the achieved values of this work can be considered exceptionally high.

The results additionally allow conclusions about the influencing factors on the specific thermal power. The single reaction of LaNi_{4.85}Al_{0.15} shows very fast reaction rates even at low temperatures, if the supply pressure is high enough. The distance to equilibrium, either by decreased temperature or increased pressure, is found to be the most important influencing factor on the specific thermal power, whereas the impact of the starting temperature only plays a secondary role. The large effect of the distance to equilibrium is also found for the single reaction of C5. A very small distance results in a distinctly different shape of the thermal power. Larger distances realized by higher temperatures lead to increased thermal power values.

The largest impact on the coupled reactions has by far the ambient temperature. The mass flow of the HTF only shows small effects at high power rates, which shows that the heat transfer of the design does not pose strong limitations on the reaction. The system is fully charged if the regeneration temperature is around 110 K higher than ambient, independent of the ambient temperature level itself. Further increase has no effect on the specific thermal power. However, the specific thermal power declines significantly at lower ambient temperatures. From 20 °C to -20 °C, the value decreases from 1.6 kW/kg by almost 2/3 to 0.6 kW/kg.

The cause for this effect cannot be concluded only by the laboratory scale measurements and is discussed in the following chapter 4. It combines the results of the laboratory scale measurements with the determined material properties. A detailed discussion on the factors influencing the specific thermal power is provided and a conclusion is drawn.

4. Discussion and conclusion

In this chapter, all findings are discussed against the background of the material properties as well as the laboratory experiments of the single and coupled reactions in relation to the automotive boundary conditions. This allows detailed assessment of the limiting factors on the specific thermal power. From these results, conclusions on metal hydrides at automotive boundary conditions are drawn and proposals for future applications are derived.

4.1. Factors influencing the specific thermal power

Different influencing factors have been investigated by systematic variation of experimental boundary conditions. The heat transfer onto the HTF was varied by varying the HTF mass flow. The results allow conclusions on the heat exchange through the reactor at the given conditions. The effect of the distance to equilibrium was investigated for the single reactions. For $\text{LaNi}_{4.85}\text{Al}_{0.15}$ both the ambient temperature and the supply pressure were varied separately. C5 was investigated at conditions close to equilibrium as well as at varied temperatures. The influence of the ambient temperature was also investigated for the coupled reactions. Additionally, the regeneration conditions for the coupled reactions were investigated by varying temperature levels supplied to $\text{LaNi}_{4.85}\text{Al}_{0.15}$.

For the variation of the HTF mass flow, a slight influence is observed only at very high specific thermal power. This is the case at high distances to equilibrium as thermodynamic driving force for the single reaction and high ambient temperature for the coupled reactions. However, the change of the specific thermal power is small compared to other influencing factors. Hence, the reactor design proves sufficient heat transfer for the considered boundary conditions.

The distance to equilibrium for the single reactions shows a substantial effect on the specific thermal power. Its influence is much greater than the effect of the ambient temperature, at which the reaction starts. This is quite noticeable, because thereby high specific thermal power can be realized easily if hydrogen at adequate pressure is available. It also has to be considered for the coupled reactions, where the supply pressure of C5 decreases naturally with decreasing temperature.

A regeneration temperature for the coupled reactions has to reach levels of around 110 K above ambient. Then, full conversion is possible. This can be explained by the distance of the thermodynamic equilibrium of the material pair, which has to be overcome but is almost independent of the temperature level in the considered range. For the vehicle application, this means that at lower ambient temperatures, the engine does not have to reach such high temperature levels to trigger regeneration compared to higher ambient temperatures.

The ambient temperature shows a large influence on the specific thermal power of the coupled reactions. The specific peak thermal power decreases by more than 30 % from 20 to 0 °C and by 45 % from 0 to -20 °C.

A comparison with the single reactor experiments of C5 very close to equilibrium showed that the specific thermal power changes quite differently over time. Therefore, the cause for the observed decrease in specific thermal power cannot be attributed to thermodynamic limitations. Instead, an explanation based on the material properties could be identified as described in the following.

A correct prediction of the material behavior without knowing the local temperature and pressure courses throughout the reactor is difficult. Hence, in order to identify possible limitations, the experimental results have to be compared to predictions by the thermodynamic and kinetic behavior of each material (see equation (5) and (9)). The prediction and the experimental results will agree in case one of these phenomena actually poses the limitation on the observed process. All results have been carefully examined in this regard.

The measured system pressure of the coupled reactions was not predictable only by thermodynamics. However, the kinetics consideration allowed an explanation of the behavior. Exemplary kinetic fits for every temperature are given in Figure 47, resulting in apparent rate coefficients for the laboratory scale experiments. For the experiments at 20 °C (Figure 47, bottom), a kinetic fit was not possible. The ratio of the antiderivative of the reaction mechanism and pressure dependence function did not lead to a straight line. Consequently, it can be assumed that the observed process is not limited and hence described correctly by the kinetic correlation. For 0 and -20 °C, however, such a fit was possible, as can be seen at the top of Figure 47. The fit for -20 °C yielded a close match with

a coefficient of determination of 99.3 %, whereas for 0 °C, the fit only revealed a coefficient of determination of 94.1 %. This can also be observed in the diagram, where the line from the experiment shows a kink. Therefore, limitations other than the kinetics might overlap and also influence the reaction rate in the large scale experiments at 0 °C.

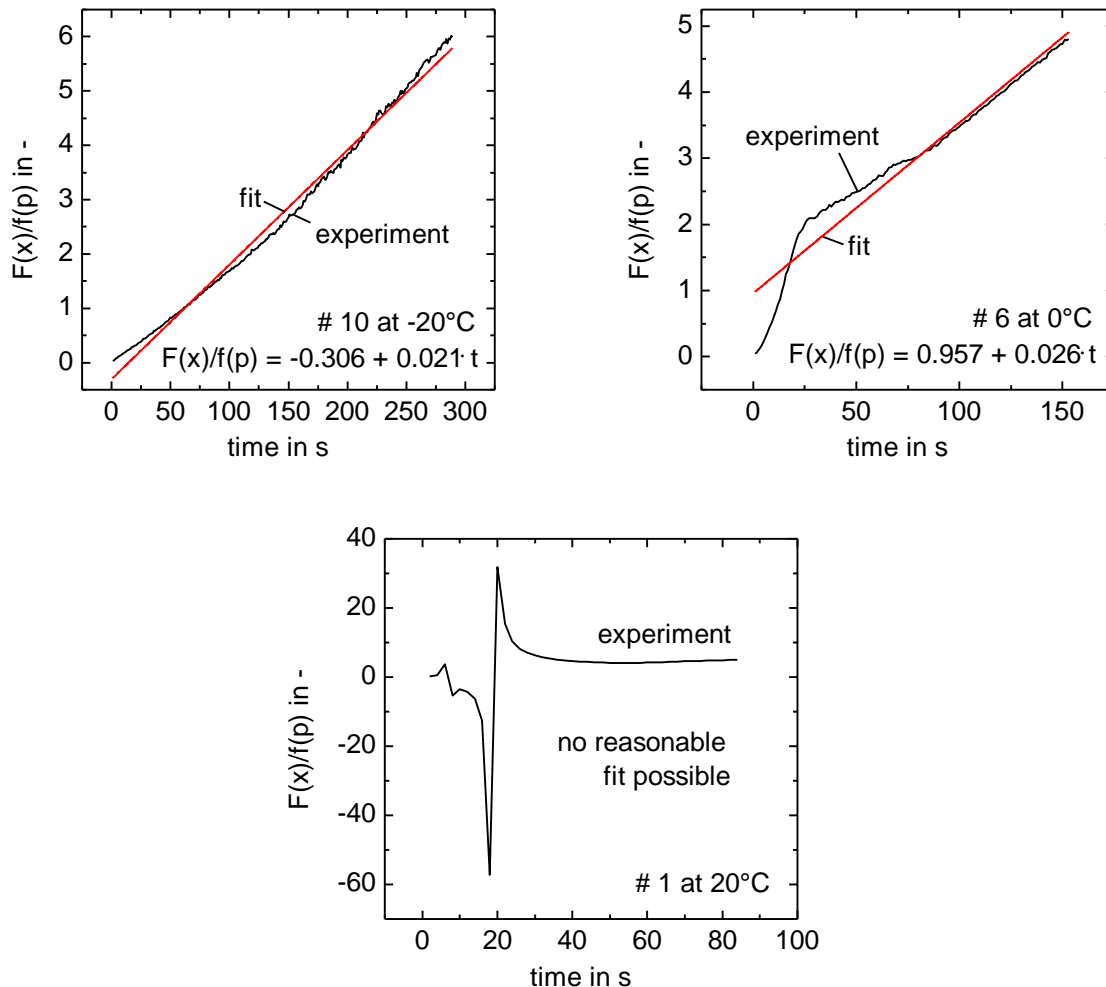


Figure 47. Kinetic fits of laboratory scale experiments

This conclusion is coherent for all resulting apparent rate coefficients, which are given in Figure 48. The values for all variations at -20 and 0°C are included at the average temperature of the material during reaction.

For all experiments at -20°C and a HTF mass flow of 250 kg/h (exp. # 10, 7), the apparent rate coefficients lie exactly on the extended line of the rate coefficient of C5, independent of the regeneration temperature. For the lower HTF mass flow (exp. # 12), the resulting apparent rate coefficient shows a slightly smaller value than the intrinsic rate coefficient at the same temperature. This implies, that the overall heat transfer for the higher mass flow

provides desorption heat to the material just as fast as it is consumed. The lower mass flow does not quite meet this requirement and, hence, causes the slightly smaller apparent rate coefficient. Overall, the intrinsic kinetics of C5 must be the limiting factor on the coupled reactions at -20 °C.

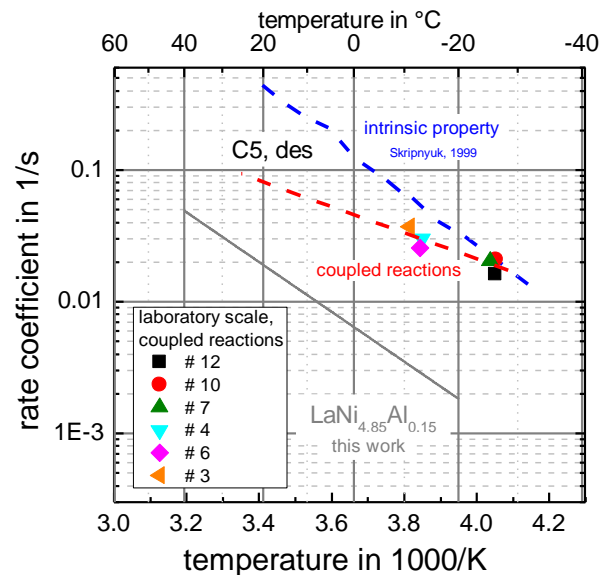


Figure 48. Apparent rate coefficients of the coupled reactions at 0 and -20 °C and the rate coefficients for $\text{LaNi}_{4.85}\text{Al}_{0.15}$ (this work) and C5 [60]

The apparent rate coefficients for the experiment at 0 °C (exp. # 3, 4, 6) show a larger distance to the intrinsic rate coefficient line. This distance increases marginal for higher regeneration temperatures.

Since no apparent rate coefficient could be determined for higher temperatures, the reaction is assumed to be limited by the heat transfer through the reactor. This is affirmed by the observation that at high specific thermal power at high temperatures, even higher values can be reached by increased HTF mass flow.

Due to the absorption heat released during the reaction of $\text{LaNi}_{4.85}\text{Al}_{0.15}$, this material increases its temperature and therefore can accelerate itself. As shown for the single reaction, higher supply pressure and therefore higher equilibrium temperature allows faster reaction and higher specific thermal power even at -20 °C. For that reason, although the intrinsic material rate coefficient is lower than for C5 at the same temperature, it is not this side of the reaction which limits the specific thermal power.

From this discussion, it can be concluded that the coupled reactions at $-20\text{ }^{\circ}\text{C}$ is limited by the reaction kinetics of C5. The specific thermal power at $20\text{ }^{\circ}\text{C}$ is limited by the overall heat transfer and at $0\text{ }^{\circ}\text{C}$ both effects overlap to some extent.

4.2. Conclusion

The results of this thesis show the potential of metal hydrides to reach high specific thermal power at automotive boundary conditions. High values of more than 5 kW/kg can be achieved at $-20\text{ }^{\circ}\text{C}$. For the single reaction, the distance to equilibrium as thermodynamic driving force is the main influencing factor. However, severe restrictions are observed for the coupled reactions. Here, only values up to 0.6 kW/kg are obtained at $-20\text{ }^{\circ}\text{C}$. It was found that, although C5 shows one of the highest rate coefficients for metal hydrides, for the coupled reactions at $-20\text{ }^{\circ}\text{C}$, this material constitutes the limitation on the specific thermal power.

From these findings, the following conclusions for the application of metal hydrides in vehicles are drawn:

The main result is the fact, that the specific thermal power of the investigated coupled reactions at low temperatures is not limited by the reactor design but depends on material properties. Hence, no increase can be reached by optimized heat transfer. This constitutes a new finding, because, usually, the fast metal hydride reaction in large scale is limited by the heat transfer.

In order to realize sufficient hydrogen supply in a closed system for internal combustion engines, two possible solutions are discussed. The simplest would be to use a material with higher rate coefficients, however, no such material for the given thermodynamics is known today. Alternatively, a different material with higher equilibrium pressure could be used as hydrogen-providing material. Sufficiently high pressure could be supplied even if the reaction is kinetically limited. However, such a system would require much higher temperature levels for regeneration (cf. Figure 6).

For future automotive applications, another type of preheater seems very promising. If hydrogen is available from the vehicle infrastructure, e.g. in fuel cell vehicles, fast gas supply

and hence very high specific thermal power can be achieved. Additionally, the system weight would decrease by half, because no hydrogen-providing material is necessary.

Such vehicles also have difficulties at subzero conditions. If a proton exchange membrane fuel cell (PEMFC) is operated below 0 °C, the produced water might freeze and form an ice layer, which prevents gas flow and the expansion in volume can cause mechanical destruction of the fuel cell. The application in vehicles therefore requires water management at ambient temperatures below 0 °C. Besides drying after shut down, fast temperature rise at the start is required. When restarting, the membrane has to be wetted which requires temperatures above freezing point. So the fuel cell needs to be preheated to temperatures above 0 °C in order to avoid degradation and hence prolonging life time significantly. Today, one state of the art start-up mode increases the temperature by running the fuel cell dry and therefore with large electrical resistance. This produces waste heat and heats up the fuel cell. However, this also leads to degradation of the fuel cell. Another applied start-up mode uses a positive temperature coefficient (PTC) heater run by precious electrical energy, which then isn't available for propulsion anymore. [106]–[109]

Therefore, a preheating system driven by surplus onboard energy could improve the fuel cell start-up phase substantially. Automotive hydrogen is usually stored in high pressure tanks up to 700 bar. However, the fuel cell only requires pressures below 5 bar. Until now, this compression work stored in the tank - which required around 15 % of the energy stored in the hydrogen itself [110] - is throttled unused and lost. Using energy readily available on board additionally increases the efficiency of the vehicle compared to state of the art operation. Such a thermal energy storage could be regenerated during driving by desorbing hydrogen to the fuel cell at low pressure, if necessary using waste heat from the fuel cell.

This design has an additional potential advantage. The metal hydride container can be integrated directly into the fuel cell, because the thermal energy is stored as chemical potential and the material can be allowed to cool to ambient temperature. This enables fast heat exchange from the preheater directly to the region of demand without the help of a heat transfer fluid. Therefore, less thermal energy is required, because no parasitic thermal mass of the HTF has to be heated. Additionally, the same reaction temperature level can increase the fuel cell temperature to a higher level, because a smaller temperature gradient is required due to the direct heat conduction.

Such a system could also be reasonable economically. Prices for the similar LaNi_5 are reported by Young [19] to 13 \$/kg. This price can be expected to drop for large-scale mining. Additionally, investigations on substitutions of expensive elements by less pure components have been performed e.g. by Ulmer et. al [111] and can potentially decrease the price further. Since only a small amount of material is necessary for the preheater, the system price can be assumed in affordable ranges.

As this thesis showed, this large distance to equilibrium as thermodynamic driving force would allow high specific thermal power for fuel cell preheating. With comparably low pressure of 10 bar, specific thermal power above 5 kW/kg was achieved. Therefore, such a directly integrated preheater could help pave the way for broad market introduction of fuel cells and hence for a carbon-free mobility.

5. Summary and outlook

The automotive boundary conditions during cold start pose severe restrictions on a preheater based on coupled metal hydride reactions. Little is known about metal hydrides at subzero conditions. This includes both material properties and laboratory scale specific thermal power investigations, in particular for coupled reactions. Moreover, no systematic investigation of possible influencing factors has been determined yet. This knowledge, however, is pivotal for appropriate preheater design for vehicle cold start phases.

In this work, $\text{LaNi}_{4.85}\text{Al}_{0.15}$ and Hydralloy C5, rechargeable with onboard waste heat of 90 to 130 °C, were selected to provide thermal energy at ambient temperatures between -20 and 20 °C. The available data lack investigations of material properties at temperature below 0 °C and of coupled metal hydride reactions and their power potential at -20 °C. Therefore, the materials were characterized, and influencing factors on the specific thermal power were investigated thoroughly in laboratory scale. Due to the complexity of coupled reactions, isolated influencing factors were investigated in a single reaction. Then, boundary conditions were varied for the coupled reactions and, including all results of this thesis, the main factors of influence were identified.

Pressure-concentration isotherms were obtained between -20 and 130 °C for $\text{LaNi}_{4.85}\text{Al}_{0.15}$ and between -30 and 35 °C for C5. Additionally, the kinetic properties of $\text{LaNi}_{4.85}\text{Al}_{0.15}$ have been investigated between -20 and 40 °C. Here, the effect of nickel substitution by aluminum was found to increase the rate coefficient. The results provide the first thermodynamic and kinetic data for these materials at such low temperatures and reveal the promising fit of the selected pair to the considered boundary conditions.

Based on the single reaction experiments of $\text{LaNi}_{4.85}\text{Al}_{0.15}$, the very fast reaction rates even at low temperatures were shown. The distance to equilibrium was found to be the most important influencing factor on the specific thermal power, whereas the impact of the actual starting temperature only plays a secondary role. At 10 bar, a thermal peak power of more than 5 kW/kg at -20 °C was achieved. The large effect of the distance to equilibrium was also found for the single reaction of C5. The highest power level for desorption was reached at 20 °C, corresponding to a specific thermal cooling power of 2.3 kW/kg.

The results for $\text{LaNi}_{4.85}\text{Al}_{0.15}$ represent the first and very high values achieved at these temperatures so far. The results for C5 are comparable to reported specific thermal power of open systems.

Based on the detailed experimental investigation of the coupled reactors, a better understanding of main influencing factors, such as heat transfer, material properties and the coupled pressure level, has been reached. Of all investigated influencing factors, like HTF mass flow, regeneration and ambient temperature, by far the largest impact on the coupled reactions was observed for the ambient temperature.

The system was fully charged if the regeneration temperature was around 110 K higher than ambient, independent of the ambient temperature level itself. This distance is defined by the thermodynamics of the chosen material pair. Further increase had no effect on the specific thermal power. However, the specific thermal power declined significantly at lower ambient temperatures. From 20 °C to -20 °C, the specific thermal power decreased from 1.6 kW/kg by almost 2/3 to 0.6 kW/kg. After careful consideration of all experiments and material properties, the kinetics of the hydrogen-providing material C5 was found to cause this limitation at low temperatures.

These investigations greatly enlarge the temperature range investigated yet and yield the first and by far the highest specific thermal power values for both the single and, in particular, the coupled reactions.

The largest contribution of this work is, however, the gained insight into the influencing factors on the specific thermal power of coupled metal hydride reactions at low temperatures. It revealed that the specific thermal power of the coupled reactions at low temperatures was not limited by the reactor design but depends on material properties. Hence, an increase of specific thermal power cannot be reached by optimized heat transfer. This constitutes a new finding, because, usually, the fast metal hydride reaction in large scale is limited by heat transfer.

Besides the possibility to increase the reaction rate of the hydrogen-supplying material, a directly integrated preheater for fuel cells was theoretically developed. Driven by the hydrogen pressure gradient between tank and fuel cell, such a system is not limited by chemical desorption, and could improve the fuel cell start-up phase substantially. This might

help to pave the way for broad market introduction of fuel cells and hence for a carbon-free mobility.

This work presents the first investigations of influencing factors of coupled metal hydride reactions at low temperatures. More data is needed in order to review existing and new simulation models and help predict the reaction behavior of the complex and highly interacting reactions. Furthermore, the development of metal hydride based preheater should be continued to contribute to a sustainable future mobility.

References

- [1] Umweltbundesamt.de, "Emissionen ausgewählter Luftschadstoffe nach Quellkategorien," *Nationale Trendtabellen für die deutsche Berichterstattung atmosphärischer Emissionen seit 1990, Emissionsentwicklung 1990 bis 2013*, 2015. [Online]. Available: <https://www.umweltbundesamt.de/daten/luft/luftschadstoff-emissionen-in-deutschland/stickstoffoxid-emissionen#textpart-1>. [Accessed: 02-Mar-2018].
- [2] Umweltbundesamt.de, "Fahrleistung im Personen- und Güterverkehr in Deutschland," 2015. [Online]. Available: <https://www.umweltbundesamt.de/daten/verkehr/fahrleistungen-verkehrsaufwand-modal-split#textpart-1>. [Accessed: 21-Mar-2018].
- [3] D. Klamann, *Lubricants and Related Products - Synthesis, Properties, Applications, International Standards*. Weinheim: Verlag Chemie GmbH, 1984.
- [4] M. S. Reiter and K. M. Kockelman, "The problem of cold starts: A closer look at mobile source emissions levels," *Transp. Res. Part D Transp. Environ.*, vol. 43, pp. 123–132, 2016.
- [5] D. Di Battista and R. Cipollone, "Experimental and numerical assessment of methods to reduce warm up time of engine lubricant oil," *Appl. Energy*, vol. 162, pp. 570–580, 2016.
- [6] R. Cipollone, D. Di Battista, and M. Mauriello, "Effects of oil warm up acceleration on the fuel consumption of reciprocating internal combustion engines," *Energy Procedia*, vol. 82, pp. 1–8, 2015.
- [7] D.-W. Lee, J. Johnson, J. Lv, K. Novak, and J. Zeitsman, "Comparisons between vehicular emissions from real-world in-use testing and epa moves estimation," Report No. SWUTC/12/476660-00021-1, Texas Transportation Institute, 2012.
- [8] D. K. Deppenkemper, M. Günther, and P. Stefan, "Development of optimized exhaust gas heating strategies for passenger car Diesel engines by means of variable valve train applications," in *17. Internationales Stuttgarter Symposium*, 2017, pp. 123–142.
- [9] C. Dardiotis, G. Martini, A. Marotta, and U. Manfredi, "Low-temperature cold-start gaseous emissions of late technology passenger cars," *Appl. Energy*, vol. 111, pp. 468–478, 2013.
- [10] Q. Fan and L. Li, "Study on first-cycle combustion and emissions during cold start in a TSDI gasoline engine," *Fuel*, vol. 103, pp. 473–479, 2013.
- [11] S. Q. A. Rizvi, *A Comprehensive Review of Lubricant Chemistry, Technology, Selection, and Design*. West Conshohocken, PA: ASTM International, 2009.
- [12] J. S. Jadhao and D. G. Thombare, "Review on exhaust gas heat recovery for i.c. engine," in *Certified International Journal of Engineering and Innovative Technology*, 2013, vol. 2, no. 12, pp. 2277–3754.
- [13] M. Dornheim, "Thermodynamics of metal hydrides: Tailoring reaction enthalpies of

- hydrogen storage materials,” in *Thermodynamics - Interaction Studies - Solids, Liquids and Gases*, Dr. Juan Carlos Moreno Pirajan, Ed. Intech open science - open minds, 2011.
- [14] W. M. Mueller, J. P. Blackledge, and G. G. Libowitz, *Metal Hydrides*. New York: Academic Press, 1968.
- [15] G. Friedlmeier, “Charakterisierung von Hochtemperatur-Metallhydriden auf Magnesium-Basis,” Dissertation, University of Stuttgart, 1997.
- [16] A. Züttel, “Hydrogen storage methods,” *Naturwissenschaften*, vol. 91, no. 4, pp. 157–72, 2004.
- [17] J. H. N. van Vucht, F. A. Kuijpers, and H. C. A. M. Bruning, “Reversible room-temperature absorption of large quantities of hydrogen by intermetallic compounds,” *Philips Res. Repts*, vol. 25, pp. 133–140, 1970.
- [18] J. Hout, *Handbook of hydrogen storage*. Weinheim: Wiley-VCH, 2010.
- [19] K. Young, *Metal Hydrides*. Elsevier Inc., 2013.
- [20] D. L. Cao, H. H. Cheng, L. Ma, D. M. Chen, M. Q. Lue, and K. Yang, “Effects of Al partial substitution for Ni on properties of LaNi_{5-x}Al_x,” *Trans. Nonferrous Met. Soc. China*, vol. 17, no. 50276063, pp. S967–S971, 2007.
- [21] X. H. An, Y. B. Pan, Q. Luo, X. Zhang, J. Y. Zhang, and Q. Li, “Application of a new kinetic model for the hydriding kinetic of LaNi_{5-x}Al_x (0 ≤ x ≤ 1.0) alloys,” *J. Alloys Compd.*, vol. 506, no. 1, pp. 63–69, 2010.
- [22] A. J. Goudy, D. G. Stokes, and J. A. Gazzillo, “The effect of heat transfer on the desorption kinetics of LaNi₅H₆,” *J. Less Common Met.*, vol. 91, no. 1, pp. 149–158, 1983.
- [23] T. B. Flanagan, H. Noh, and S. Luo, “The thermodynamic characterization of ZrCo-H, HfCo-H, HfNi-H and Zr_{1-x}Hf_xNi(Co) Alloy-H Systems,” *J. Alloys Compd.*, vol. 677, pp. 163–170, 2016.
- [24] M. Ron, “The normalized pressure dependence method for the evaluation of kinetic rates of metal hydride formation/decomposition,” *J. Alloys Compd.*, vol. 283, no. 1–2, pp. 178–191, 1999.
- [25] A. Rodríguez Sánchez, H.-P. Klein, and M. Groll, “Expanded graphite as heat transfer matrix in metal hydride beds,” *Int. J. Hydrogen Energy*, vol. 28, no. 5, pp. 515–527, 2003.
- [26] M. V. C. Sastri, B. Viswanathan, and S. S. Murthy, *Metal Hydrides - Fundamentals and Applications*. Berlin, Heidelberg: Springer, 1998.
- [27] E. Rabkin and V. M. Skripnyuk, “On pressure hysteresis during hydrogenation of metallic powders,” *Scr. Mater.*, vol. 49, no. 5, pp. 477–483, 2003.
- [28] L. K. Doraiswamy and M. M. Sharma, *Heterogeneous reactions: analysis, examples,*

- and reactor design. Volume 1: Gas-solid and solid-solid reactions. New York: Wiley, 1984.
- [29] P. Dantzer, "Metal-Hydride technology: A critical review," in *Hydrogen in Metals III. Properties and Applications*, H. Wipf, Ed. Berlin, Heidelberg: Springer, 1997.
- [30] L. Schlapbach, Ed., *Hydrogen in Intermetallic Compounds II*. Berlin, Heidelberg: Springer, 1992.
- [31] M. Martin, C. Gommel, C. Borkhart, and E. Fromm, "Absorption and desorption kinetics of hydrogen storage alloys," *J. Alloys Compd.*, vol. 238, no. 1–2, pp. 193–201, 1996.
- [32] P. S. Rudman, "Hydriding and dehydriding kinetics," *J. Less-Common Met.*, vol. 89, no. 1, pp. 93–110, 1983.
- [33] K. S. Nahm, W. Y. Kim, S. P. Hong, and W. Y. Lee, "The reaction kinetics of hydrogen storage in LaNi₅," *Int. J. Hydrogen Energy*, vol. 17, no. 5, pp. 333–338, 1992.
- [34] J. W. Oh, C. Y. Kim, K. S. Nahm, and K. S. Sim, "The hydriding kinetics of LaNi_{4.5}Al_{0.5} with hydrogen," *J. Alloys Compd.*, vol. 278, pp. 270–276, 1998.
- [35] C. S. Wang, X. H. Wang, Y. Q. Lei, C. P. Chen, and Q. D. Wang, "The hydriding kinetics of M/Ni₅ - I. Development of the model," *Int. J. Hydrogen Energy*, vol. 21, no. 6, pp. 471–478, 1996.
- [36] R. B. Jordan, *Reaction mechanisms of inorganic and organometallic systems*. Oxford: University Press, 1998.
- [37] J. Zhang, T. S. Fisher, P. V. Ramachandran, J. P. Gore, and I. Mudawar, "A review of heat transfer issues in hydrogen storage technologies," *J. Heat Transfer*, vol. 127, no. 12, p. 1391, 2005.
- [38] S. S. Murthy, "Heat and mass transfer in solid state hydrogen storage: A review," *J. Heat Transfer*, vol. 134, no. 3, p. 31020, 2012.
- [39] A. Mazzucco, M. Dornheim, M. Sloth, T. R. Jensen, J. O. Jensen, and M. Rokni, "Bed geometries, fueling strategies and optimization of heat exchanger designs in metal hydride storage systems for automotive applications: A review," *Int. J. Hydrogen Energy*, vol. 39, no. 30, pp. 17054–17074, 2014.
- [40] I. Bürger, M. Dieterich, C. Pohlmann, L. Röntzsch, and M. Linder, "Standardized hydrogen storage module with high utilization factor based on metal hydride-graphite composites," *J. Power Sources*, vol. 342, pp. 970–979, 2017.
- [41] P. Muthukumar and M. Groll, "Metal hydride based heating and cooling systems: A review," *Int. J. Hydrogen Energy*, vol. 35, no. 8, pp. 3817–3831, 2010.
- [42] M. M. H. Bhuiya, A. Kumar, and K. J. Kim, "Metal hydrides in engineering systems, processes, and devices: A review of non-storage applications," *Int. J. Hydrogen Energy*, vol. 40, no. 5, pp. 2231–2247, 2015.

- [43] M. Linder, R. Mertz, and E. Laurien, "Experimental results of a compact thermally driven cooling system based on metal hydrides," *Int. J. Hydrogen Energy*, vol. 35, no. 14, pp. 7623–7632, 2010.
- [44] I.-S. Park, J.-K. Kim, K. J. Kim, J. Zhang, C. Park, and K. Gawlik, "Investigation of coupled AB5 type high-power metal hydride reactors," *Int. J. Hydrogen Energy*, vol. 34, no. 14, pp. 5770–5777, 2009.
- [45] T. Imoto *et al.*, "Development of an F-class refrigeration system using hydrogen-absorbing alloys," *Int. J. Hydrogen Energy*, vol. 21, no. 6, pp. 451–455, 1996.
- [46] N. Aswin, P. Dutta, and S. S. Murthy, "Screening of metal hydride pairs for closed thermal energy storage systems," *Appl. Therm. Eng.*, vol. 109, no. B, pp. 949–957, 2016.
- [47] V. K. Sharma, E. Anil Kumar, and S. Srinivasa Murthy, "Influence of dynamic operating conditions on the performance of metal hydride based solid sorption cooling systems," *Int. J. Hydrogen Energy*, vol. 40, no. 2, pp. 1108–1115, 2015.
- [48] N. Yasuda, T. Tsuchiya, N. Okinaka, and T. Akiyama, "Application of metal hydride sheet to thermally driven cooling system," *Int. J. Hydrogen Energy*, vol. 38, no. 18, pp. 7469–7476, 2013.
- [49] J. Ni and H. Liu, "Experimental research on refrigeration characteristics of a metal hydride heat pump in auto air-conditioning," *Int. J. Hydrogen Energy*, vol. 32, no. 13, pp. 2567–2572, 2007.
- [50] Z. Dehouche, W. de Jong, E. Willers, A. Isselhorst, and M. Groll, "Modelling and simulation of heating/air-conditioning systems using the multi-hydride-thermal-wave concept," *Appl. Therm. Eng.*, vol. 18, no. 6, pp. 457–480, 1998.
- [51] V. K. Sharma and E. Anil Kumar, "Effect of measurement parameters on thermodynamic properties of La-based metal hydrides," *Int. J. Hydrogen Energy*, vol. 39, no. 11, pp. 5888–5898, 2014.
- [52] E. R. Pinatel, M. Palumbo, F. Massimino, P. Rizzi, and M. Baricco, "Hydrogen sorption in the $\text{LaNi}_5\text{-xAl}_x\text{-H}$ system ($0 \leq x \leq 1$)," *Intermetallics*, vol. 62, pp. 7–16, 2015.
- [53] N. Mechi, I. Ben Khemis, H. Dhaou, S. Knani, A. Jemni, and A. Ben Lamine, "A macroscopic investigation to interpret the absorption and desorption of hydrogen in $\text{LaNi}_4.85\text{Al}_0.15$ alloy using the grand canonical ensemble," *Fluid Phase Equilib.*, vol. 427, pp. 56–71, 2016.
- [54] P. K. Selvam, P. Muthukumar, M. Linder, R. Mertz, and R. Kulenovic, "Measurement of thermochemical properties of some metal hydrides – Titanium (Ti), misch metal (Mm) and lanthanum (La) based alloys," *Int. J. Hydrogen Energy*, vol. 38, no. 13, pp. 5288–5301, 2013.
- [55] E. Willers, "Multi-Hydrid-Sorptionsanlage zur kombinierten Heizung und Kühlung," Dissertation, University of Stuttgart, 2002.
- [56] H. Dhaou, F. Askri, M. Ben Salah, A. Jemni, S. Ben Nasrallah, and J. Lamloumi,

- “Measurement and modelling of kinetics of hydrogen sorption by LaNi₅ and two related pseudobinary compounds,” *Int. J. Hydrogen Energy*, vol. 32, no. 5, pp. 576–587, 2007.
- [57] M. Wanner, “Untersuchung des Langzeitverhaltens der thermodynamischen Stabilität von Metallhydriden,” Dissertation, University of Stuttgart, 2001.
- [58] G. Capurso *et al.*, “Development of a modular room-temperature hydride storage system for vehicular applications,” *Appl. Phys. A*, vol. 122, no. 3, p. 236, 2016.
- [59] V. Skripnyuk and M. Ron, “Hydrogen desorption kinetics in intermetallic compounds C2, C5 and C5 with Laves phase structure,” *Int. J. Hydrogen Energy*, vol. 28, no. 3, pp. 303–309, 2003.
- [60] V. M. Skripnyuk and M. Ron, “Evaluation of kinetics by utilizing the normalized pressure dependence method for the alloy Ti_{0.95} Zr_{0.05} Mn_{1.48} V_{0.43} Fe_{0.08} Al_{0.01},” *J. Alloys Compd.*, vol. 295, pp. 385–390, 1999.
- [61] K. Herbrig, L. Röntzsch, C. Pohlmann, T. Weißgärber, and B. Kieback, “Hydrogen storage systems based on hydride–graphite composites: computer simulation and experimental validation,” *Int. J. Hydrogen Energy*, vol. 38, no. 17, pp. 7026–7036, 2013.
- [62] X.-L. Wang and S. Suda, “Study of the hydriding kinetics of LaNi_{4.7}Al_{0.3}-H system by a step-wise method,” *J. Less Common Met.*, vol. 159, pp. 109–119, 1990.
- [63] X.-L. Wang and S. Suda, “Effects of Al-substitution on hydriding reaction rates of LaNi_{5-x}Al_x,” *J. Alloys Compd.*, vol. 191, no. 1, pp. 5–7, 1993.
- [64] F. Feng, M. Geng, and D. O. Northwood, “Mathematical model for the plateau region of P–C-isotherms of hydrogen-absorbing alloys using hydrogen reaction kinetics,” *Comput. Mater. Sci.*, vol. 23, no. 1–4, pp. 291–299, 2002.
- [65] G. Friedlmeier, M. Schaaf, and M. Groll, “How to measure pressure-concentration-isotherms representative for technical applications,” *Zeitschrift für Phys. Chemie*, vol. 183, pp. 185–195, 1994.
- [66] P. D. Goodell, G. D. Sandrock, and E. L. Huston, “Kinetic and dynamic aspects of rechargeable metal hydrides,” *J. Less Common Met.*, vol. 73, no. 1, pp. 135–142, 1980.
- [67] P. Muthukumar, M. Linder, R. Mertz, and E. Laurien, “Measurement of thermodynamic properties of some hydrogen absorbing alloys,” *Int. J. Hydrogen Energy*, vol. 34, no. 4, pp. 1873–1879, 2009.
- [68] E. Anil Kumar, M. Prakash Maiya, and S. Srinivasa Murthy, “Influence of transient operating conditions on pressure-concentration isotherms and storage characteristics of hydriding alloys,” *Int. J. Hydrogen Energy*, vol. 32, no. 13, pp. 2382–2389, 2007.
- [69] P. Muthukumar, A. Satheesh, M. Linder, R. Mertz, and M. Groll, “Studies on hydriding kinetics of some La-based metal hydride alloys,” *Int. J. Hydrogen Energy*, vol. 34, no. 17, pp. 7253–7262, 2009.

- [70] A. Inomata, H. Aoki, and T. Miura, "Measurement and modelling of hydriding and dehydriding kinetics," *J. Alloys Compd.*, vol. 278, no. 1–2, pp. 103–109, 1998.
- [71] J. Han, "Hydriding kinetics of LaNi₅ and LaNi_{4.7}Al_{0.3}," *Int. J. Hydrogen Energy*, vol. 14, no. 3, p. 181, 1989.
- [72] V. K. Sharma and E. Anil Kumar, "Measurement and analysis of reaction kinetics of La – based hydride pairs suitable for metal hydride – based cooling systems," *Int. J. Hydrogen Energy*, vol. 39, no. 33, pp. 19156–19168, 2014.
- [73] P. D. Goodell and P. S. Rudman, "Hydriding and dehydriding rates of the LaNi₅-H system," *J. Less Common Met.*, vol. 89, no. 1, pp. 117–125, 1983.
- [74] G. Sandrock and R. C. Bowman, "Gas-based hydride applications: Recent progress and future needs," *J. Alloys Compd.*, vol. 356–357, pp. 794–799, 2003.
- [75] M. Dieterich, I. Bürger, and M. Linder, "Open and closed metal hydride system for high thermal power applications: Preheating vehicle components," *Int. J. Hydrogen Energy*, vol. 42, no. 16, pp. 11469–11481, 2017.
- [76] A. Docter, G. Frank, G. Konrad, A. Lamm, and J. T. Mueller, "Fuel cell and method for cold-starting such a fuel cell," US 2008/0102327 A1, 2008.
- [77] P. M. Golben, D. DaCosta, and G. Sandrock, "Hydride-based cold-start heater for automotive catalyst," *J. Alloys Compd.*, vol. 253–254, pp. 686–688, 1997.
- [78] D. H. Dacosta, M. Golben, and D. C. Tragna, "Metal hydride systems for the hydrogen planet," in *Proceedings of the 14th World Hydrogen Energy Conference*, 2002.
- [79] Z. Z. Fang *et al.*, "Metal hydrides based high energy density thermal battery," *J. Alloys Compd.*, vol. 645, no. 1, pp. S184–S189, 2015.
- [80] F. Qin, J. Chen, M. Lu, Z. Chen, Y. Zhou, and K. Yang, "Development of a metal hydride refrigeration system as an exhaust gas-driven automobile air conditioner," *Renew. Energy*, vol. 32, no. 12, pp. 2034–2052, 2007.
- [81] M. Linder and R. Kulenovic, "An energy-efficient air-conditioning system for hydrogen driven cars," *Int. J. Hydrogen Energy*, vol. 36, no. 4, pp. 3215–3221, 2011.
- [82] C. Weckerle, I. Buerger, and M. Linder, "Novel reactor design for metal hydride cooling systems," *Int. J. Hydrogen Energy*, vol. 42, no. 12, pp. 8063–8074, 2017.
- [83] J. Gerstmann and M. Golben, "Metal hydrides preheater for the M2 diesel burner," Report No. NATICK/TR-99/021, Advanced Mechanical Technology Inc., 1999.
- [84] Z. Liu *et al.*, "Novel fuel cell stack with coupled metal hydride containers," *J. Power Sources*, vol. 328, pp. 329–335, 2016.
- [85] M. Ron, "A hydrogen heat pump as a bus air conditioner," *J. Less Common Met.*, vol. 104, no. 2, pp. 259–278, 1984.
- [86] P. M. Golben and E. Lee Huston, "Design and fabricate a metallic hydride heat pump with a cooling capacity of 9000 Btu/h," Report No. AD-A213 756, Ergenics Inc., 1989.

- [87] S.-G. Lee, Y.-K. Kim, and J.-Y. Lee, "Operating characteristic of metal hydride heat pump using Zr-based Laves phase," *Int. J. Hydrogen Energy*, vol. 20, no. 1, pp. 77–85, 1995.
- [88] L. Izhvanov, A. Solovey, V. P. Frolov, and Y. I. Shanin, "Metal hydride heat pump-New type of heat converter," *Int. J. Hydrogen Energy*, vol. 21, no. 11–12, pp. 1033–1038, 1996.
- [89] B.-H. Kang, C. W. Park, and C. S. Lee, "Dynamic behavior and hydrogen transfer in a metal hydride cooling system," *Int. J. Hydrogen Energy*, vol. 21, no. 9, pp. 769–774, 1996.
- [90] M. Ram Gopal and S. S. Murthy, "Experiments on a metal hydride cooling system working with ZrMnFe/MmNi_{4.5}Al_{0.5} pair," *Int. J. Refrig.*, vol. 22, pp. 137–149, 1999.
- [91] E. Willers, M. Wanner, and M. Groll, "Multi-hydride thermal wave device for simultaneous heating and cooling," *J. Alloys Compd.*, vol. 293, pp. 915–918, 1999.
- [92] A. Chernikov, L. Izhvanov, A. Solovey, V. Frolov, and Y. Shanin, "An installation for water cooling based on a metal hydride heat pump," *J. Alloys Compd.*, vol. 330–332, pp. 907–910, 2002.
- [93] H.-P. Klein and M. Groll, "Development of a two-stage metal hydride system as topping cycle in cascading sorption systems for cold generation," *Appl. Therm. Eng.*, vol. 22, no. 6, pp. 631–639, 2002.
- [94] E. Kallweit, J. Hahne, "Effective thermal conductivity of metal hydride powders: measurement and theoretical modelling," in *Heat transfer Vol. 6. Heat transfer augmentation, two-phase flow with and without phase change, conduction and insulation*, G. F. Hewitt, Ed. Rugby, Warwickshire: Inst. of Chem. Eng., 1994, pp. 373–378.
- [95] C. Pohlmann, L. Röntzsch, T. Weißgärber, and B. Kieback, "Heat and gas transport properties in pelletized hydride-graphite-composites for hydrogen storage applications," *Int. J. Hydrogen Energy*, vol. 38, no. 3, pp. 1685–1691, 2013.
- [96] M. Dieterich, C. Pohlmann, I. Bürger, M. Linder, and L. Röntzsch, "Long-term cycle stability of metal hydride-graphite composites," *Int. J. Hydrogen Energy*, vol. 40, no. 46, pp. 16375–16382, 2015.
- [97] T. Oi, K. Maki, and Y. Sakaki, "Heat transfer characteristics of the metal hydride vessel based on the plate-fin type heat exchanger," *J. Power Sources*, vol. 125, no. 1, pp. 52–61, 2004.
- [98] A. Sharafian and M. Bahrami, "Assessment of adsorber bed designs in waste-heat driven adsorption cooling systems for vehicle air conditioning and refrigeration," *Renew. Sustain. Energy Rev.*, vol. 30, pp. 440–451, 2014.
- [99] M. V. Lototsky et al., "Metal hydride systems for hydrogen storage and supply for stationary and automotive low temperature PEM fuel cell power modules," *Int. J. Hydrogen Energy*, vol. 40, no. 35, pp. 11491–11497, 2015.

- [100] M. Afzal, R. Mane, and P. Sharma, "Heat transfer techniques in metal hydride hydrogen storage: A review," *Int. J. Hydrogen Energy*, vol. 42, no. 52, pp. 30661–30682, 2017.
- [101] L. Zhou and Y. Zhou, "Determination of compressibility factor and fugacity coefficient of hydrogen in studies of adsorptive storage," *Int. J. Hydrogen Energy*, vol. 26, no. 6, pp. 597–601, 2001.
- [102] A. Savitzky and M. J. E. Golay, "Smoothing and differentiation of data by simplified least squares procedures," *Anal. Chem.*, vol. 36, no. 8, pp. 1627–1639, 1964.
- [103] A. Züttel, "Metallhydride - Einführung," in *Vorlesungsskript*, Physik Department, Universität Fribourg, Schweiz, 2001.
- [104] C.-N. Park and J.-Y. Lee, "Kinetic properties of the hydrogenation of the FeTi intermetallic compound," *J. Less-Common Met.*, vol. 91, no. 2, pp. 189–201, 1983.
- [105] X. H. Wang, C. S. Wang, C. P. Chen, Y. Q. Lei, and Q. D. Wang, "The hydriding kinetics of MINi5-II. Experimental results," *Int. J. Hydrogen Energy*, vol. 21, no. 6, pp. 479–484, 1996.
- [106] J. Mishler, Y. Wang, P. P. Mukherjee, R. Mukundan, and R. L. Borup, "Subfreezing operation of polymer electrolyte fuel cells: Ice formation and cell performance loss," *Electrochim. Acta*, vol. 65, pp. 127–133, 2012.
- [107] A. Santamaria, H. Y. Tang, J. W. Park, G. G. Park, and Y. J. Sohn, "3D neutron tomography of a polymer electrolyte membrane fuel cell under sub-zero conditions," *Int. J. Hydrogen Energy*, vol. 37, no. 14, pp. 10836–10843, 2012.
- [108] S. J. Lim *et al.*, "Investigation of freeze/thaw durability in polymer electrolyte fuel cells," *Int. J. Hydrogen Energy*, vol. 35, no. 23, pp. 13111–13117, 2010.
- [109] R. Lin, X. Lin, Y. Weng, and Y. Ren, "Evolution of thermal drifting during and after cold start of proton exchange membrane fuel cell by segmented cell technology," *Int. J. Hydrogen Energy*, vol. 40, no. 23, pp. 7370–7381, 2015.
- [110] J. O. Jensen, A. P. Vestbø, Q. Li, and N. J. Bjerrum, "The energy efficiency of onboard hydrogen storage," *J. Alloys Compd.*, vol. 446–447, pp. 723–728, 2007.
- [111] U. Ulmer, M. Dieterich, A. Pohl, R. Dittmeyer, M. Linder, and M. Fichtner, "Study of the Structural, Thermodynamic and Cyclic Effects of Vanadium and Titanium Substitution in Laves-Phase AB₂ Hydrogen Storage Alloys," *Int. J. Hydrogen Energy*, vol. 42, no. 31, pp. 20103–20110, 2017.
- [112] P. Bauer, "Inbetriebnahme und Messungen an einer Anlage für Konzentrations - Druck - Isothermen bei Metallhydriden," Bachelor thesis, Hochschule Heilbronn, 2017.
- [113] Deutscher Wetterdienst, "Mean temperature Germany January 1881-2018," 2018. [Online]. Available: <http://www.dwd.de/DE/leistungen/zeitreihenundtrends/zeitreihenundtrends.html;jsessionid=174B85265E16ACFE81318337C9E7D701.live11051?nn=560374#buehneTop>. [Accessed: 09-Sep-2017].

Parts of this study have been presented in the following publications:

Scientific Journals:

M. Dieterich, I. Bürger, and M. Linder, "Open and closed metal hydride system for high thermal power applications: Preheating vehicle components," *Int. J. Hydrogen Energy*, vol. 42, no. 16, pp. 11469–11481, 2017.

I. Bürger, M. Dieterich, C. Pohlmann, L. Röntzsch, and M. Linder, "Standardized hydrogen storage module with high utilization factor based on metal hydride-graphite composites," *J. Power Sources*, vol. 342, pp. 970–979, 2017.

U. Ulmer, M. Dieterich, A. Pohl, R. Dittmeyer, M. Linder, and M. Fichtner, "Study of the structural, thermodynamic and cyclic effects of vanadium and titanium substitution in laves-Phase AB₂ Hydrogen Storage Alloys," *Int. J. Hydrogen Energy*, vol. 42, no. 31, pp. 20103–20110, 2017.

M. Dieterich, C. Pohlmann, I. Bürger, M. Linder, and L. Röntzsch, "Long-term cycle stability of metal hydride-graphite composites," *Int. J. Hydrogen Energy*, vol. 40, no. 46, pp. 16375–16382, 2015.

International Conferences:

M. Dieterich, I. Bürger, and M. Linder, "Next Generation Car – Coupled Thermochemical Reactions for Preheating Vehicle Components," Presentation, in *EVS30 - Electric Vehicle Symposium & Exhibition*, Stuttgart, Germany: 2017.

M. Dieterich, I. Bürger, and M. Linder, "Preheating fuel cells at -20°C with metal hydrides using the pressure difference between tank and stack," Presentation, in *WHTC - 7th World Hydrogen Technology Convention*, Prague, Czech Republic: 2017.

M. Dieterich, I. Bürger, F. Heubner, L. Röntzsch, and M. Linder, "Passive cooled metal hydride hydrogen storage module for stationary applications," Presentation, in *WHEC 2016 - 21st World Hydrogen Energy Conference 2016*, Zaragoza, Spain: 2016.

M. Dieterich, I. Bürger, and M. Linder, "High density hydrogen storage in metal hydride composites with air cooling," Presentation, in *ANM - 7th International conference on Advanced Nano Materials*, Aveiro, Portugal: 2015.

M. Dieterich, I. Bürger, M. Linder, and A. Wörner, "Investigation of long term cycle stability – first results of metal hydride composites," in *MH - 14th International Symposium on Metal-Hydrogen Systems*, Manchester, Great Britain: 2014.

M. Dieterich, M. Linder, and A. Wörner, "Thermal management in vehicles with thermochemical energy storage," in *ICSAT - 5th International Conference on Sustainable Automotive Technologies*, Ingolstadt, Germany: 2013.

During the work on this study, the following theses related to the present work have been supervised:

L. Uechitthaworn, "Construction and Measurement of Thermochemical Pre-Heater based on Metal Hydrides for Fuel Cells in Vehicles," Master thesis, Offenburg University of Applied Sciences, 2018.

J. Hoffmeyer, "Auslegung eines Laborreaktors zur Untersuchung des Stofftransports in Metallhydriden und zur Vorwärmung einer Niedertemperatur-PEM-Brennstoffzelle," Master thesis, University of Stuttgart, 2016.

M. C. Pang, "Design and construction of thermochemical heat storage test bench for automotive thermal management," Bachelor thesis, University of Applied Sciences Heilbronn, 2013.

Appendix

Appendix A - Details on Hydralloy C5 investigated in this work

Appendix B - Details on characterization test bench

- B1. Determination of tubes, Sieverts' and reactor volumes
- B2. Calculation of hydrogen conversion
- B3. Normalization of desorbed hydrogen conversion during PCI measurements
- B4. Temperature change during the PCI measurements
- B5. Considerations on the calculation of hydrogen conversion at low temperatures of C5 measurements
- B6. All results for the PCI-plateau slope

Appendix C - Details on laboratory scale test bench

- C1. Calibration of thermocouples of laboratory test bench
- C2. Calculation of measurement uncertainties

Appendix A - Details on Hydralloy C5 investigated in this work

The material investigated in this work for hydrogen supply was provided by GfE Metalle und Materialien GmbH (Germany). The composition of a 5 kg sample was provided as given in Table 14. From this, the molar composition was calculated, and led to a composition for C5 in this work given as: $\text{Ti}_{0.95}\text{Zr}_{0.05}\text{Mn}_{1.46}\text{V}_{0.45}\text{Fe}_{0.09}$.

Table 14. Composition information of Hydralloy C5 from supplier

	share in wt.-%
Ti	27.1
Zr	2.9
Mn	51.2
V	15
Fe	3.1

Appendix B - Details on characterization test bench

B1. Determination of tubes, Sieverts' and reactor volumes

The different volumes of the test bench can be measured, if one volume is already known. Therefore, the volume of V_{S1} was determined with water in three runs and the average value was used. A definite initial pressure is set in this volume whereas the connected one is evacuated. After opening the connecting valve (valve 4), the resulting pressure allows the calculation of the unknown volume. This procedure can be repeated for every volume of the test bench and of the reactor. The results are given in Table 15.

Table 15. Tubes, Sieverts' and reactors free volumes, partly from [112]

V_{tl}	V_{tr1}	V_{tr2}	V_{tr3}	V_{tr4}	V_{ref}	V_{S1}	V_{S2}
ml							
26.24	7.69	8.71	4.72	6.05	1.0	291.4 ^e	492.49
$V_{free,reactor}$							
ml							
PCI				reaction rates			
LaNi _{4.85} Al _{0.15}		C5		Charge I		Charge II	
23.8		32.41		34.5		31.9	

tl: tube left; tr: tube right; ref: reference for pressure difference measurement with p_d ; S: Sieverts'

^e Determined with water

B2. Calculation of hydrogen conversion

Hydrogen conversion for absorption

The mass of hydrogen absorbed up to time t ($m_{abs}(t)$) is calculated from the total mass which has left the Sieverts' volume and the mass which led to the pressure increase in the reactor ($m_{free,R-side}(t)$) as given in equation (21). The hydrogen mass flown out of the Sieverts' volume is calculated according to the ideal gas law as given in equation (22), where V_{Siev} is the used Sieverts' volume ($V_{Siev} = V_S + V_{tl} + V_{tr2}$; V_S varied for different experiments, see section 2.3.4), $T_s(t)$ is its temperature at time t , M is the molar mass of hydrogen ($M = 2 \text{ g/mol}_{H_2}$), R is the universal gas constant ($R = 8.314 \frac{\text{J}}{\text{mol K}}$) and $p_{d,corr}(t)$ is the corrected pressure drop in the Sieverts' volume. The correction is necessary, because the automated program opens valve 6 before opening valve 9 to the reactor. This enlargement of the Sieverts' side before the actual start of the reaction is taken into account by using the minimal value at the very beginning of the reaction for standardization (see equation (23)). The hydrogen mass leading to the pressure increase on the reactor side is

calculated as given in equation (24). The reactor side consists of the free volume of the reactor ($V_{free,R}$) and the tube volume on the reactor side ($V_{tube} = V_{tr3} + V_{tr4} + V_{tr1}$). The pressure increase is calculated from the pressure difference between the current $p_R(t)$ and initial pressure of the reactor $p_R(t_0)$.

$$m_{abs}(t) = m_{Siev}(t) - m_{free,R-side}(t) \quad (21)$$

$$m_{Siev}(t) = \frac{V_{Siev} M}{T_S(t) R} p_{d,corr}(t) \quad (22)$$

$$p_{d,corr}(t) = p_d(t) - p_d(t_{min. \text{ at beginning}}) \quad (23)$$

$$m_{free,R-side}(t) = \frac{V_{free,R} + V_{tube}}{T_{tube}(t)} \frac{M}{R} (p_R(t) - p_R(t_0)) \quad (24)$$

Combining all equations, the absorbed mass of hydrogen can be calculated according to equation (25).

$$m_{abs}(t) = \left(\frac{(V_S + V_{tl} + V_{tr2})}{T_S(t)} (p_d(t) - p_d(t_{minimum \text{ at the beginning}})) - \frac{V_{free,R} + V_{tube}}{T_{tube}(t)} p_R(t) \right) \frac{M}{R} \quad (25)$$

Hydrogen conversion for desorption

The hydrogen mass $m_{des}(t)$ desorbed until time t is calculated from the volume flow controller according to equation (26).

$$m_{des}(t) = m_{Siev,end} \quad \text{flowed into reactor side during absorption}$$

$$- m_{V_{tr4}}(p/T_{R,abs,end}) \quad \text{not on reactor side at desorption anymore}$$

$$- m_{V_{tr1}}(p/T_{R,abs,end})$$

$$+ m_{V_{tr2}}(p/T_{S,abs,end}) \quad \text{additionally on reactor side at desorption} \quad (26)$$

$$- \sum_{i=0}^t \left(\frac{p_N \dot{V}_{VFC}(i) M}{R T_N} \Delta t \right) \quad \text{flows out of reactor side during desorption}$$

$$- m_{free,R-side}(p_R(t)) \quad \text{leading to pressure drop in reactor, not desorbed from material}$$

The hydrogen flow into the reactor during absorption $m_{Siev,end}$ is taken from equation (22) at the end of absorption. The volume flow controller can only measure in one direction. Therefore, the flow direction of the hydrogen has to be adjusted for desorption, which leads to a change of the volume of the reactor side. Hence, instead of the volumes V_{tr4} and V_{tr1} , now, V_{tr2} is on the reactor side. This is taken into account by subtracting the contained hydrogen masses $m_{V_{tr4}}$ and $m_{V_{tr1}}$ and adding $m_{V_{tr2}}$, which are calculated with the ideal gas law using values for pressure and temperature according to the conditions at the end of absorption. The hydrogen mass flown out of the reactor is calculated using the volume flow for every time step ($\dot{V}_{VFC}(t) \cdot \Delta t$). The volume is converted to mass with the ideal gas law using normal conditions ($p_N = 1.013 \text{ bar}$ and $T_N = 273.15 \text{ K}$). The mass until time t results from the sum of these values. The hydrogen mass flown out of the reactor which leads to a pressure decrease but was not desorbed from the material $m_{free,R-side}(p_R(t))$ is calculated using the ideal gas law as given in equation (27).

$$m_{free,R-side}(p_R(t)) = \left(\frac{V_{free,R}}{T_R(t)} + \frac{V_{tr3} + V_{tr2}}{T_{tube}(t)} \right) \frac{M}{R} p_R(t) \quad (27)$$

The hydrogen inside the reactor is at reactor temperature and the hydrogen in the tubes at tube temperature, respectively.

The calculated hydrogen conversion for desorption led to lower values than for absorption. This is a commonly seen result in PCI measurements. However, the material has to desorb the same amount as was absorbed, because during the next absorption process, the same hydrogen conversion value is reached (without additional desorption). Additionally, the balance via Sieverts' method during absorption leads to more accurate values than via the flow rate meter during desorption. Therefore, the hydrogen conversion during desorption is normalized by fitting the absolute hydrogen conversion to the value given for the absorption.

B3. Normalization of desorbed hydrogen conversion during PCI measurements

The calculated desorbed hydrogen conversion value during PCI measurements is normalized by fitting the absolute hydrogen conversion to the value given for the absorption. The VFC values $m_{des}(t)$ are used for accurate relative changes during the reaction time. The hydrogen pressure in V_{tr2} at the beginning of desorption corresponds to the pressure of the

Sieverts' volume at the end of absorption, which in many cases is above reactor pressure. When changing the reactor side volume to adjust the flow direction, the connection of V_{tr2} with the reactor might lead to pressure increase and further absorption. However, since the pressure increase is minimal due to the small volume of 8.71 ml and the material absorbs in the β -phase here, this effect is neglected.

These considerations lead to the following fitting conditions given by equation (28) and (29).

$$m_{des,init} = m_{abs,end} \quad (28)$$

$$m_{des,end} = 0 \quad (29)$$

Using a linear correlation, the normalized hydrogen mass $m_{norm}(t)$ is calculated according to equation (30), where the indices *end* and *init* refer to the value at the end and beginning of the reaction, respectively.

$$m_{norm}(t) = m_{abs,end} \frac{m_{des}(t) - m_{des,end}}{m_{des,init} - m_{des,end}} \quad (30)$$

The hydrogen conversion ω is calculated from the hydrogen mass for both absorption and desorption using the mass of metal hydride, as given in equation (2).

B4. Temperature change during the PCI measurements

Temperature change of $LaNi_{4.85}Al_{0.15}$ during the PCI measurements

Figure 49 gives the temperature change for all experiments for the total duration of the experiments and in more detail for the first 30 min.

The largest changes in temperature occur at the beginning of absorption at high temperatures. However, within this period, the hydrogen conversion does not exceed a value of 0.024 wt.-% (for # 9-11) and hence corresponds to the formation of the α -phase. Therefore, this temperature change, which is appreciably small anyway, does not interfere with the plateau measurements and the experiments can be considered as isothermal.

This figure confirms that the temperature never changes by more than 3 K, as required, and significantly less during the $\alpha+\beta$ -phase. Hence, the acquired data can be related to the set temperature.

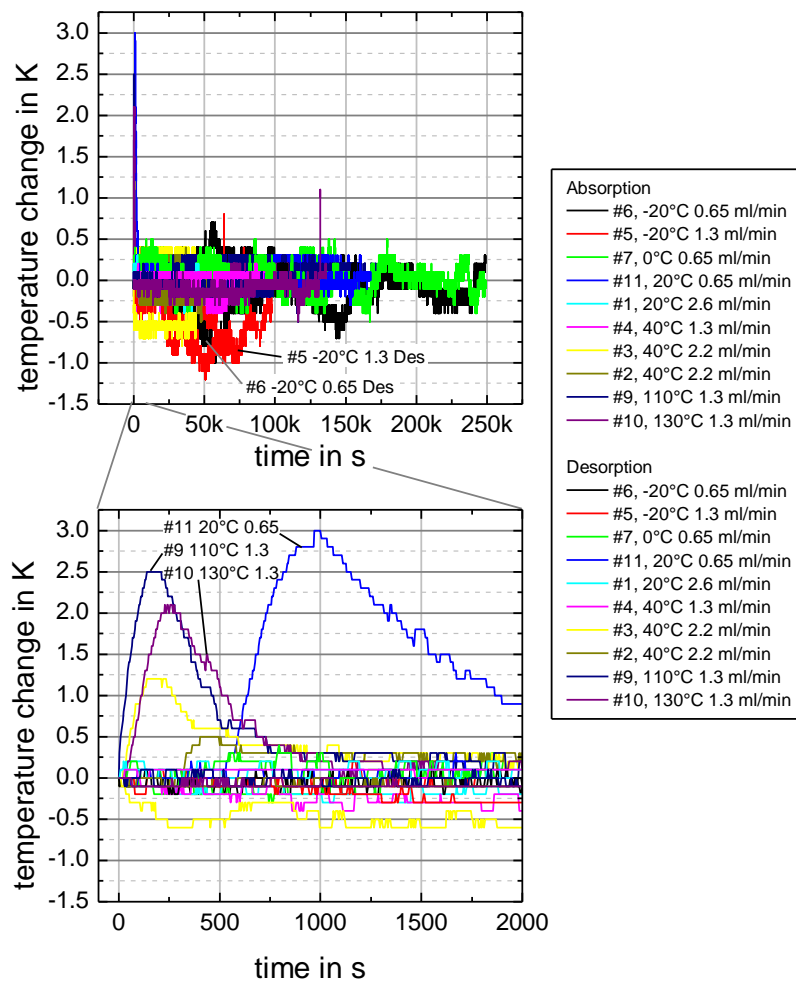


Figure 49. Temperature change during all PCI measurements (abs + des) for $\text{LaNi}_{4.85}\text{Al}_{0.15}$ for the total duration of experiment (top) and close up at the beginning (bottom)

Temperature change of C5 during the PCI measurements

The temperature change of the material for all experiments is given in Figure 50. The beginning is enlarged for a detailed display of the largest changes. The temperature never exceeded a change of more than 1.7 K. Hence, the material stayed close to equilibrium and the results can be referred to the intended temperature.

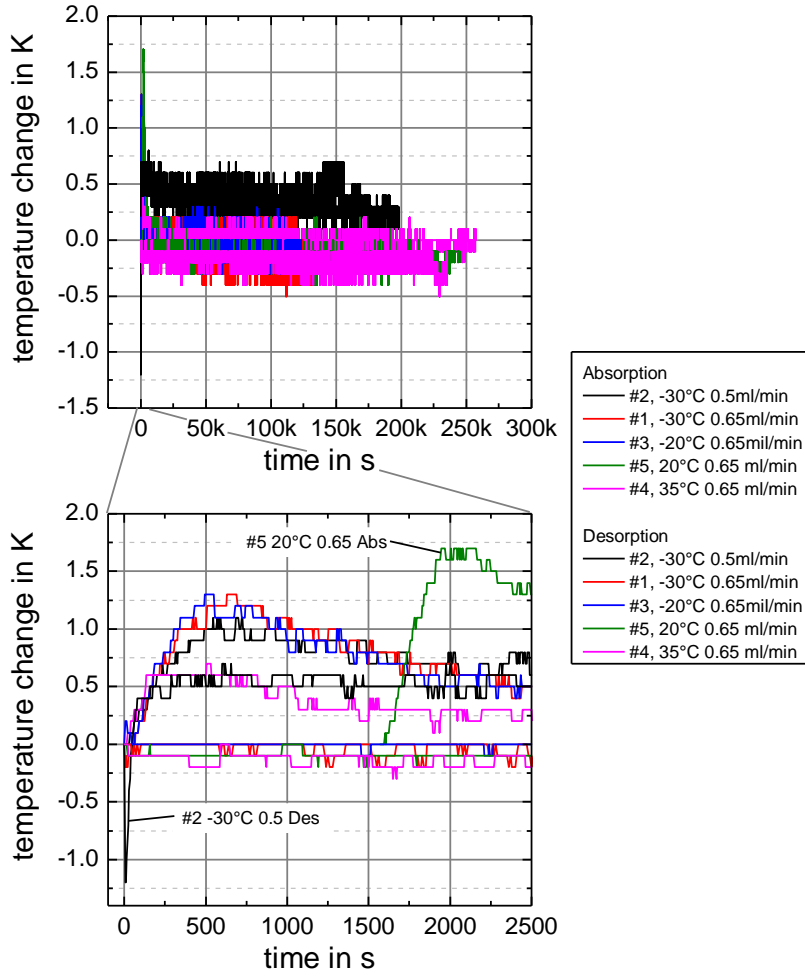


Figure 50. Temperature change during all PCI measurements (abs + des) for C5 for the total duration of experiment (top) and close up at the beginning (bottom)

B5. Considerations on the calculation of hydrogen conversion at low temperatures of C5 measurements

Although the experiments and analysis have been performed with great care, the overall hydrogen conversion shows slightly smaller values for decreased temperatures. This contradicts with the phase model according to Figure 2 in chapter 1.2. However, all possible effects of the analysis were looked at intensively, which is given in this section.

Analysis – relevant equation

$$\omega_{abs}(t) = \left(\frac{(V_S + V_{tl} + V_{tr2})}{T_s(t)} (p_a(t) - p_a(t_{minimum\ at\ the\ beginning})) - \frac{V_{free,R} + V_{tube}}{T_{tube}(t)} p_R(t) \right) \frac{M}{R \cdot m_{MH}}$$

Experimental procedure

The material was not changed in between experiments, nor was the reactor de- and installed during measurements. Also, nothing was changed on the test bench side during the measurement phase.

Assumptions

The small temperature change of the material of maximal 1.4 K is unlikely to cause the result and is accounted for in the calculation anyway. The hydrogen temperature is assumed to stay at Sieverts' temperature also after flowing into the reactor. This value was greatly varied and no influence on the hydrogen conversion could be observed.

Measurement precision

The measurement precisions are indicated in Table 3. During the experiments, great care was taken to ensure measurement values much larger than the measurement precisions. The precision of the pressure differential sensor is ± 0.015 bar, whereas hydrogen conversion of 1 wt.-% results in a pressure drop always above 1.8 bar and hence corresponds to more than 100 times of the measurement precision. The end value of the pressure in the reactor was always at least 40 % of the measurement range. The metal hydride mass was determined with a precision of ± 0.001 g. An error of ± 0.06 g was assumed for filling. This is still less than 1 % of the total mass of 6.2 g.

Uncertainties in free volumes

The uncertainties during the determination of the volumes of the test bench and the reactor were determined to less than 2 %. The free volume measurement of the reactor was performed 3 times and the measurement value was always at least 8x of the uncertainty.

In Figure 51, a theoretical variation of the reactor volume was performed. At the top, the calculation considers the actually determined value ($V_{\text{free,R}} = 1$). At the bottom left, a free volume increase of 10 % was used ($V_{\text{free,R}} = 1.1$), and on the right the value was decreased by 10 % ($V_{\text{free,R}} = 0.9$). As can be seen, the increase of the volume decreases the difference of the hydrogen conversion for the different temperatures, however, the value at 20 °C differs more from literature than before. For the decrease of the volume, the difference actually increases. Therefore, the determined volume of the reactor is considered to be correct.

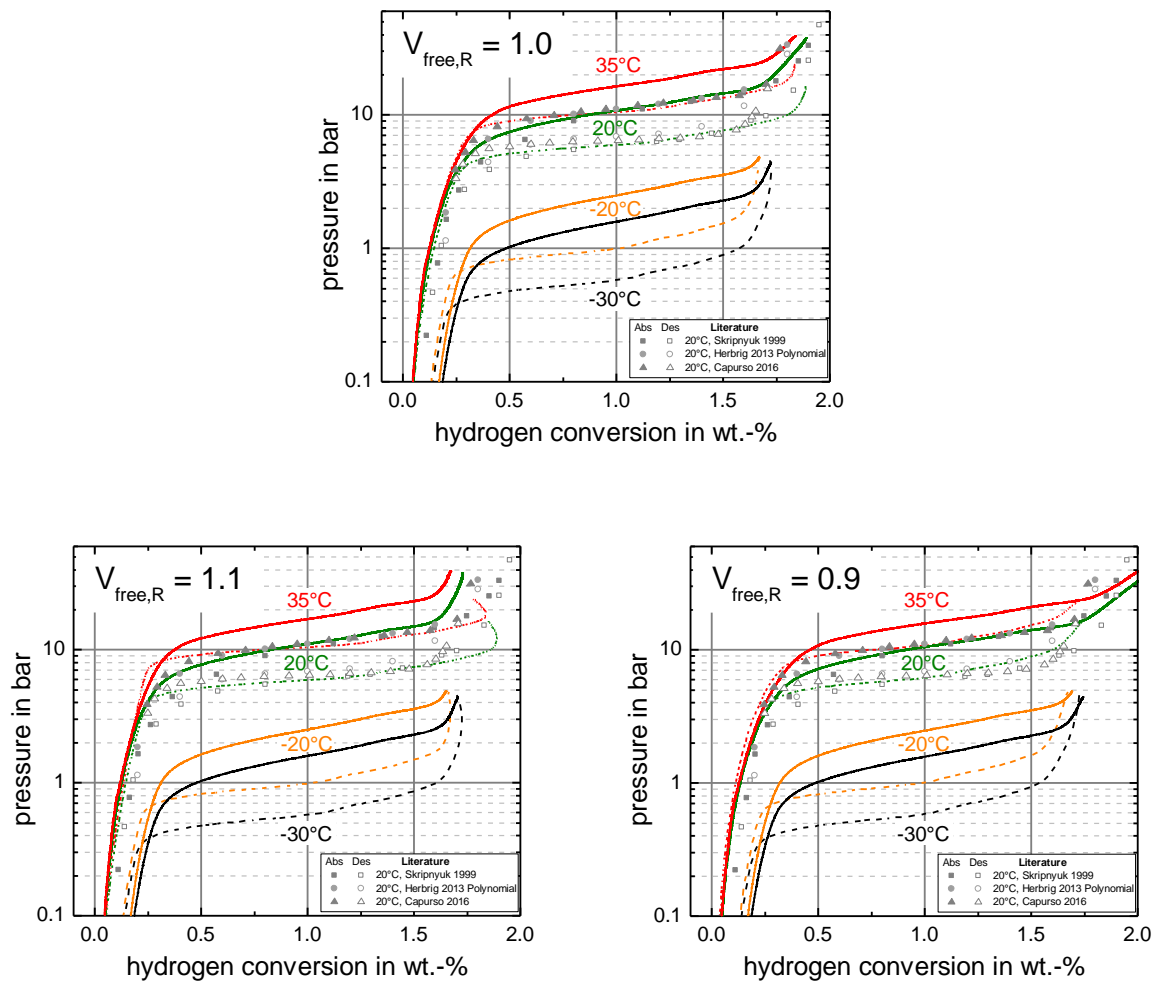


Figure 51. Influence of reactor volume determination

Order of experiments

The influence of the order of experiment, however chosen randomly to exclude any influences, was also considered. However, 23 cycles have been performed before measurement, which leads to the assumption that no further activation should occur inside the material. This corresponds with the hydrogen conversion values during measurement. The order of the investigated temperatures was: -30 °C/ -20 °C/ 35 °C/ 20 °C and the corresponding hydrogen conversion decreased from -30 to -20 °C, increased to 35 °C and decreased again to 20 °C. Therefore, no activation is observed and hence, the order of experiment did not affect the hydrogen conversion.

Compressibility factor

The influence of the compressibility at the low pressures investigated is very small. If considered, however, at the given temperature and pressure range during the measurements, the compressibility factor is always higher for higher pressures. Hence, the calculated mass and therewith hydrogen conversion would also be higher for higher pressures and temperatures [101]. Therefore, the difference between the plateau widths between high and low temperature/ pressure would increase further.

Actual material behavior?

At the end, the question was also considered, if, maybe, the observation represents actual material behavior. However, as can be seen from Table 16 showing the hydrogen conversion for C5 in the laboratory experiments calculated from the hydrogen flow rate, larger hydrogen conversion is observed at lower temperatures, as was expected.

Table 16. Overall hydrogen conversion for the large scale experiments at -20 and 20 °C

T_{amb} in °C	Exp. #	T_{reg} in °C	ΔT_{amb-reg} in K	ω in wt.-%*
-20	10	130	150	1.41
	2			1.42
	16			1.41
	7	90	110	1.40
	14			1.37
+20	1	130	110	1.33
	11			1.32

* Calculated from hydrogen flow meter

Conclusion

Somehow, the pressure drop at low pressures and temperatures is underestimated. Although, all possible effects of the analysis were looked at intensively, as given in this section, the reason for the deviation is unclear. However, the resulting pressure level of the $\alpha+\beta$ -phase is not affected but lead to precise description of the mid-plateau. Hence, the curves were aligned at 50 % conversion and these values were used for further evaluation.

B6. All results for the PCI-plateau slope

For the determination of the slope, the PCI-plateau lines were approximated with a linear regression resulting from equation (4), considering the result of $\ln \frac{p_{eq}}{p_0}$ for the y-axis. The results for both materials are given in Table 17 and Table 18.

Table 17. Plateau slopes for all temperature for $\text{LaNi}_{4.85}\text{Al}_{0.15}$

T in °C	-20	0	20	40	110	130	mean
absorption							
slope	0.0055	0.00474	0.00418	0.00392	0.00336	0.00302	0.00412
standard error	2.30E-06	2.42E-06	4.42E-06	2.68E-06	2.52E-06	2.17E-06	
desorption							
slope	0.00405	0.0039	0.00341	0.00368	0.00342	0.00357	0.00367
standard error	2.90E-06	3.63E-06	4.82E-06	4.67E-06	5.47E-06	7.22E-06	

Table 18. Plateau slopes for all temperature for C5

T in °C	-30	-20	20	35	mean
absorption					
slope	0.80427	0.80095	0.66540	0.62100	0.72291
standard error	6.39E-04	7.25E-04	4.83E-04	2.81E-04	
desorption					
slope	0.60447	0.6069	0.45591	0.47054	0.534455
standard error	0.00146	0.00105	6.95E-04	7.22E-04	

Appendix C - Details on laboratory scale test bench

C1. Calibration of thermocouples of laboratory test bench

All thermometers for the measurement of the HFT at the inlet and outlet of the reactors have been calibrated at the test bench. The correction is presented in the following equations, where all temperatures are inserted in °C.

$$T_{HTF1,out} = 0.99797 \cdot T_{HTF1,in} + 0.02634$$

$$T_{HTF2,out} = 0.99864 \cdot T_{HTF2,in} + 0.03248$$

C2. Calculation of measurement uncertainties

The uncertainties of the test bench were calculated as probable error ε as follows:

$$P_{HTF} = \dot{m}_{HTF} c_{p,HTF} \Delta T_{HTF}$$

$$\varepsilon P = \sqrt{(c_{p,HTF} \Delta T_{HTF} \varepsilon \dot{m}_{HTF})^2 + (\dot{m}_{HTF} \Delta T_{HTF} \varepsilon c_{p,HTF})^2 + (\dot{m}_{HTF} c_{p,HTF} \varepsilon \Delta T_{HTF})^2}$$

$$Q = \int_{t=0}^t P dt \approx \sum (P_i \Delta t)$$

$$\varepsilon Q = \sqrt{\sum (\Delta t \varepsilon P_i)^2}$$

$$\omega = \frac{Q M \cdot 100}{\Delta_R H m_{MH}}$$

$$\varepsilon \omega = \sqrt{\left(\frac{100 M}{\Delta_R H m_{MH}} \varepsilon Q\right)^2 + \left(\frac{-Q 100 M}{\Delta_R H^2 m_{MH}} \varepsilon \Delta_R H\right)^2 + \left(\frac{-Q 100 M}{\Delta_R H m_{MH}^2} \varepsilon m_{MH}\right)^2}$$

The measurement precision of the equipment is given in Table 10. The precision of the heat capacity measurement of the HTF was $\pm 10\%$. No uncertainty was assumed for the time step Δt . For the reaction enthalpy, a precision of $\pm 10\%$ and for the determination of the metal hydride mass, a precision of 0.06 g was assumed.